An Integrated-Optic Current Sensor for Relaying and Metering in High-Voltage Power Systems

by

Jeffrey David Bull

B.A.Sc., The University of British Columbia, 1997

A THESIS SUBMITTED IN PARTIAL FULFILLMENT OF

THE REQUIREMENTS FOR THE DEGREE OF

Doctor of Philosophy

in

THE FACULTY OF GRADUATE STUDIES

(Department of Electrical and Computer Engineering)

The University of British Columbia

July 2004

Abstract

Optical instrumentation has attracted considerable interest over the years for high-voltage applications. Optical fibers, by virtue of their all dielectric construction, are highly resistant to electrical breakdown and electro-magnetic interference, making them ideally suited for signal transmission in substation environments.

A novel hybrid current sensor for high-voltage instrumentation is developed, constructed, and tested here using a Rogowski coil and an integrated-optic Pockels cell (IOPC). The Rogowski coil generates a low-level voltage signal in proportion to the derivative of the primary current. A fully passive integrator is constructed from ultrastable components, permitting integration in the high-voltage environment without the compromised reliability associated with active components and their power supplies. A key aspect of this work is placing the integrator before the optical path to avoid amplification of low-frequency noise and drift. The penalty for using the passive integrator is high attenuation, necessitating a high sensitivity IOPC.

High sensitivity IOPCs with integrated electrodes are fabricated on both X-cut and Y-cut lithium niobate substrates using titanium indiffusion. Only the X-cut configurations are able to provide the needed phase and magnitude stability because they can be fabricated without an optical buffer layer. The buffer layer is shown to be problematic due to mobile charge. IOPCs are pigtailed and packaged in an ultralow stress configuration to provide thermal stability.

High current testing shows the hybrid sensor to exceed IEEE and IEC linearity standards for 0.3 and 0.2 % metering accuracy at a nominal current of 3 kA. The same sensor is also shown to achieve better than 0.5 % instantaneous accuracy when measuring transient over-currents up to 30 kA. The thermal stability of the sensor is shown to be capable of achieving 0.3 % accuracy over a temperature range from -30 to $+70$°C.

Some of the IOPCs tested in this work exhibit a significant degree of mode conversion. The mode conversion is not intentional and results in distortion of the

IOPC transfer function from its ideal sinusoidal shape. The mechanisms responsible for the mode conversion are explained by a coupled-mode formulation of the IOPC that takes into account the anisotropy caused by the electro-optic effect as well as the intrinsic anisotropy of lithium niobate. It is shown that deviations on the order of 0.5° of the propagation direction with respect to the crystallographic axes can induce 100 % mode conversion with waveguide lengths of a few centimeters. The importance of crystallographic alignment is identified and a solution to suppress mode conversion by maintaining a minimum amount of modal birefringence is proposed. Lastly, a new method for measuring birefringence is described based on mode conversion analysis. The method takes advantage of parasitic mode conversion and is non-destructive and unambiguous.

Contents

List of Tables

List of Figures

Acknowledgements

I would like to thank my parents, Ronald and Janeen, for their continuous encouragement to explore the world in which we live with curiosity and creativity. I would also like to thank my sister Traci, and my brother Jeremy for their continuous support of my goals.

Many thanks go to Dr. Nicolas Jaeger for his encouragement to enter graduate studies and to aim for the top. He has given me invaluable technical insights and guidance as my research supervisor.

I would also like to thank Dr. Alina Kulpa and Mr. Hiroshi Kato for their assistance in device fabrication and wealth of knowledge in micro-fabrication.

I am also grateful for the assistance and support provided by Dr. Farnoosh Rahmatian and the technical team at Nxtphase Corporation. Farnoosh's wisdom and professionalism is very much appreciated.

Thanks to Mr. Kjolby, Mr. Dawson, and Mr. Fletcher in the Department of Electrical and Computer Engineering for their superb work in helping construct the mechanical assemblies used in my research.

Lastly, I would like to thank the Natural Sciences and Engineering Research Council of Canada, the British Columbia Advanced Systems Institute, and the University of British Columbia for their financial support.

JEFFREY DAVID BULL

The University of British Columbia
July 2004

To my parents, Janeen and Ronald.

Chapter 1

Introduction and Background

1.1 Introduction

This chapter presents introductory and background material to provide a context for the work presented in this thesis. The chapter begins with an overview of existing current sensor technologies as well as the motivation for developing new current sensors. Optical current sensors are then discussed as well as the hybrid optical approach. The sensor developed in this thesis is a hybrid sensor and the basic elements of this sensor are outlined. The chapter concludes with the organizational structure of the remainder of this thesis.

1.2 Conventional Current Transformers

Current transformers are key instruments in power systems. The two main applications for current measurement are revenue metering and protection [1]. Metering applications are primarily concerned with high accuracy in steady-state conditions

while protection applications are primarily concerned with detecting abnormal operating conditions. The conventional current transformer (CT) provides a relatively high-power output; the North American standard is a 5 A secondary current at rated primary current. The choice of 5 A was made almost a century ago to provide noise immunity and sufficient energy to operate electro-mechanical relays and meters [2]. The introduction of modern, microprocessor based relays and meters that do not require high-powered signals to operate has facilitated the introduction of sensors with low-powered analog or digital outputs [3].

The conventional CT has several disadvantages. For relaying, the saturation of the transformer's non-linear core under fault conditions can distort the waveform. The distortion is particularly prominent when the fault current carries a large "DC" offset on the 60 Hz signal. The flux in the core is proportional to the integral of the induced secondary voltage. As a result, the flux caused by the offset can far exceed the flux from the 60 Hz component [3]. The condition is made worse if residual flux in the core adds to the flux from the fault. Conventional CTs have further disadvantages related to their construction. They are typically oil-filled and have extensive insulation which makes them heavy and costly. For example, a 7718 kg conventional CT is much more expensive to install than a 109 kg optical CT [4].

1.3 Optical Current Sensors

Optical instrumentation has received much attention for high-voltage power system applications. Initial attempts at using optical systems for current measurement in high-voltage applications were made in the late 1960s and early 1970s [2]. Opti-

cal fibers are inherently insulating and as a result provide an ideal signal transport medium for information in high-voltage environments. Optical fibers also provide electro-magnetic interference immunity and virtually unlimited bandwidth for power system applications.

Developments towards an optical current transformer (OCT) have led to several designs. The basic designs can be categorized into five distinct types [2]: 1) conventional CT with optical isolation, 2) magnetic concentrator with optical measurement, 3) bulk optics, 4) optical fiber, and 5) witness sensor. The most direct implementation and perhaps most elegant OCT is the optical fiber type that exploits the Faraday effect. In these sensors, the current interacts directly with the optical properties of the fiber, causing a polarization rotation proportional to the fiber's Verdet constant. Although simple in principle, economic and technical difficulties in producing a commercially viable Faraday effect OCT has led to significant interest in developing accurate, wide-band, and cost effective, hybrid solutions [5].

1.4 The Hybrid Approach

The hybrid optical current sensor takes advantage of the versatility obtained by separating the function of detecting the primary current from the function of transmitting the sensed signal from the high-voltage to the low-voltage environment. This separation allows considerable flexibility and has led to the development of many hybrid current sensors [5, 6, 7, 8]. Two convenient classifications for hybrid current sensors are: 1) active sensors relying on active components in the high-voltage environment, and 2) passive sensors having only passive components in the high-voltage environ-

ment.

The simplest of the active sensors involves only a single active component, namely a light emitting diode (LED). In [7], a conventional current transformer with a 3000:1 ratio was used to drive an LED through a full-wave rectifier. A multimode fiber transmits the signal to a photodetector and spectrum analyzer. The main limitation of this sensor, aside from its rectifying behavior, is thermal instability which was measured to be 0.5 %/°C. The temperature dependence of the LED can be overcome by using a voltage-to-frequency converter to frequency modulate the LED as shown in [9]. Although the FM modulation scheme overcomes the limitations of the amplitude drift of the LED, it involves placing integrated circuits in the high-voltage environment as well as a power supply. Even though power can be tapped from the high-voltage line, battery backup is required to provide instantaneous operation after a re-energization. The difficulty in maintaining a battery as well as the active circuitry is seen as a significant drawback in this type of sensor [10].

Several sensors have been developed based on the all-passive approach. The sensor-heads do not need a power supply and are generally reliable by virtue of having a smaller component count than the active sensors. One implementation of a passive sensor was demonstrated in [6]. This sensor used a conventional CT to drive a piezoelectric cylinder with an optical fiber wrapped around the cylinder. The fiber forms one arm of a fiber-optic Michelson interferometer that intensity modulates an optical carrier. The limitations of this sensor are claimed by the authors to be vibration and temperature sensitivity. Although not explicitly stated in [6], the figures suggest the amplitude error is on the order of 5 %; suitable for protection applications but

inadequate for metering.

A better result for an all-passive sensor was demonstrated in [8]. As in [6], a piezoelectric element is used, but here the piezoelectric element phase modulates a fiber-optic differentiating Sagnac interferometer. This interferometer uses a time delay in the interferometer loop to create an amplitude modulation that is proportional to the derivative of the phase modulation. Since a Rogowksi coil was used to drive the piezoelectric element, the output of this sensor was proportional to the second derivative of the primary current. The authors report a linearity of better than ± 0.3 % from 8 A to 3.2 kA as well as a temperature stability of ± 0.3 % from $-20°$C to $+70°$C. Although this is a sufficient result for revenue metering applications, the frequency response of this sensor is not presented, nor do the authors discuss possible application to relaying. One would expect that recovering a non-sinusoidal primary current signal would require a double integral of the sensor output. It is also expected that a double integrator would suffer from amplification of low-frequency noise. For instance, if such an integrator were used, the noise at 6 Hz would be amplified by a factor of 100 as compared to a 60 Hz signal.

1.5 The Rogowski Coil and Integrated-Optic Pockels Cell CT

The objective of this work was to develop a current sensor that, using a single instrument, could simultaneously satisfy standard requirements for revenue metering as well as for protective relaying. A nominal current of 3 kA was selected for this project,

determined in consultation with Nxtphase Corporation and BC Hydro, Vancouver, BC.

The current sensor developed here is a hybrid sensor having all-passive components in the high-voltage environment. A Rogowski coil [11, 12] is used to sense the primary current and convert it into a voltage signal. Optical isolation is achieved using a modified integrated-optic Pockels cell (IOPC) that was initially developed at the University of British Columbia as a high-voltage sensor [13, 14, 15]. The IOPC is a lithium niobate ($LiNbO_3$) based polarimetric modulator. It was chosen here for adaptation into a hybrid current sensor because of the possibility of optically tracking the sensor-head temperature, normalizing the optical signal path to cancel intensity drift, and the potential for high sensitivity. Because the IOPC is an integrated-optic device, the current sensor developed here has been called the Integrated-Optic Current Transformer, or IOCT.

Two generations of IOCT were made in the course of this work. The first demonstrated excellent linearity performance but was limited in terms of thermal stability and its output was proportional to the time derivative of the primary current [16]. The second generation IOCT incorporated a passive integrator and a much more sensitive IOPC [17]. This sensor is shown here to exceed the performance of other published hybrid current sensors and performs very respectably when compared to stringent IEEE [18] and IEC standards [19, 20].

1.6 Organization of the Thesis

Including this introduction, this thesis is organized into 7 chapters. Chapter 2 presents the theory, design, and construction of the electrical part of the IOCT. The Rogowski coil and integrator designs as well as test results are covered. Chapter 3 covers the work done on the IOPC to adapt it for the hybrid current sensor application. Noise sources affecting the optical system are also analyzed. Chapter 4 covers the fabrication of the IOPC as well as the construction of the IOCT housing. Chapter 5 presents the test results of the IOCT in the context of IEEE and IEC standards. The tests include linearity, frequency response, and temperature stability. Chapter 6 develops a theoretical model to explain unintentional mode conversion that was observed in the course of this work. The mode conversion distorts the IOPC transfer function and can lead to measurement nonlinearity. Finally, Chapter 7 concludes this thesis and makes recommendations for future work.

Chapter 2

Hybrid Sensor Design

2.1 Introduction

This chapter presents the theory, design, and construction of the electrical part of the hybrid current sensor. The chapter begins with an overview of the sensor to identify its functional parts. The theory of the Rogowski coil is then presented. The Rogowski coil is a linear inductive coupler that provides a voltage signal in response to the primary current. Because of the differentiating nature of the Rogowski coil, an integrator must also be used. The optimum integrator design is first presented from a linear system theory point of view. Results using digital integration are presented along with the difficulties encountered when integrating the signal after optical transmission with the IOPC. Finally, the passive integrator that was ultimately selected for the IOCT is described in detail including measurements on component stability and the overall frequency response.

2.2 Sensor Overview

The main components of the Rogowski coil and IOPC current sensor are shown in Figure 2.1. The current is inductively sensed by the Rogowski coil which generates a voltage signal at its terminals in proportion to the derivative of the primary current. A passive integrator recovers a signal proportional to the primary current and applies this voltage to the IOPC. Optical fibers connect the IOPC to an optical source and a polarizing beam splitter. The beam splitter splits the optical output from the IOPC into two complementary optical signals which are detected by an optical receiver. A digital signal processing (DSP) unit processes the complementary signals to cancel optical intensity fluctuations. The DSP unit also performs an arcsine function to compensate for the non-linearity of the IOPC to give a highly linear digital output signal that is proportional to the primary current.

2.3 Rogowski Coil

Rogowski coils represent a different approach to high-precision instrumentation as compared to the conventional CT. The conventional CT relies on its iron core to create a magnetic circuit that is relatively insensitive to geometric variability in its construction. This stability comes at the expense of undesirable properties of the core including saturation and hysteresis [1]. The Rogowski coil uses a non-magnetic core and avoids these non-idealities. Instead, the precision of the Rogowski coil is largely determined by the precision of its geometry [22]. The Rogowski coil must be able to accurately sense the magnetic field of a current carrying conductor in a

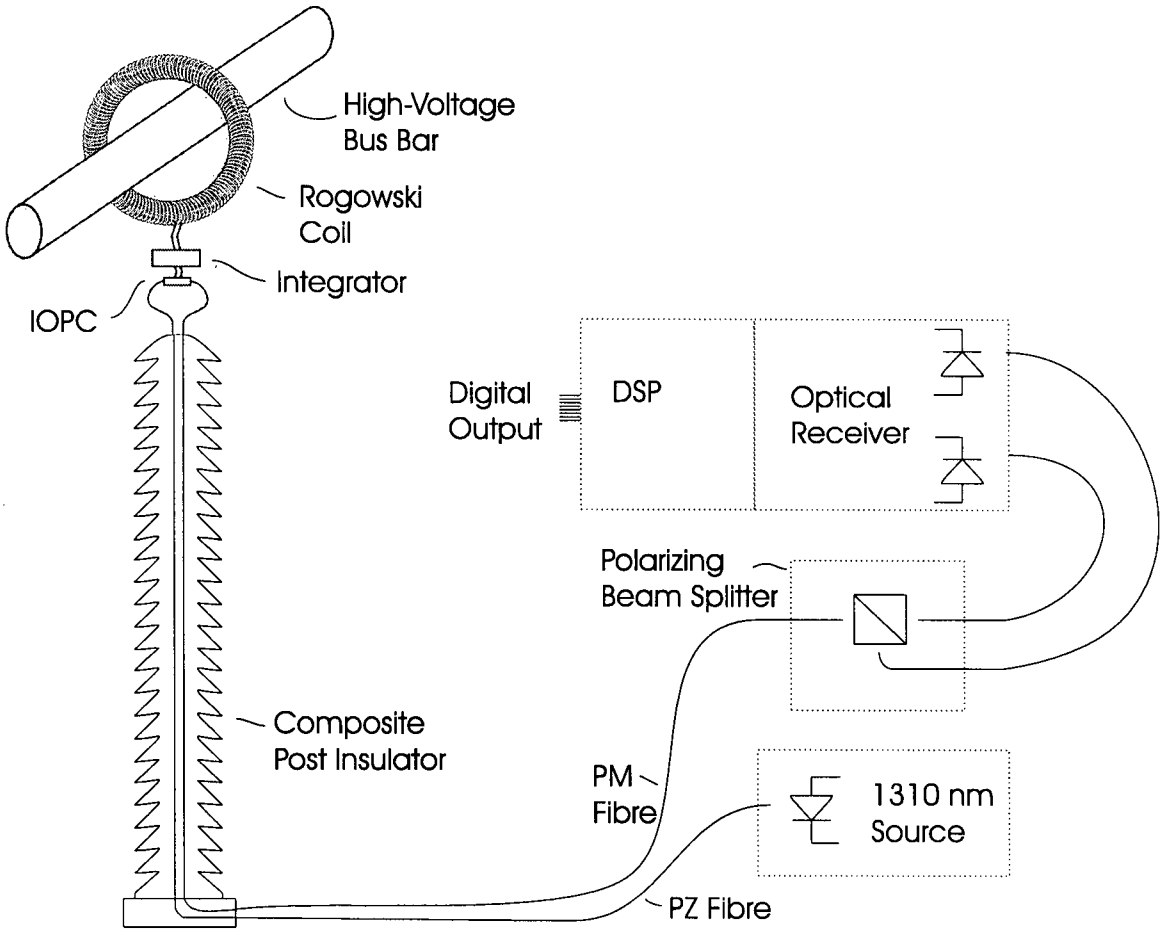

Figure 2.1: Functional diagram of the Integrated-Optic Current Transformer (IOCT) showing the Rogowski coil, IOPC, integrator, optical receiver and the DSP unit [21].

real environment, subject to distortions from other conductors including the other two conductors of a three phase circuit, or other separate circuits. The magnetic field that penetrates a Rogowski coil is also dependent on the position of the primary conductor in relation to the coil. The elegance of the Rogowski coil lies in its ability to keep a constant mutual inductance for any conductor position which it encircles, and its rejection of magnetic fields from nearby conductors. This behavior is achieved by using appropriate coil geometry and precise coil construction.

2.3.1 Theory

It is well known that the mutual inductance of a rectangular cross-sectioned toroid is readily obtained from Faraday's Law as:

$$M = \frac{\mu_o}{2\pi} N w \ln\left(\frac{b}{a}\right) \tag{2.1}$$

where μ_o is the permeability of free space (non-magnetic core), N is the number of coil turns, w is the axial width of the core, a is the inner radius of the core, and b is the outer radius of the core. Equation 2.1 can be extended to cases where the coil is not coaxial with the conductor. In addition, cases where a winding of constant cross-sectional area follows an arbitrary path around the conductor can also exhibit positional independence [23]. The condition for this extension is that the coil approximates the line integral of Ampere's law around the conductor. In the limit as the winding density becomes infinite, and the cross-sectional area of the core vanishes, the Rogowski coil exactly evaluates the line integral. For this reason, the coil should be tightly wound on a core with a relatively small area. The mutual inductance in

this limit is given by:

$$M = \mu_o n A \tag{2.2}$$

where n is the winding density and A is the cross-sectional area of the core.

An equivalent circuit for the Rogowski coil with a load resistor, R_L, is shown in Figure 2.2. This circuit includes the self-inductance of the coil, the coil series resistance, as well as the parasitic capacitance of the windings. Although the Rogowski coil must be operated into a high impedance, the load can be adjusted to advantage. Two performance characteristics that are dependent on the load resistance are the damping factor of the second order circuit and the temperature dependence of the load voltage [24]. For coils where the cross-sectional area is small compared to the coil radius, the temperature variation of the mutual inductance is well approximated by the temperature coefficient of linear expansion of the core material. This relationship results because the coil area increases with the square of the temperature while the turns density decreases linearly with the temperature. For frequencies well below the self-integration frequency, the reactance of the coil is negligible and the gain of the coil is proportional to:

$$G = \frac{R_L(1 + \alpha_{R_L}\Delta T)M(1 + \alpha_{lin}\Delta T)}{R_L(1 + \alpha_{R_L}\Delta T) + R_C(1 + \alpha_{res}\Delta T)} \tag{2.3}$$

where R_L is the load resistance, R_C is the coil resistance, ΔT is the temperature change, α_{R_L} is the temperature coefficient of the load resistor, α_{lin} is the linear expansion coefficient of the core material, and α_{res} is the temperature coefficient of resistivity of the coil. Taking the derivative of G with respect to T and setting it equal to zero, gives the optimum value of R_L:

$$R_L = R_C \frac{(\alpha_{res} - \alpha_{R_L} - \alpha_{lin})}{\alpha_{lin}}. \tag{2.4}$$

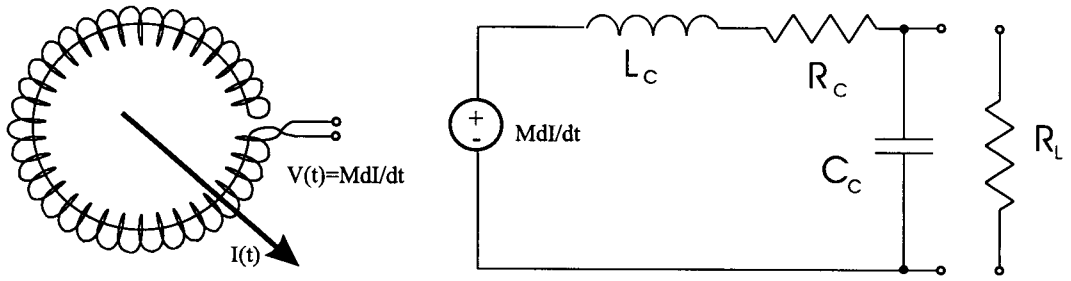

Figure 2.2: Conceptual drawing of a Rogowski coil and its equivalent circuit including a load resistor.

A similar result is given in [24] with the temperature dependence of R_L ignored.

A further performance consideration for the Rogowski coil is the high-frequency response. At high frequencies the capacitance between the coil windings becomes significant. To reduce capacitive noise pickup by the coil, an electrostatic shield should be wrapped around the coil to create an equipotential surface. This screen further increases the parasitic capacitance of the coil. The transfer function relating the primary current to the terminal voltage for the equivalent circuit in Figure 2.2 is:

$$H(s) = \frac{sM}{L_C C_C (s^2 + s\frac{(L_C + C_C R_L R_C)}{C_C R_L L_C} + \frac{R_C + R_L}{C_C R_L L_C})}. \tag{2.5}$$

The poles of Equation 2.5 are complex when the self-integration frequency, associated with L_C, coincides with the low-pass cut-off frequency, associated with C_C. These two poles determine the high-frequency behavior of the Rogowski coil.

2.3.2 Implementation

Three iterations of the Rogowski coil were used in this work. The first iteration was constructed from PVC tubing with a spiraled outer casing (see Figure 2.3). Copper wire (20 gauge) was wrapped into the spiraled casing giving 115 turns around a toroid

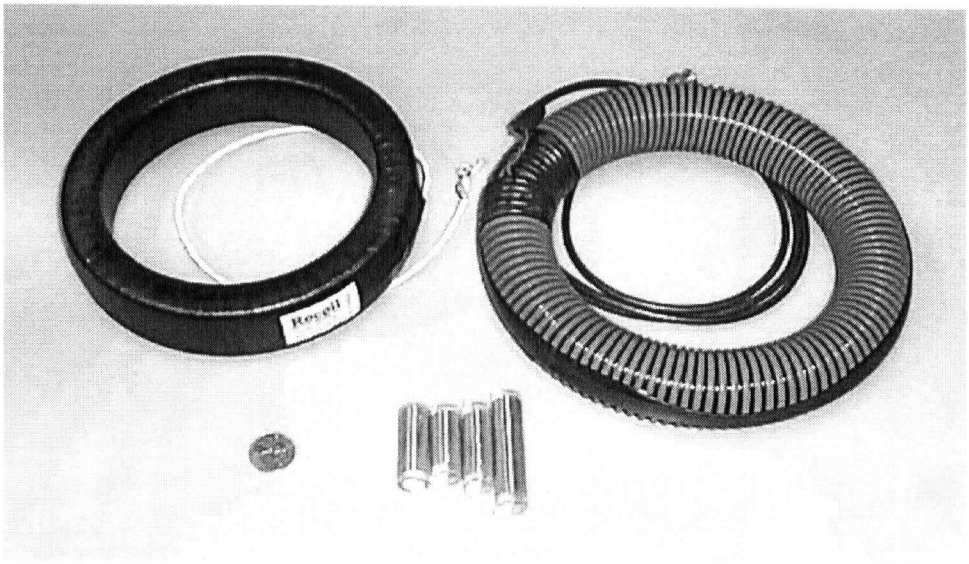

Figure 2.3: The first generation Rogowski coil is shown here on the right. The epoxy-glass core Rogowski coil from Rocoil Limited is shown on the left. At the bottom are coil samples obtained from Rocoil to verify that the conformal coating used to secure the windings would not delaminate at $-40°C$.

with a 224 mm outer diameter and a 161 mm inner diameter. The mutual inductance was 199 nH. The limitations of this type of coil were the dimensional stability of the core and the low mutual inductance. The second and third iterations of the Rogowski coil were custom ordered from Rocoil Limited, Harrogate, North Yorkshire, England. Rocoil's standard core material is acrylic which is used for its machinability and rigidity. The first coil obtained from Rocoil had a mutual inductance of 2.316 μH. It had a width of 38 mm, an outside diameter of 214 mm and an inside diameter of 170 mm, sufficient for a 5 inch busbar. It was used in the first generation IOCT with great success. The only draw back of this coil was the high thermal expansion coefficient of the acrylic, at 90E-6/°C [25], which would give a 0.45 % change in mutual inductance over a 50°C change.

The second generation IOCT was fitted with a Rogowski coil having a custom

designed core made using an epoxy-glass fabric laminate, grade 10G/40 from Tufnol Limited, Perry Barr, Birmingham, England. The thermal expansion coefficient of this material is 11E-6/°C, specified in the plane of the lamination, which is nearly an order of magnitude better than acrylic. The measured parameters for this coil are shown in Table 2.1. The mutual inductance of 5 μH provides a terminal voltage of 16 V_{pp} at a nominal current of 3 kA. This value was selected in consideration of the integrator's attenuation, presented below, and the achievable half-wave voltage for the IOPC, presented in Chapter 3. Any further increase in mutual inductance would compromise the bandwidth of the IOCT as evidenced by the self-resonance frequency of the Rogowski coil at 38 kHz.

The calculated load resistance for temperature compensation using Equation 2.4 is 110 kΩ. The resistance needed for critical damping of the coil self-resonance is much lower at 2.3 kΩ. The value selected for the load resistor was a compromise at 60 kΩ. This value gives a damping ratio of 0.08. The resulting under-damped resonance gives a theoretical rise in the overall sensor amplitude of 7.6 % at 10 kHz. This value is well within acceptable standards and is shown in Section 5.5 to satisfy the frequency response requirements of IEC 60044-8 [20]. To protect the coil from possible over voltages, two 300 V transient voltage suppressors (TVS) were connected in series to give a clamp voltage of 600 V (part number P6KE300CAMSCT, from Microsemi Corp., Irvine, CA.) The measured parasitic capacitance of each TVS is negligible at 32 pF. The 600 V clamp limits the maximum measurable steady-state current to 220 kA, or equivalently, a maximum measurable dI/dt of 120 MA/s.

Table 2.1: Parameters for the epoxy-glass Rogowski coil. Values with a '*' are derived quantities.

Number of Turns	2780
Mutual Inductance	5.04 μH
Self-Inductance *	14.0 mH
Series Resistance	322 Ω
Shunt Capacitance *	1.3 nF
Self-Resonance Frequency	38 kHz

2.4 Integration

Integration is required to recover the current signal since the output of the Rogowski coil is proportional to the derivative of the primary current. An ideal integrator has a reciprocal-frequency magnitude response and a 90 degree phase lag. This relationship implies infinite gain at DC, meaning an ideal integrator will not be tolerant of any finite DC offset errors in the signal path. A further implication of this is that low-frequency noise sources located between the Rogowski coil and the integrator will be amplified with respect to the power frequency. These two issues play a dominant role in the design and the location of the integrator.

The simplest realizable integrator, that has finite gain, is the single non-zero pole integrator. The transfer function is:

$$H(s) = \frac{1}{1 + s/\omega_i} \tag{2.6}$$

where ω_i is the pole frequency. This integrator approaches the response of the ideal integrator at frequencies above the pole frequency. A small pole frequency, smaller than the power frequency, gives a large operating bandwidth but sacrifices signal strength at the power frequency as compared to the pole frequency. In order for this

integrator to achieve a phase error below 8 minutes at 60 Hz, in conformance with IEEE C57.13 [18], the pole frequency must be approximately 60 mHz. The problem with such an integrator is that the power frequency signal is attenuated by a factor of 1000 with respect to frequencies below the pole frequency. In a passive integrator, this means 60 dB of attenuation at the power frequency; for an active integrator, it means amplification of 1/f noise and DC offsets in the circuit. To address these problems, a phase compensator is used. The transfer function for the compensator is:

$$H_c(s) = \left(\frac{s + \zeta\omega_c}{\zeta(s + \omega_c)} \right) \tag{2.7}$$

where ω_c is the compensator pole and ζ determines the phase lag of the compensator. The parameter ζ determines the pole-zero separation, and hence the amount of phase change that can be obtained. The peak phase change is given by [26]:

$$\theta_{\max} = \sin^{-1} \left(\frac{1 - \zeta}{1 + \zeta} \right). \tag{2.8}$$

The penalty for using the compensator is an attenuation at high-frequency of $1/\zeta$ so this parameter should not be too large. We have found that a good compromise is to maximize the gain-phase product of the compensator which occurs at $\zeta \approx 2.54$. The position of the pole-zero pair is then adjusted to null the phase error at the power frequency for the combined integrator-compensator transfer function. This yields a compensator pole frequency given by:

$$f_c = \left(-f_n + f_n\zeta - \sqrt{f_n^2 - 2f_n^2\zeta + f_n^2\zeta^2 - 4f_i^2\zeta} \right) \frac{f_n}{2f_i\zeta} \tag{2.9}$$

where f_n is the nominal power frequency and f_i is the integrator pole frequency.

Figure 2.4 shows the magnitude and phase error plots for the phase compensated integrator for several values of the integrator pole frequency, f_i. The errors are

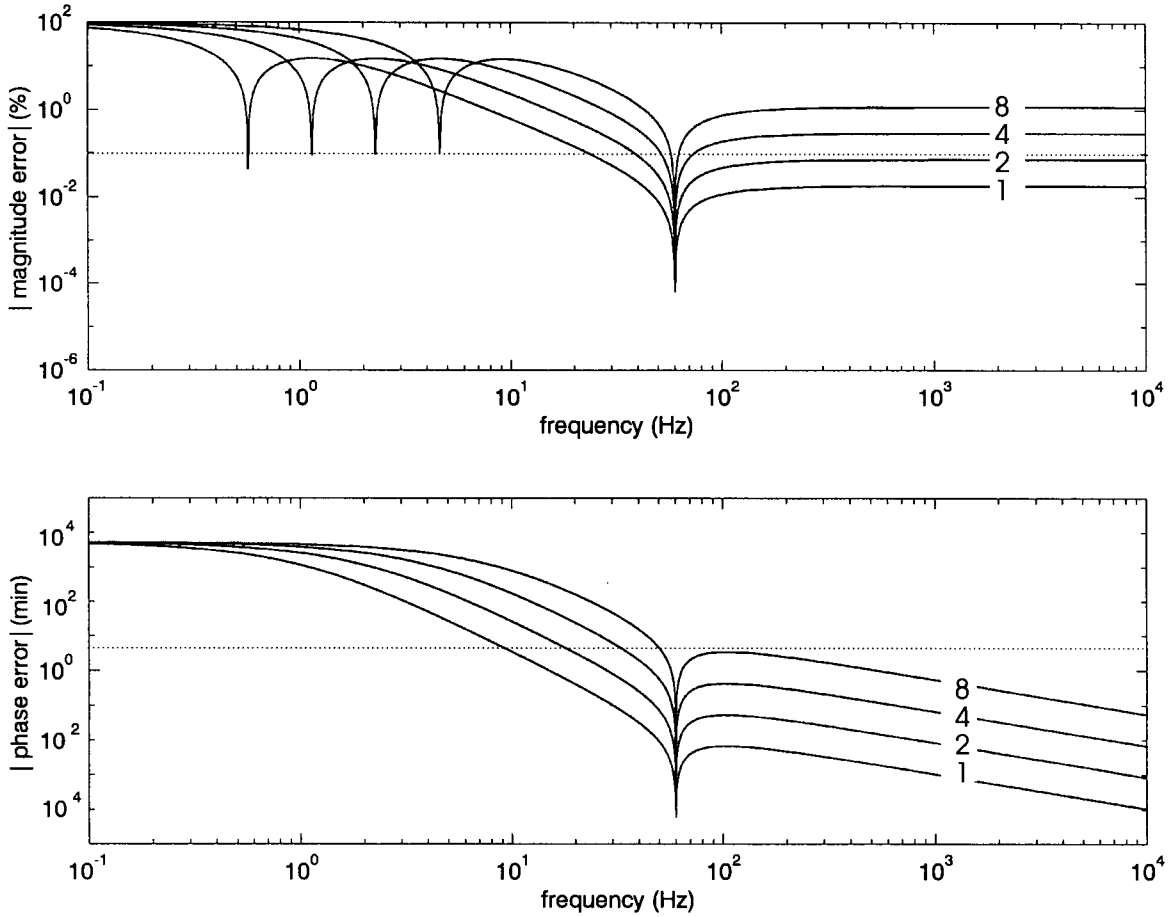

Figure 2.4: Magnitude and phase response for a phase compensated integrator for several values of the integrator pole frequency, f_i: 1, 2, 4 and 8 Hz. Also shown are lines at 0.1 % magnitude and 5 minutes phase.

made to be zero at 60 Hz. From the figure, it is apparent that an integrator pole frequency of 2 Hz or less should be used to keep high-frequency ratio errors below 0.1 %. The phase response for this case maintains an error below 5 minutes of arc to 17 Hz. The corresponding value for f_c is 1.30 Hz.

2.4.1 Digital Integrator

The simplest integrator to implement from a hardware point of view is to add a digital integrating filter to the DSP unit. The feasibility of this method was tested by postprocessing data using Matlab^{TM}, from The MathWorks, Natick, MA. The data set was obtained from transient measurements with a Rogowski coil, an IOPC, and an optical receiver and DSP unit provided by NxtPhase Corporation, Vancouver, BC. More information on the test setup can be found in Chapter 5.

Figure 2.5.a shows a 20 kA test waveform consisting of a 4 second long off-on-off cycle recorded with the current reference described in Chapter 5. Figure 2.5.b shows the digitized signal from the DSP unit that has been linearized to undo the sinusoidal transfer function of the IOPC. This signal is proportional to the derivative of the current. Figure 2.5.c shows the linearized IOPC signal after integration. The phase compensated integrator from the previous section was implemented as an Infinite Impulse Response (IIR) filter with coefficients obtained using the impulse invariant method [27]. Comparing the reference waveform in Figure 2.5.a to the waveform in 2.5.c, it is apparent that the integrated IOPC signal has a substantial transient response after breaking the circuit. The magnitude of this apparent transient is 4 kA at its peak and represents 15 % of the peak current value. Figure 2.5.d shows the result of integrating the waveform in (b) with trapezoidal integration. The ramp seen in the waveform shows that the signal in (b) has a non-zero average but only while the current is energized. Since there are no rectifying elements in the current source, this effect must be due to non-linearity in the sensor. The transient seen at the end of waveform (c) is the negative step response of the integrator, excited by the removal

of the partially rectified signal.

Other problems were encountered with the digital integrator. Slow fluctuations in the IOPC bias point were amplified by the integrator resulting in apparent low-frequency current noise on the order of 100's of amps. It was concluded that the solution to eliminate low-frequency artifacts is to place the integrator before the optical path. The passive integrator discussed next accomplishes this. Passive integrators have been used for measuring current pulses where large dI/dt values mean signal strength is not an issue, and the RC time constant needed for integration is relatively short [28, 29]. For this work, overcoming the drawbacks of low signal strength and long integration times was considered crucial in light of the difficulties encountered with integration after the optical path. The high sensitivity IOPC presented in Chapter 3 was designed specifically to accommodate the attenuation associated with the passive integrator.

2.4.2 Passive Integrator

The ideal location for the integrator from a low-frequency noise perspective is right before the optical signal path. This requires that the integrator be located in the high-voltage environment. Although active components can be used in the high-voltage environment, there are several drawbacks to such an approach. Creating a reliable power supply that will keep the sensor operational while the line is not energized is non-trivial. One approach that has been used to power active electronics is to transmit power over an optical fiber from a remotely located laser [30]. A photodiode functions as a power supply rectifier. The drawback to such an approach is increased complexity,

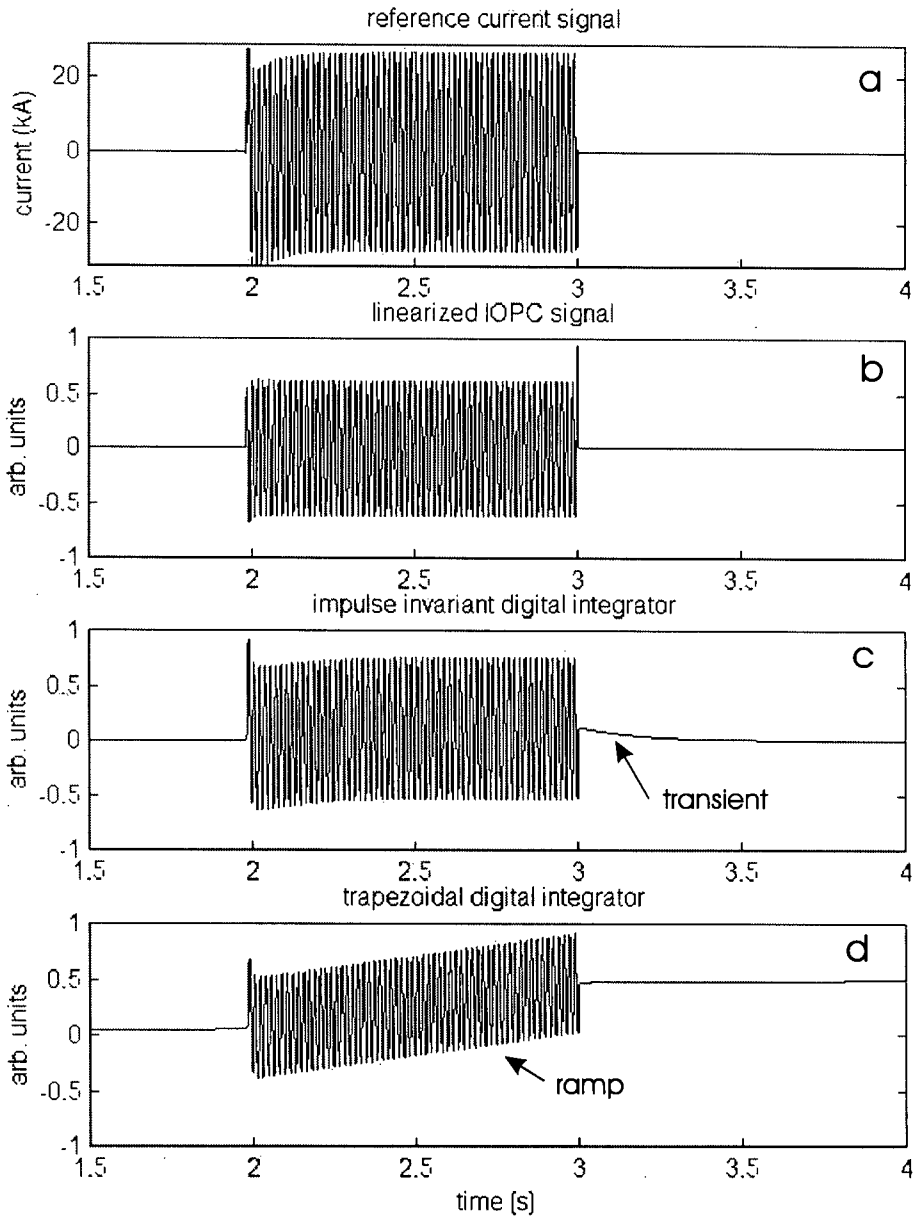

Figure 2.5: Digital integrator evaluation: a) reference current signal, b) linearized IOPC signal, c) IIR integrated version of (b), d) trapezoidal integration of (b).

increased cost, and increased probability of component failure. Batteries can also be used to provide power, but even rechargeable batteries require maintenance. The ideal integrator is passive, requires no power supply, and is constructed from just a few highly reliable components.

The circuit designed to implement the single-pole passive integrator with the phase compensator is shown in Figure 2.6. R_3 and C_1 primarily provide the integrating function, while R_1, R_2, and C_2 primarily provide the phase compensating function. The transfer function for the passive integrator is:

$$H_i(s) = \frac{1 + R_2C_2s}{1 + (R_2C_2 + C_1R_3 + C_2R_1 + C_1R_1)s + (R_3R_2 + R_1R_3 + R_1R_2)C_1C_2s^2} \tag{2.10}$$

where R_L has been ignored because it is almost shorted by the Rogowski coil impedance. The zero and two pole frequencies selected above give three constraints while there are five unknowns in component values. Since the resistors used here were more difficult to obtain than the capacitors, the resistor values where specified first and the required capacitance values were calculated. The selected component values are shown in Table 2.2.

The stability of the integrator components is critical for the sensor to be accu-

Table 2.2: Integrator component values.

Component	Nominal Value	Measured Value
R_1	120 kΩ	120.4 kΩ
R_2	120 kΩ	119.1 kΩ
R_3	1 MΩ	1.004 MΩ
R_L	60 kΩ	n/a
C_1	95 nF	94.67 nF
C_2	400 nF	400.2 nF

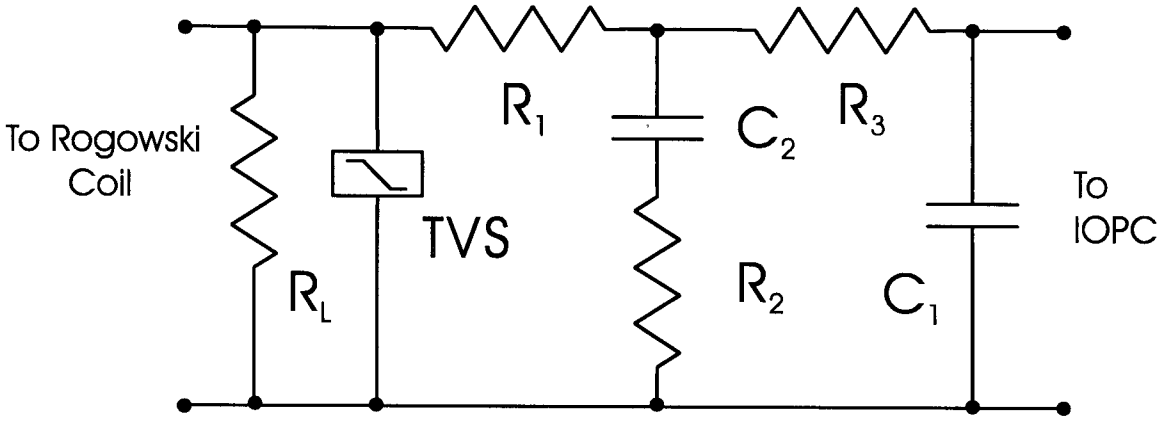

Figure 2.6: Schematic of the passive integrator with phase compensation.

rate. Table 2.3 shows the magnitude and phase sensitivities to each component for the integrator. The magnitude sensitivities are nearly 1 for both R_3 and C_1. This means that a fractional change in these component values will result in an equivalent ratio error. The magnitude sensitivities to R_1 and R_2 are reduced by 50 % and, since both are equal and opposite, systematic variations in their values will substantially cancel each other. The phase sensitivities are significantly less problematic than the magnitude sensitivities because the pole-zero locations are sufficiently far away from the power frequency. For example, a 1 % change in R_2 will produce only a 1.35 minute change in phase. Also of note is that the sum of the resistor sensitivities and the sum of the capacitor sensitivities are both zero for the phase response. This means that systematic variations in the component values will not alter the phase appreciably.

The resistors that were selected for this project were made to order by Precision Resistor Co. (PRC), Inc., Largo, FL. The time stability of these resistors is specified at ± 0.001 %/yr, while their temperature coefficient is 0 ± 5 ppm/°C. They are wire wound resistors, wound to have low inductance and hence low mutual in-

Table 2.3: Sensitivity to integrator component values at 60 Hz.

Component	Magnitude Sensitivity	Phase Sensitivity (minutes)
R_1	−0.53	−45
R_2	0.47	135
R_3	−0.94	−90
C_1	−0.99	−90
C_2	0.00	90

ductance. This is a critical feature since these components must not induce voltage when immersed in a strong magnetic field. Resistor type HR255N (1/4 W, 150 V) was selected for R_1 and R_2 while HR3716N (1 W, 600 V) was selected for R_3 based on the resistance range possible with each resistor type.

The reactance of the resistors from PRC was measured to determine if their wire wound construction would have adverse affects. Measurements were made using an LCR meter, model 4275A from Hewlett Packard (now Agilent), Palo Alto, CA. The HR255N resistors, valued at 120 kΩ, exhibited a shunt capacitance of 1.3 pF at 10 kHz, corresponding to an impedance angle of 0.2 minutes at 60 Hz. The HR3716N resistors, however, valued at 2.2 MΩ, exhibited a shunt capacitance of 2.2 pF at 10 kHz, corresponding to an impedance angle of 6.3 minutes at 60 Hz. This angle was verified at 6.0 minutes at 60 Hz using a Wheatstone bridge [31] configuration but with a 16-bit analog to digital converter, model number DAS1802HR, from Keithley Instruments, Inc., Cleveland, OH, as the detector to measure the phase difference across the bridge. Carbon film resistors were used as the reference resistors which, by virtue of their construction, do not suffer from reactance at 60 Hz. Although the measured 6 minute phase error of the HR3716N resistors is stable, and could be compensated, an alternate high impedance resistor was sought. An available

1 MΩ, wire wound resistor from an unknown manufacturer was found to have the required performance. The temperature coefficient was measured to be very low at approximately −5 ppm/°C. The equivalent shunt capacitance was measured to be 0.11 pF at 10 kHz, equivalent to a 0.1 minute phase error at 60 Hz. This resistor was used as R_3 in light of these performance figures.

The most stable commercial capacitors that could be found have the Electronic Industries Association (EIA) COG designation, specified as 0 ±30 ppm/°C over the range −55 to +125°C. This uncertainty is significantly worse than the resistor stability and represents the most likely source of drift in the integrator. The capacitors used in this work were manufactured by KEMET Electronics Corporation, Greenville, SC, under part number C350C104J1G5CA (100 V rating). These capacitors are made with a non-ferroelectric ceramic. To evaluate the their stability, seven 100 nF capacitors were temperature cycled in an environmental chamber. The leads connecting the capacitors had a capacitance of only 100 pF and so did not contribute any error to the measured variation. Figure 2.7 shows the temperature response from −50 to +100°C measured at 100 Hz. All of the capacitors were within the 0 ±30 ppm/°C limits. In fact, all but one were remarkably better at approximately −7 ppm/°C. The anomalous capacitor had a higher than average capacitance value and was not used in the integrator construction.

The capacitors' dissipation factors are also critical parameters for the phase stability of the integrator. The dissipation factor is the ratio of the capacitor's resistance to reactance [31], often written as $\tan(\delta)$ where δ is the deviation of the current-to-voltage phase relationship from a perfect 90° lead. The dissipation factor

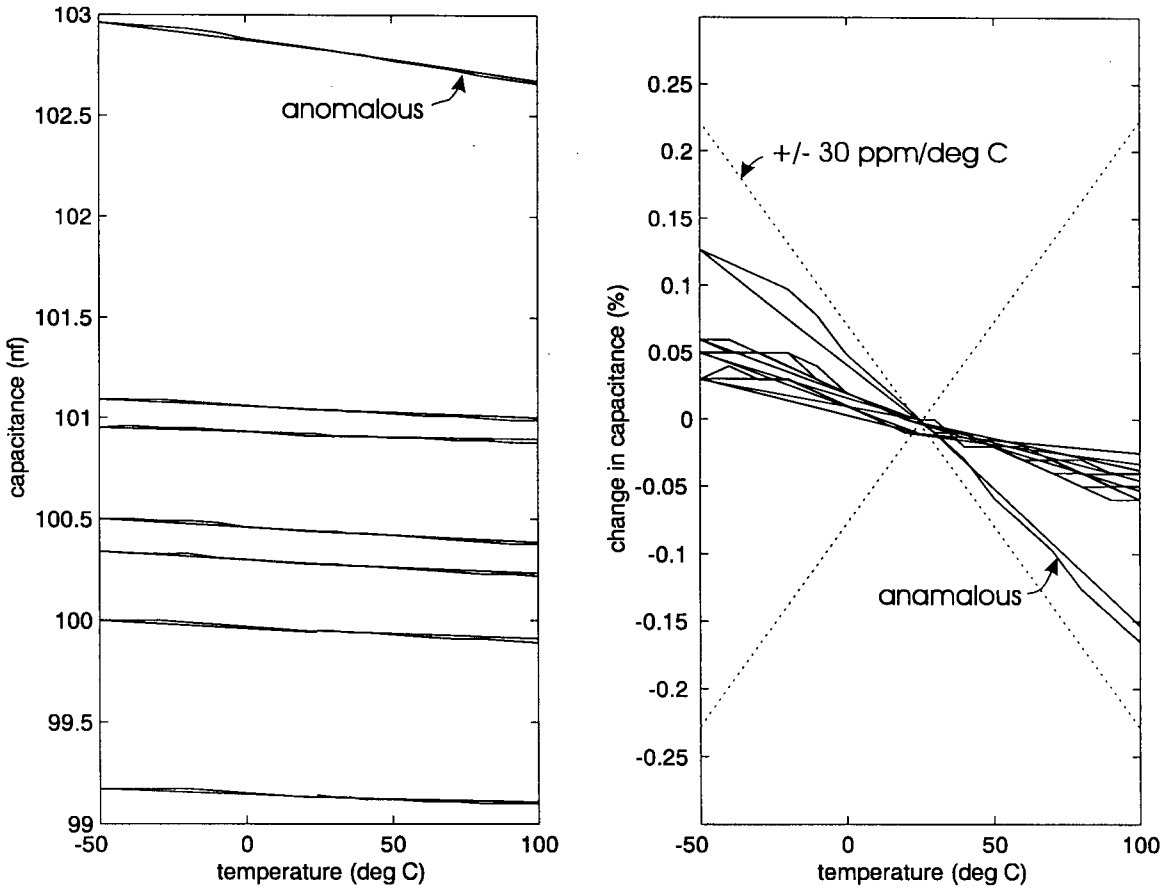

Figure 2.7: Temperature response of the KEMET COG ceramic capacitors. The COG limits of 0 $\pm$ 30 ppm/°C are also shown at the right. One capacitor is seen to be anomalous, but still within COG limits.

was measured over temperature for the seven KEMET capacitors. The worst value was 4E-4, corresponding to a phase error of 1.4 minutes, which occurred at $-50°C$. The dissipation factor reached a minimum for all capacitors near 0°C at approximately 1.8E-4, or 0.4 minutes. This represents a net variation in phase of 1 minute and is acceptable in the context of achieving an overall phase error of ± 8 minutes to comply with the IEEE C57.13 standard [18].

With all of the components selected, a printed circuit board (PCB) was laid out for the integrator and manufactured by AP Circuits, Calgary, AB. Although the component count is small, the layout was done on a double sided board so that, where possible, a current return path could be placed directly beneath the signal traces to minimize mutual inductance. The components' leads were all carefully aligned with the PCB holes to maximize stability by minimizing the stress on the components. The capacitance value of C_1 was left at 91.67 nF (measured), i.e., less than the nominal value of 95 nF, so that it could be trimmed to null the integrator's phase.

The finished integrator was tested with the Keithley DAS1802HR to determine its amplitude and phase response. The phase error of the DAS1802HR setup when comparing two substantially in-phase signals was determined to be ± 1 minute near 60 Hz provided that the two signals were of comparable amplitude and source impedance. For this reason, the test configuration shown in Figure 2.8 was constructed to ensure these conditions were met. A high-voltage amplifier, model 3211 from New Focus Inc., San Jose, CA, capable of generating 400 V_{pp} at frequencies up to 500 kHz, was used to provide sufficient signal strength to overcome the integrator's attenuation. The reference signal was obtained from a resistive divider that was set

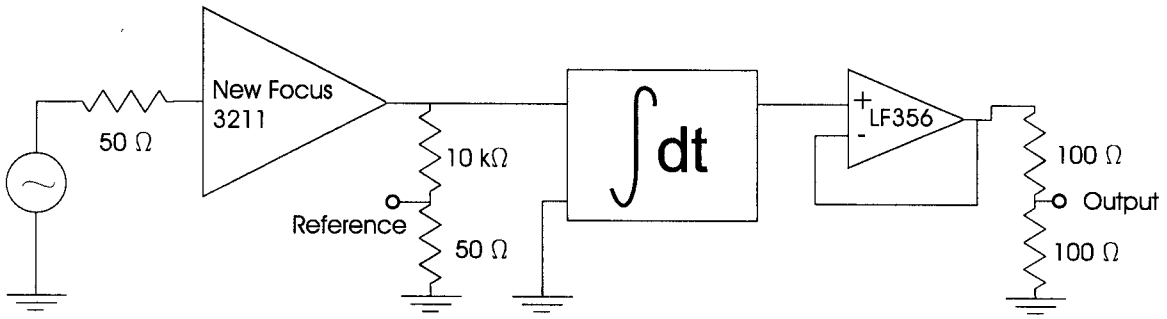

Figure 2.8: Integrator test configuration used to provide comparable impedance and signal level inputs for the Keithley DAS1802HR analog to digital converter.

to give a signal amplitude comparable to that of the integrator output at 60 Hz. The integrator was followed with an LF356 unity gain buffer from National Semiconductor, Santa Clara, CA, selected for its high input impedance, and a resistive divider to give an output impedance matched to the reference impedance.

The test circuit was used first to trim the value of C_1 to null the integrator's phase. This was done at 65 Hz to avoid 60 Hz power line interference. An extra 3 nF was added to bring the total capacitance to 94.67 $\pm$0.05 nF, resulting in a measured phase of 0 $\pm$1 minute. The calculated value for C_1 to null the phase, using the measured values for the other components, was 94.6 nF, showing excellent consistency between the component measurements and the phase measurements.

Figure 2.9 shows the resulting ratio error as well as the absolute phase error for the finished integrator. The results are in good agreement with the expected response from Figure 2.4 with the 2 Hz integrator pole frequency. The magnitude response becomes noisy above 1 kHz because of the attenuation of the integrator, but otherwise the characteristics are as expected. The phase response is only slightly different from the theoretical values. There is a very slight overcompensation in phase resulting in

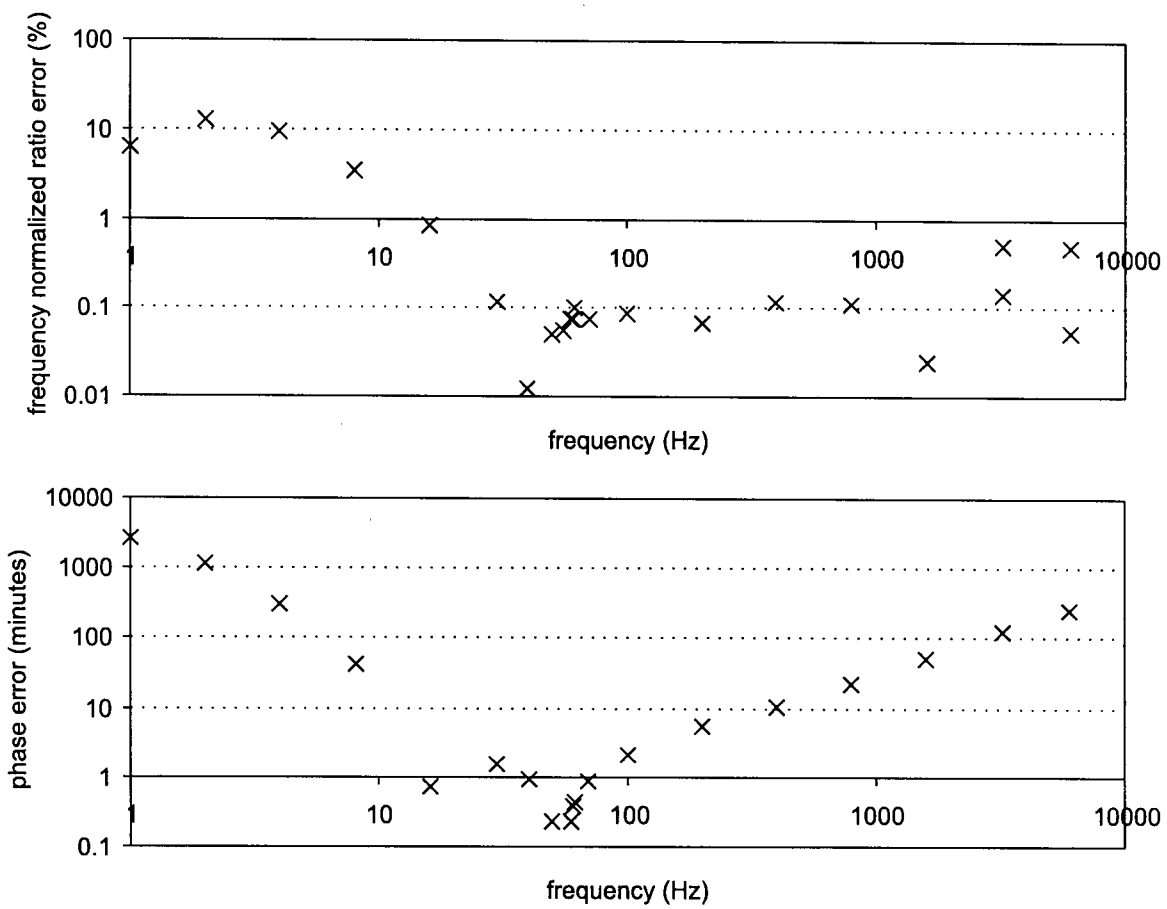

Figure 2.9: Magnitude and phase response of the passive integrator measured using the setup from Figure 2.8.

two phase nulls and a small phase lead between 10 and 60 Hz. Above 100 Hz, the phase error grows slowly rather than vanishing, reaching a lag of about 240 minutes (4°) at 6 kHz. The uncertainty in the 6 kHz phase measurement was not determined; however, the measurements in Chapter 5 show the final IOCT phase response to be well within the IEC and IEEE standards.

Chapter 3

IOPC for Current Sensing

3.1 Introduction

This chapter begins with the background and theory of the integrated-optic Pockels cell (IOPC). The subsequent sections detail the work done on the IOPC to make it suitable for the hybrid current sensor application. Various electrode structures were evaluated, with the aim of increasing the sensitivity of the IOPC, to give modulation levels compatible with the passive integrator. A significant portion of this work involved optimizing the low-frequency response to give ultrastable magnitude and phase accuracy at 60 Hz. The chapter concludes with a discussion of random and, in particular, correlated noise induced by vibrating the polarization maintaining fiber at the output of the IOPC.

3.2 Background and Fundamentals of the IOPC

The Pockels cell is a polarimetric device in which the relative phase delay of two orthogonal linear polarizations of light is modulated. The integrated-optic Pockels cell (IOPC) confines this interaction to a Ti indiffused lithium niobate waveguide that is sized to allow only the fundamental TE-like and TM-like modes to propagate (referred to from here on as the TE and TM modes) [14]. The TE and TM modes are polarized substantially normal to the direction of propagation with the TE mode having its dominant electric field component in the plane of the substrate, and the TM mode having its dominant electric field component normal to the substrate.

The direction of propagation is chosen to be along the optic axis of the lithium niobate crystal (lithium niobate is uniaxial). This results in both modes 'seeing' the same refractive index profile and thus having similar mode profiles [13]. The similarity of the mode profiles means that a superposition of the two modes will yield a relatively uniform polarization state and hence offer the potential for a high extinction ratio modulator. Another advantage of propagating along the optic axis is that both modes have nearly equal propagation constants, which differ slightly due to waveguide birefringence. Avoiding interaction with the material birefringence gives greater stability and predictability of the modal birefringence [13].

There are two choices in crystal cut that can be used when propagating along the optic axis: X-cut or Y-cut. To obtain efficient polarization modulation, the linear input polarization must be oriented at 45° with respect to the principal axes of the modulated optical indicatrix. This can be accomplished by using either an X-cut substrate with a horizontal modulation field applied in the Y direction, or a Y-cut

substrate with a vertical modulation field applied in the Y direction [32]. To convert the polarization modulation into an intensity modulation, a polarization maintaining (PM) fiber is oriented at 45° with respect to the X and Y axes at the output of the waveguide and functions as an analyzer. The optical powers in each mode of the PM fiber obey two complementary transfer functions, P_1 and P_2, relating the optical power to the modulating electric field [14]:

$$P_{1,2} = \frac{P_o}{2}\left[1 \pm \alpha \cos\left(\frac{E_y}{E_\pi}\pi + \phi_i\right)\right] \tag{3.1}$$

where P_o is the total optical power, α determines the on-off ratio, E_y is the electric field component parallel to the Y axis, E_π is the half-wave electric field, and ϕ_i is the intrinsic bias arising from the waveguide's modal birefringence. The intrinsic bias is given by:

$$\phi_i = 2\pi B^m l/\lambda_o \tag{3.2}$$

where B^m is the modal birefringence, l is the waveguide length, and λ_o is the free space optical wavelength. The half-wave electric field is given by:

$$E_\pi = \lambda_o/(2n_o^3 r_{22} L) \tag{3.3}$$

where n_o is the ordinary refractive index, r_{22} is the relevant electro-optic coefficient [33], and L is the electro-optic interaction length. Since the IOPC will be used here to transmit a voltage signal, the IOPC must have electrodes incorporated to replace E_y and E_π in Equation 3.1 by the applied voltage V_a and the half-wave voltage V_π. The relationship between the electric field and the voltage is determined by the particular electrode configuration.

3.3 Adapting the IOPC for Current Sensing

IOPCs fabricated previously at UBC have been targeted at high-voltage sensing. These devices are immersion type sensors that detect electric fields. Typical half-wave electric fields for these devices are on the order of several hundred kV/m. Since the purpose of the IOPC in this work is to measure the voltage from the Rogowski coil, an electrode structure is fabricated on the surface of the sensor substrate to give a fixed voltage-to-field relationship. Furthermore, to accommodate the attenuation of the passive integrator presented in Chapter 2, the IOPC should be made as sensitive as possible. The Rogowski coil also benefits from a more sensitive IOPC, since a smaller mutual inductance results in a higher self-resonance frequency.

The choice of electrode configuration depends on the choice of crystal cut. Initially, the main criterion for choosing between X-cut and Y-cut substrates was thought to be how effective the corresponding electrode structures were at creating a strong uniform electric field in the Y direction. In fact, as will be shown later, the choice of cut was dictated by the optical buffer layer properties. The two electrode configurations that were considered were a three-strip coplanar electrode for the Y-cut substrates and a two-strip version for the X-cut substrates (see Figure 3.1). Both configurations give a predominantly Y-directed electric field across the waveguide. An analysis of these structures will be performed to estimate achievable values for the half-wave voltage of the IOPC.

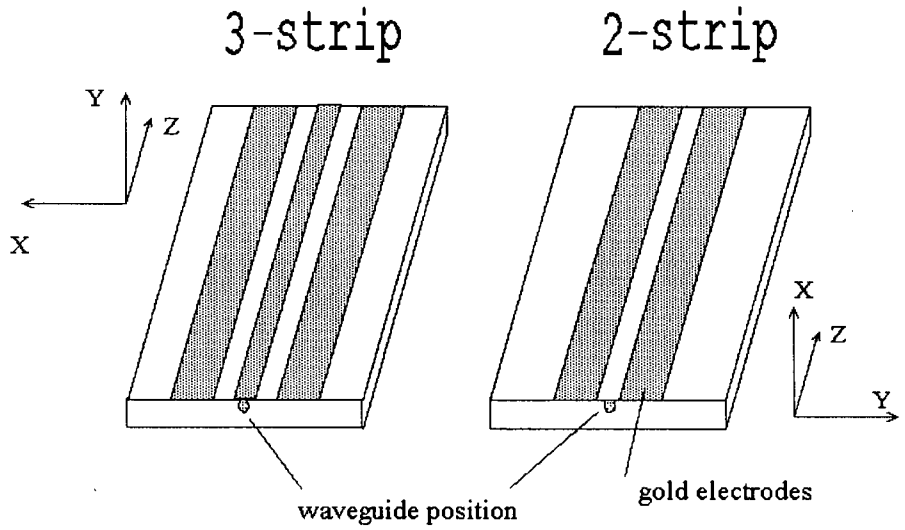

Figure 3.1: IOPC electrode configurations: a three-strip coplanar electrode on Y-cut (left) and a two-strip coplanar electrode on X-cut (right) lithium niobate.

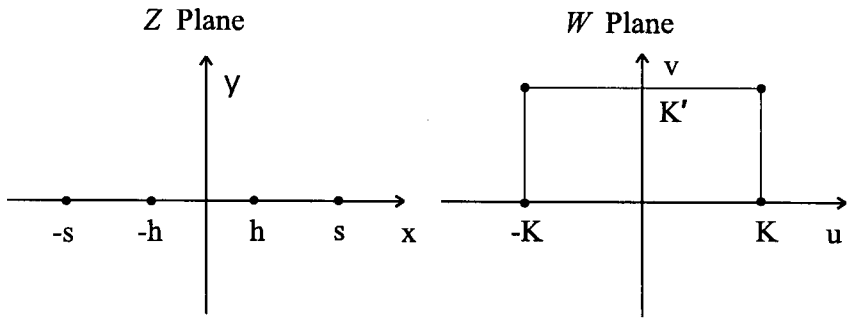

Figure 3.2: Conformal mapping from the Z to W planes.

3.3.1 Calculation of Electrode Fields

The method of conformal mapping was used to determine the electric fields generated by the electrodes. A variation of the Schwarz-Cristoffel formula [34] can map both of these electrode configurations into parallel plate capacitors, where the field is given by the voltage divided by the plate separation. This approach is presented in [35]; however, an error is made in [35] in the mapping of the three-strip electrode structure in which the electric fields are in error by a factor of one half. The formulas for the electric fields were derived using a form of the Schwartz-Christoffel formula:

$$w = F(z) = \int_0^z \frac{\mathrm{d}z}{h\sqrt{(1 - z^2/h^2)(1 - z^2/s^2)}} \tag{3.4}$$

where h and s are the points shown in Figure 3.2 and F is the mapping function from the Z plane to the W plane.

The points are mapped as follows: $z = h \rightarrow w = K$; $z = s \rightarrow w = K + jK'$; $z = \pm\infty \rightarrow w = 0 + jK'$. Symmetry is preserved for the left half-planes. Here j

denotes the square root of -1. The equations to describe the electric fields in the three-strip case will be developed below; the two-strip case is similar. For the three-strip electrode case, the region from $-h$ to h is the center electrode and is mapped to the bottom of the rectangle from $-K$ to K. h to s is the gap between the electrodes and is mapped to the side from K to $K+jK'$ (similarly, $-h$ to $-s$ is mapped to the side from $-K$ to $-K+jK'$). The outer electrodes are assumed to extend from $-s$ to $-\infty$ and from s to $+\infty$ and must be electrically connected. These regions form the top electrode in the W plane from $-K+jK'$ to $K+jK'$. The electric potential in the W plane can be now be written as:

$$V(u,v) = \frac{U}{K'}v \tag{3.5}$$

where U is the electrode potential, and u and v are the coordinates in the W plane. The electric field equations can now be written as:

$$\begin{aligned} E_x(z) &= \frac{\partial V(F(z))}{\partial x} \\ &= \frac{-U}{K'} Im\left\{\frac{\partial w(z)}{\partial z}\frac{\partial z}{\partial x}\right\} \\ &= \frac{-U}{K'} Im\left\{\frac{1}{\sqrt{\left(1-\left(\frac{z}{h}\right)^2\right)\left(1-\left(\frac{z}{s}\right)^2\right)}}\right\} \end{aligned} \tag{3.6}$$

and

$$\begin{aligned} E_y(z) &= \frac{\partial V(F(z))}{\partial y} \\ &= \frac{-U}{K'} Im\left\{\frac{\partial w(z)}{\partial z}\frac{\partial z}{\partial y}\right\} \\ &= \frac{-U}{K'} Re\left\{\frac{1}{\sqrt{\left(1-\left(\frac{z}{h}\right)^2\right)\left(1-\left(\frac{z}{s}\right)^2\right)}}\right\}. \end{aligned} \tag{3.7}$$

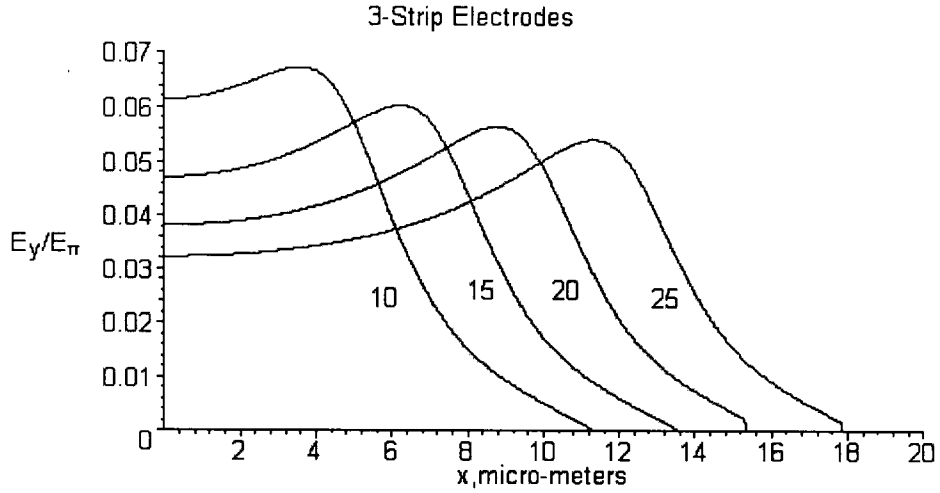

Figure 3.3: Y-directed electric field at a depth of 2 μm into the substrate for the three-strip electrode. Numbers indicate the middle electrode width in microns.

The electric field equations were evaluated using the software package Maple^{TM} from Maplesoft, Waterloo, ON. The results are shown in Figures 3.3 and 3.4 for several middle electrodes widths (three-strip case) and gap widths (two-strip case). The applied voltage is $U = 1$ V and the plot is normalized by E_π as calculated from Equation 3.3 using an electrode length $L = 10$ mm, $\lambda_o = 1.3$ μm, and $r_{22} = 5.4$E-12 m/V [36]. A gap of 10 μm was chosen for the three-strip electrodes while an electrode width of 50 μm was chosen for the two-strip electrodes. The field is plotted at a depth into the substrate of 2 μm, corresponding roughly to the location of the peak intensities of the guided modes. The estimated half-voltages are shown in Table 3.1.

As expected, the smaller center electrode or center gap yields the smallest half-wave voltage. Based on sensitivity alone, the best choice would be the three-strip configuration with the 10 μm center electrode. Although the three-strip configuration

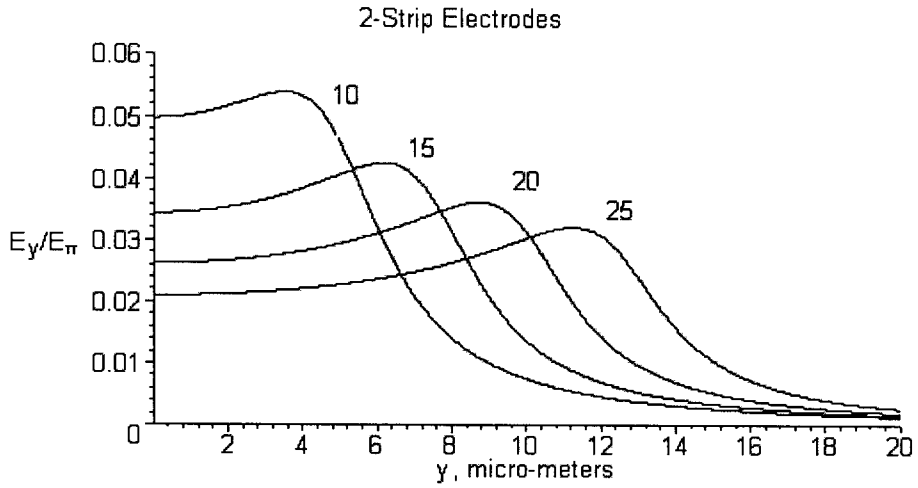

Figure 3.4: Y-directed electric field at a depth of 2 μm into the substrate for the two-strip electrode. Numbers indicate the electrode gap width in microns.

Table 3.1: Half-wave voltages for the three- and two-strip electrodes.

size (μm)	Vπ three-strip	Vπ two-strip
10	16	20
15	21	29
20	26	38
25	31	48

gives good sensitivity, it did not perform well in transient tests due to the optical buffer layer.

3.3.2 Optical Buffer Layer Considerations

The reason for using an SiO_2 buffer layer is to isolate the optical field from nearby electrodes [37]. The large index contrast between the SiO_2 and the lithium niobate (1.44 vs. 2.22 at $\lambda_o = 1.3$ μm) ensures that the evanescent optical field does not

interact with the metal, even when the metal is directly overtop of the waveguide. The generally accepted penalty for using a buffer layer is an increase in the half-wave voltage due in part to elevating the electrodes, but also because of a concentration of the modulating field inside the oxide which has a lower relative permittivity than the lithium niobate (3.9 vs. 84 [36]). Introducing a buffer layer typically increases the half-wave voltage of an integrated electro-optic lithium niobate modulator by 10 to 30 % [38].

In the course of fabricating and testing IOPCs for this work, it became apparent that the buffer layer had a significant impact on the low-frequency performance of the IOPC. A significant body of literature exists on the subject of "DC drift" in lithium niobate modulators for telecommunication applications. Research in this area has focused both on drift intrinsic to the lithium niobate [39, 40, 41, 42] as well as drift associated with buffer layers [43, 44, 45, 46]. For telecommunication applications, the biases of modulators are actively set by application of a DC voltage. Over time, the bias point has a tendency to relax, requiring an increase in the DC bias voltage. This situation is problematic if the bias voltage exceeds the supply limits. For the IOPC, DC drift is not a concern since biasing is achieved passively through modal birefringence. What is of concern is that the same phenomena leading to DC drift has been found to affect the low-frequency response of IOPCs. The effect can be so strong as to inhibit modulation altogether at 60 Hz, or in less severe cases, produce magnitude and phase errors.

The first IOPCs fabricated as part of this work (see Chapter 4) were made using Y-cut substrates and a three-strip coplanar electrode structure on top of a

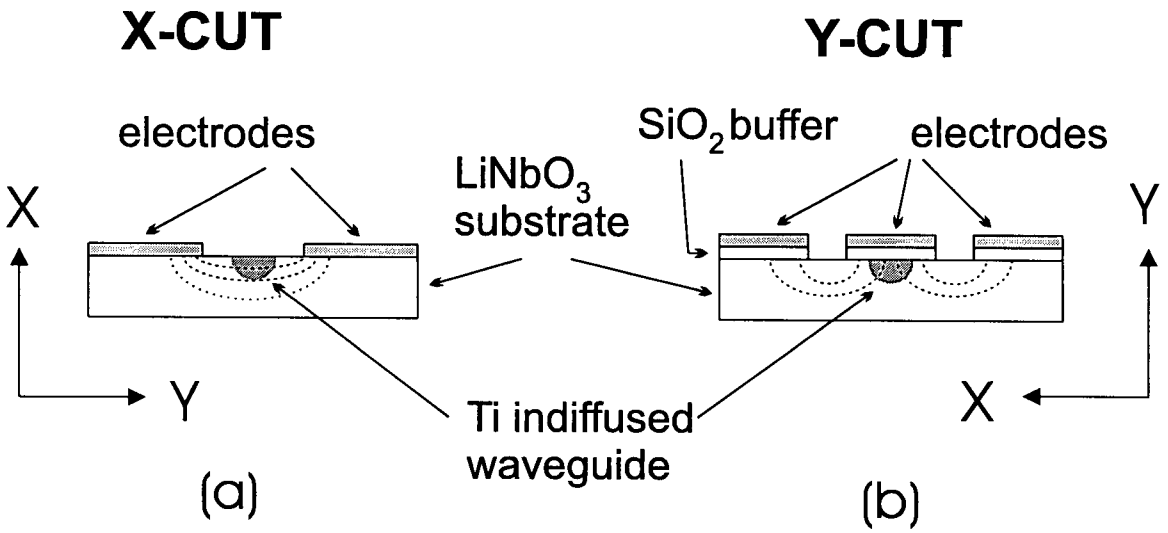

Figure 3.5: IOPC electrode configurations for X-cut (a) and Y-cut (b) lithium niobate.

continuous SiO_2 buffer layer. This configuration was found to behave as a high pass filter and was unusable for 60 Hz operation. The step response of this structure is shown in Figure 3.6. This step response was fit to a single time constant process with good agreement as shown in Figure 3.7 on a logarithmic time scale. The equation for the fit is:

$$P(t) = 1 + k[e^{-t/\tau} - 1] \tag{3.8}$$

where $P(t)$ is the normalized step change in optical power over time, $k = 0.96$ is the magnitude of the decay at infinity, and $\tau = 1.9\text{E-}5$ s is the time constant. Here the step response decays down to only 4 % well before the end of one power frequency cycle (17 ms). Clearly this is not a suitable modulator for 60 Hz instrumentation.

To try to defeat the charge screening effect, all of the SiO_2 was etched using buffered HF from between the electrodes (see Figure 3.5b) to prevent charge migration from one electrode to the other. Complete removal was verified using an Alphastep

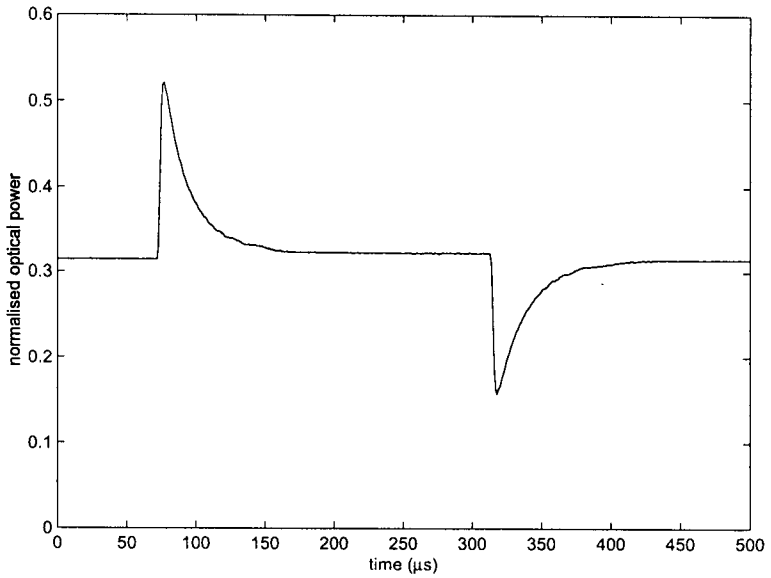

Figure 3.6: Step response of a Y-cut IOPC with an SiO_2 buffer layer and a three-strip coplanar electrode. The response is normalized to the total optical power.

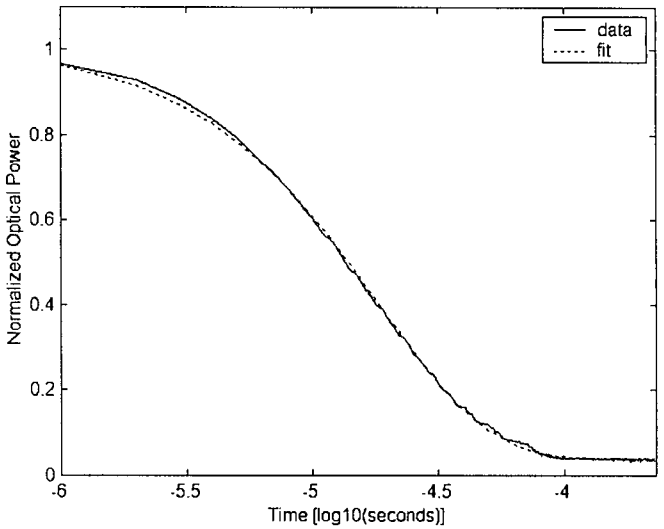

Figure 3.7: Single time constant fit to the step response of Figure 3.6.

200 Stylus Profilometer from Tencor, San Jose, CA, followed by an over etch. This technique was employed in [47] for a Mach-Zehnder type modulator to obtain DC stability. Despite the removal of SiO_2, all of the IOPCs that were fabricated in this manner possessed low-frequency time constants in response to a step in applied voltage. Figure 3.8 shows a typical response after etching and the corresponding fit given by:

$$P(t) = 1 - 0.092\exp(-t/0.033) - 0.076\exp(-t/0.35). \tag{3.9}$$

Although this response is much improved in that it will provide efficient modulation at power frequencies, there will be both magnitude and phase instability at 60 Hz. Equation 3.9, converted into a frequency domain transfer function, gives a phase lag of 33 minutes and a ratio error with respect to $f = \infty$ of 0.1 %.

The phase associated with Equation 3.8 was evaluated using the Laplace Transform to determine the allowable degree of transient behavior in terms of the phase response at 60 Hz. The result is shown as a contour plot in Figure 3.9 as a function of k and τ. The contour for 10 minutes of arc corresponds to the IEC 0.2 % accuracy class [19]. As expected, the phase error is most sensitive near the time constant corresponding to 60 Hz, or -2.6 in log seconds. The magnitude of a transient having this time constant must be less than -22 dB in optical power to satisfy a 10 minute phase error. Since none of the Y-cut IOPCs fabricated in the course of this work could achieve the desired phase response, subsequent fabrication efforts used X-cut lithium niobate substrates.

X-cut IOPCs were fabricated initially using a buffer layer beneath the electrodes to see if the change in geometry from the Y-cut devices would improve the

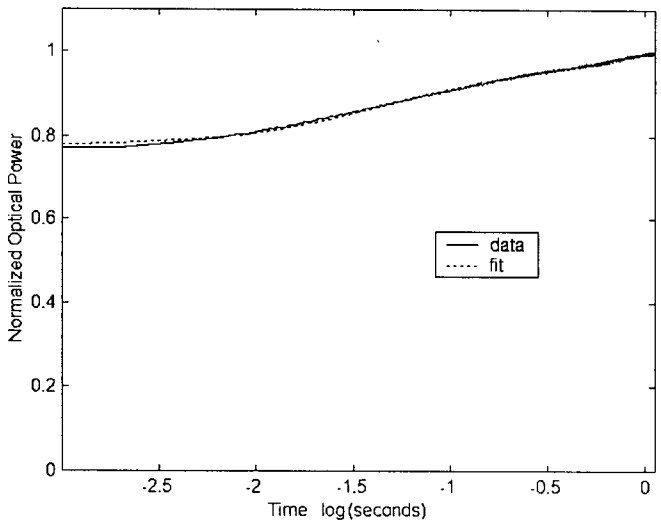

Figure 3.8: Step response for the three-strip electrodes on Y-cut lithium niobate with the SiO_2 buffer removed from between the electrodes.

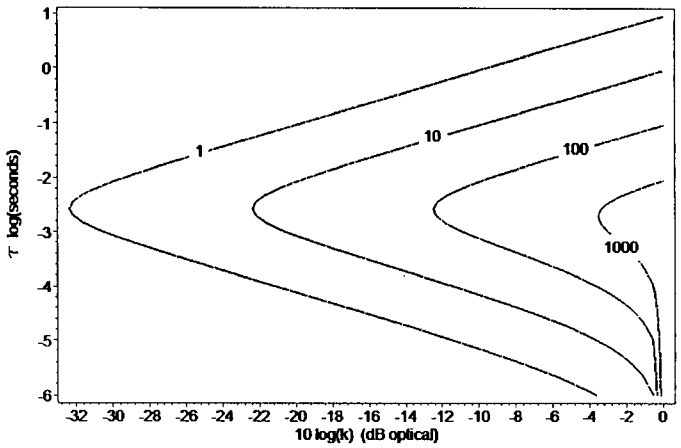

Figure 3.9: Phase contours in minutes at 60 Hz as a function of τ and k for a single time constant process obeying Equation 3.8.

low-frequency behavior. As before, the modulation decayed to zero. Depositing the buffer on top of the electrodes produced better results but still a transient was present with a magnitude of $k = -20$ % and a time constant of 250 ms (note: a negative value of k represents an increasing modulation with time.) Subsequently, removing the buffer by wet etching in buffered HF resulted in a transient decay with a magnitude of $k = +20$ % and a time constant of 50 ms. Further attempts at etching the surface in buffered HF as well as reactive ion etching (RIE) with CF_4 were unsuccessful in eliminating the transient. This result indicates that the transient behavior of these devices is sensitive to the condition of the lithium niobate surface between the electrodes.

On subsequent fabrications, the surface of the lithium niobate was disturbed as little as possible. SiO_2 was deposited only at the ends of the waveguides where adhesives are used in fiber bonding (see Chapter 4.) A shadow mask was used in this step to avoid contamination of the electrode region. The electrodes were pattered using a lift-off process instead of etching for the same reason. The step response was dramatically improved over the Y-cut IOPCs as seen in Figure 3.10. Curve fitting to this response shows the magnitude of transients to be on the order of -27 dB. Inspection of Figure 3.9 shows that this is sufficient to obtain phase errors less than 10 minutes of arc for any time constant. Direct measurement of the phase on six different IOPCs at 60 Hz, using the Keithley DAS1802HR analog to digital converter, produced values ranging from -2 minutes to $+2$ minutes.

A drawback of having no optical buffer layer is that the electrodes must be far away from the optical field to avoid optical absorption. It was found empirically that

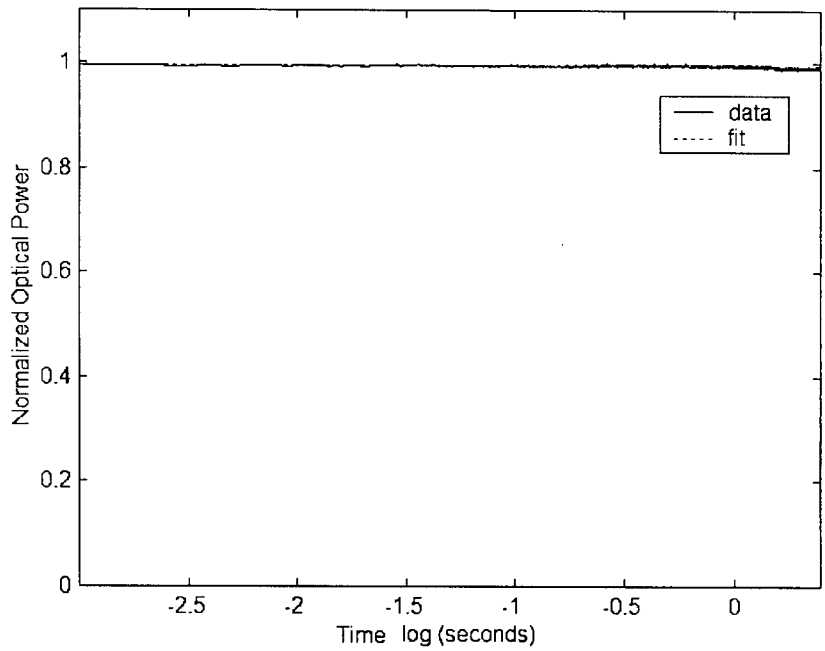

Figure 3.10: Step response for the two-strip electrodes on X-cut lithium niobate with no buffer layer.

electrode gaps of 15 and 20 μm suffered from differential mode loss (the TM mode being lossier) of approximately 2 dB, while the 25 and 30 μm electrode gaps could provide, on average, zero differential mode loss for 22 mm long electrodes.

3.4 Modulation Depth and System Noise

There are two types of noise that impact the performance of the IOCT: random noise and correlated noise. Random noise is introduced by the optical source and detector circuit. This imposes a minimum modulation depth to achieve a given signal to noise ratio (SNR). The new standard for electronic current transducers, IEC 60044-8, spec-

ifies a minimum SNR of 30 dB at rated current [20]. For revenue metering, random noise is filtered out, provided the integration time is sufficiently long. Correlated noise on the other hand will not average to zero and so is of particular concern. This section briefly discusses the sources of random noise in the IOCT, followed by an investigation into correlated noise caused by vibrating the PM fiber at the output of the IOPC.

3.4.1 Random Noise

The two fundamental random noise sources for the optical detector circuit following the IOPC are shot noise and Johnson noise [48]. Shot noise results from the statistical process of electron-hole pair generation in the detector's photodiode. Johnson noise, or thermal noise, results from random thermal motion of electrons in resistive elements. The equation for shot noise current is:

$$i_{ns} = \sqrt{2eRP_{rx}\Delta f} \tag{3.10}$$

where e is the charge of an electron, R is the photodiode responsivity, P_{rx} is the received optical power, and Δf is the noise equivalent bandwidth of the detector. For the typical receiver power used here of 10 μW and an analog bandwidth of 50 kHz, this amounts to 360 pA, or an SNR of 87 dB (electrical) using a photodiode responsivity of 0.8 A/W.

Thermal current noise becomes significant at low receiver powers. The thermal noise current is given by [48]:

$$i_{nt} = \sqrt{\frac{4k_BT}{R_L}F_n\Delta f} \tag{3.11}$$

where k_B is Boltzmann's constant, T is the temperature of the load resistor, R_L, and F_n is the noise figure of the receiver amplifier. Unlike shot noise, the thermal noise is independent of the received optical power and so sets the noise floor at zero optical power. For the receiver used here, the equivalent noise current referred to the input is below 200 pA, making shot noise the dominant noise source.

The optical source is an additional random noise source in the optical system. A broadband, super luminescent light emitting diode (SLED) was selected for the IOCT, primarily to avoid coherent noise as discussed in the following section. The fiber coupled power of this source is approximately 150 μW. The relative intensity noise (RIN) of these sources is on the order of -130 dB/Hz, or -83 dB (electrical) in a 50 kHz bandwidth. Allowing for a 40 dB (electrical) reduction at a modulation depth of 1 % at rated current leaves an SNR limit due to RIN of 43 dB.

The measured value for the signal-to-noise ratio for the full IOCT was 45 dB at the rated current of 3 kA. This value is 15 dB better than the minimum SNR specified in [20]. The most direct way of improving the SNR would be to increase the modulation depth; however, the modulation depth must be kept small to accommodate over-currents for protective relaying.

3.4.2 Correlated Noise

The primary source of correlated noise for the IOCT is vibration. The IOPC provides two complementary signals which allow fluctuations in the total optical power arriving at the photodetectors to be cancelled. This normalization suppresses common-mode signals but does nothing to reduce noise that appears as a differential modulation in

the two photodetector signals. A differential modulation will result if there is either a power exchange in the fast and slow modes of the PM fiber, or, a differential phase modulation followed by a misalignment of the polarizing beam splitter (see Chapter 4) with respect to the PM fiber axes. If the two PM fiber modes are coherent when arriving at the beam splitter, the misalignment will produce a differential intensity modulation. In the high-voltage substation environment, the differential phase of the PM fiber modes will fluctuate due to vibration and temperature changes.

Previous studies on polarization noise in PM fibers [23-27] have been largely targeted at communications applications in which a stable linear polarization state is transmitted in one axis of the fiber to reduce polarization noise in polarization sensitive receivers or to avoid polarization mode dispersion (PMD). The IOPC uses the PM fiber somewhat differently; the PM fiber must transmit and preserve substantially equal powers in both axes of the fiber. A further difference from communications applications is that low-frequency mechanical disturbances in a high-voltage substation overlap the bandwidth of greatest interest, namely 60 Hz and the lower ordered harmonics. An experiment was set up to quantify the impact of polarization noise on the IOPC.

The experimental setup consisted of a 5.3 m long PM fiber, part number FS-PM-6621 manufactured by 3M^{TM}, St. Paul, MN, with 1 m of the fiber fastened onto the cone of an audio speaker. A 1310 nm isolated DFB laser, part number MRLDSPD010I4PN-RAP7 from MRV Communications, Inc., Chatsworth, CA, was coupled to the PM fiber by a polarizing (PZ) fiber, part FS-PZ-6626 also from 3M^{TM}, oriented to launch approximately equal powers into the fast and slow axes of the PM

fiber. The output of the PM fiber was collected with a microscope objective, passed though an analyzer, and focused onto a photodetector, model 2011 from New Focus Inc., San Jose, CA. An 8-bit oscilloscope was used to measure the noise levels. To quantify the vibration, a mirror was bonded to the speaker cone to reflect a visible laser beam onto a wall. The displacement of the speaker cone was calculated as a function of the beam displacement. Figure 3.11 shows the dependence of the vibration noise on the speaker displacement at 60 Hz with the analyzer at 45° with respect to the PM fiber axes. This angle was chosen to maximize the polarization noise for the purpose of characterization. The bandwidth of the detector was set to pass frequencies from 10 Hz to 3 kHz. The noise level in the absence of vibration is -31 dB down from the DC level. Noise values are quoted here as $10\log(V/V)$, representing equivalent optical power, as opposed to electrical power.

Figure 3.12 shows a typical polarization noise waveform and its spectral content with 220 μm of vibration displacement at 120 Hz. Again, the analyzer is set to 45° with respect to the PM fiber axes. Clearly the noise generated is correlated to the driving vibration. The harmonic content of the correlated polarization noise is a function of the relative phase of the fast and slow modes in the PM fiber as well the magnitude of the phase modulation. Since differential phase modulation produces a sinusoidal amplitude transfer function at the analyzer, the harmonic content of the noise will vary in time as the relative phase of the PM fiber modes drift.

Figure 3.13 shows the noise measured as a function of the analyzer angle with 220 μm of displacement at 120 Hz. The analog bandwidth of the photodetector was set to 10 kHz for this measurement. The total noise reaches a minimum of -40 dB

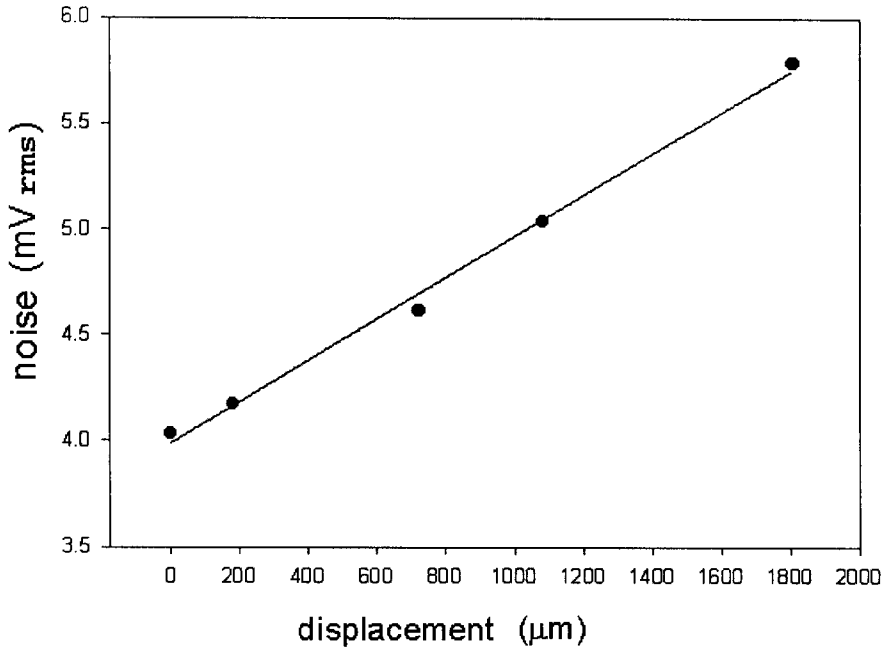

Figure 3.11: Measured photodetector noise voltage as a function of the peak to peak vibration displacement of the PM fiber at 60 Hz. The corresponding optical DC level is 4.7 V.

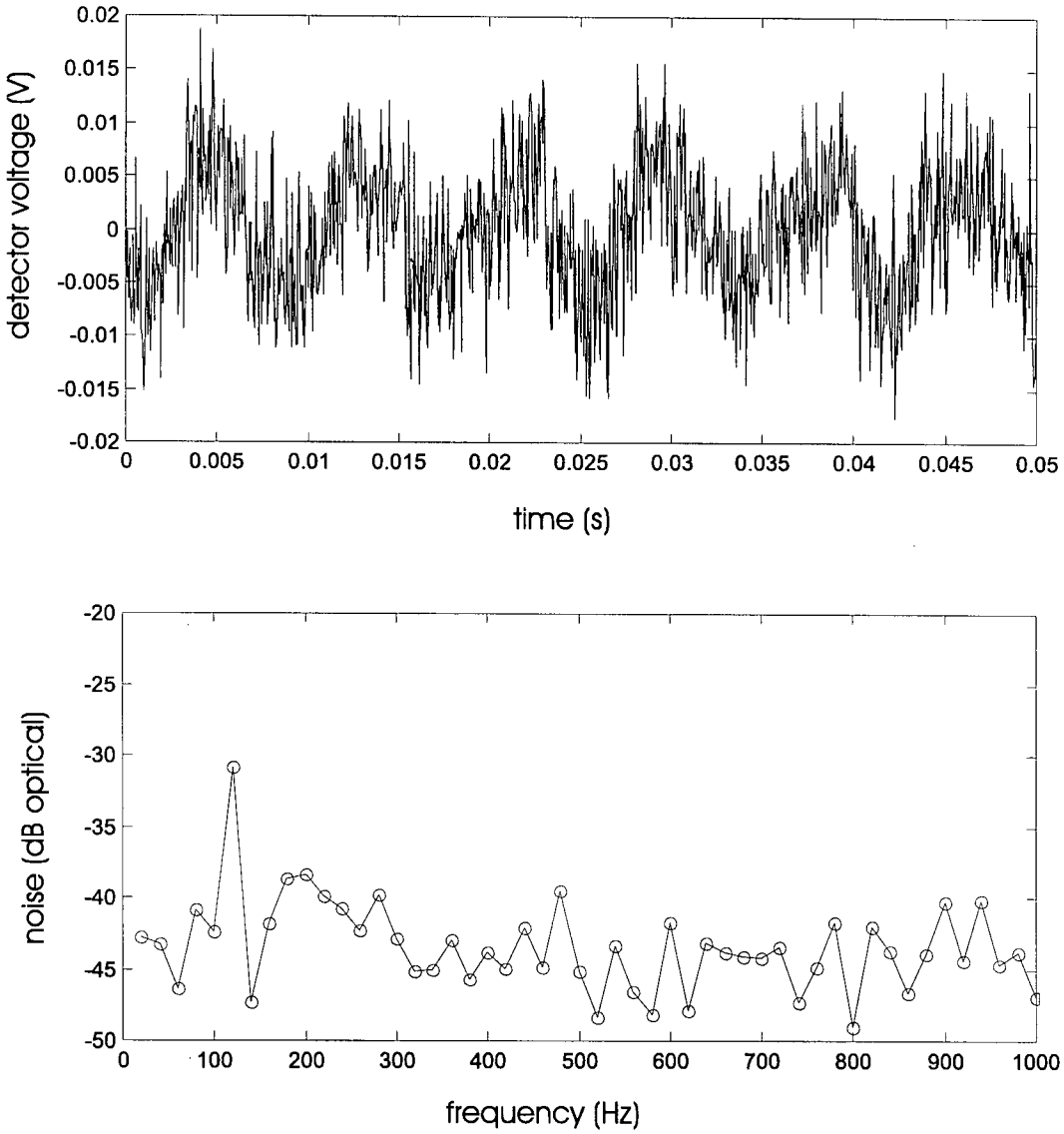

Figure 3.12: Typical polarization noise waveform and its spectrum with 120 Hz vibration at a displacement of 220 μm.

when the analyzer is aligned with the PM fiber axes at zero degrees. This measurement is limited by the noise floor of the system (laser+detector) which obscures the polarization noise. Spectral analysis gives a better indication of the amount of correlated noise at 120 Hz. The curve for the 120 Hz noise component, measured with a resolution bandwidth of 20 Hz, gives a noise value of -48 dB when aligned to the fiber axes. This value is comparable to the noise floor in the absence of vibration, meaning the noise power is not fully correlated to the vibration. It can be concluded nonetheless that a 1° misalignment of the analyzer gives a correlated signal at approximately -44 dB. The impact of the correlated noise on the IOCT can now be estimated.

The magnitude of the correlated noise determined above will now be expressed in terms of error current. The specified current range for the IEC 0.2 % accuracy class covers from 5 % to 120 % of rated current [20]. The optical modulation depth used in this work is approximately -20 dB at rated current, or -33 dB at 5 % of rated current. Using the value of -44 dB for the 120 Hz noise measured above, the 120 Hz signal appears as an error current of 8 % of the fundamental. The error in measuring the 120 Hz component of the primary current would of course be much larger, possibly 100 %. IEC 60044-8 specifies an absolute accuracy of 1 % for the second harmonic for the application of power quality metering [20]. Rather than try to achieve this level of accuracy by trying to obtain sub-degree alignment errors of the PM fiber, an alternate solution was sought.

The most practical solution to the polarization noise problem is to use a broadband optical source. If the optical path length difference between the fast and slow

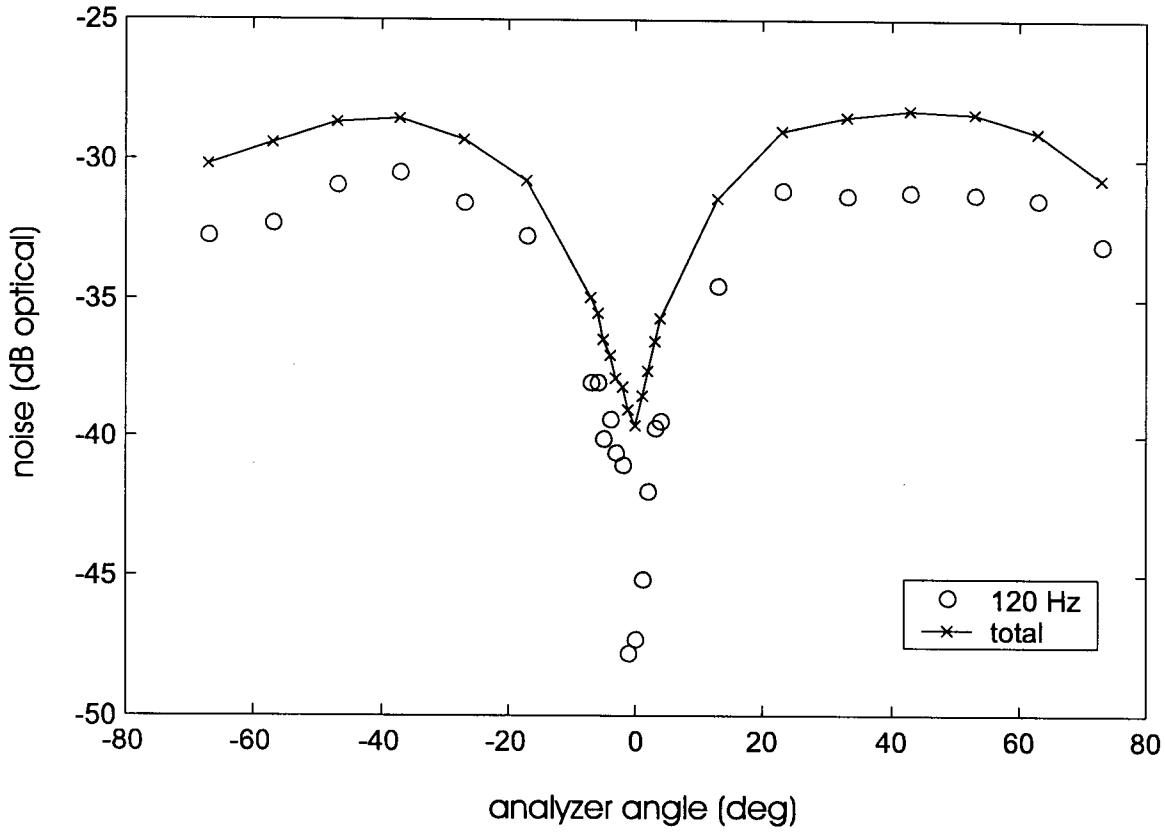

Figure 3.13: Noise in dB optical, referenced to the DC level, as a function of analyzer angle with 220 μm displacement at 120 Hz. Both the total noise power is shown as well as the 120 Hz component measured with a resolution bandwidth of 20 Hz.

axes of the PM fiber is longer than the coherence length of the source, the polarization state will not fluctuate regardless of any phase modulation induced by vibration. If the modal powers are equal, when the analyzer is oriented at 45°, the optical intensity obeys the interference function of the Michelson Interferometer [49] given by:

$$P(\tau) = P_o \left[1 + \exp\left(-\tau/\tau_c\right) \cos\left(2\pi f_o \tau\right)\right] \tag{3.12}$$

where P_o is the average optical power, τ is the time delay between the fast and slow modes, f_o is the optical frequency and τ_c is the coherence time given by

$$\tau_c = \frac{\lambda_o^2}{c\Delta\lambda_o} \tag{3.13}$$

where λ_o is the free space optical wavelength, $\Delta\lambda_o$ is the line width of the optical source, and c is the free space speed of light. The time delay τ is given by:

$$\tau = BL/c \tag{3.14}$$

where B is the birefringence of the fiber and L is the fiber length. Evaluating the exponential decay of the oscillations in Equation 3.12 for the FS-PM-6621 fiber, specified with a minimum birefringence of 3E-4, gives an attenuation of -23 dB/m in the coherent interference. The value of $\Delta\lambda_o$ used in this calculation is 30 nm, corresponding to the approximate line width of the thermo-electrically cooled 1310 nm super luminescent diode (SLED) provided by Nxtphase Corporation for this work. The thermo-electric cooling was essential since the small-signal sensitivity of the IOPC after bias drift correction was found to vary by 0.17 %/°C with the SLED temperature.

The length of PM fiber selected for the IOPC was 4 meters. This gives 92 dB suppression of polarization noise which is sufficient to lower the -44 dB of 120 Hz

correlated noise measured above down to -136 dB. Compared to the -34 dB nominal modulation depth at 5 % of rated current, the correlated 120 Hz noise is still negligible at -102 dB. The penalty for using the SLED is reduced optical power over what can be obtained with a laser, thereby increasing the relative contribution of the photodetector noise to the SNR. Nonetheless, the noise level is well within the allowable limit.

Chapter 4

Sensor Fabrication

4.1 Introduction

This chapter describes the fabrication of the Integrated-Optic Current Transformer (IOCT). The first section describes the fabrication of the IOPC from micro-fabrication to pigtailing and packaging. A step-by-step process list is given for the waveguide and electrode fabrication. The last section describes the current sensor housing. The housing for the first generation IOCT was constructed at UBC while the housing for the second generation IOCT was provided by Nxtphase Corporation.

4.2 IOPC Fabrication

This section describes the fabrication steps of the IOPC, starting at the wafer level, and concluding with the fiber pigtailing and packaging procedure. The wafer level fabrication steps were adapted largely from [50]. The steps described here are for the design that achieved the best performance in terms of frequency response and

stability. This design used an X-cut configuration with coplanar electrodes on either side of the waveguide. The structure is shown in Figure 4.1. An SiO_2 buffer layer was used to prevent the optical mode from interacting with the epoxy used to bond the fiber bonding blocks to the substrate. In the absence of the buffer layer, the differential mode loss was found to be unstable, drifting by as much as 1 dB if the IOPC was baked at 100°C for 2 hours.

A further design feature, used here to improve stability, is the incorporation of a Y_2O_3 anti-reflection (AR) coating. Although the AR coating improves optical insertion loss and reduces waveguide Fabry-Perot resonances, the primary reason for the AR coating here is to provide increased conductivity on the Z-directed end-facets. Lithium niobate generates a significant electric field (on the order of 20 kV $m^{-1}{}^{\circ}C^{-1}$), due to pyroelectric charge, on the Z facets in response to a temperature change [51]. Bias instability in lithium niobate sensors has been attributed, in part, to pyroelectric discharge [52]. Pyroelectric discharge is proposed here as the mechanism for the bias jumps seen in Section 5.7. Although the bulk conductivity of evaporated Y_2O_3 is expected to be significantly larger than the conductivity of lithium niobate (3E$-$10 $\Omega^{-1}m^{-1}$ [53] vs. 1E$-$13 $\Omega^{-1}m^{-1}$ [51]) it is anticipated that the surface conductivity between the Y_2O_3 layer and the lithium niobate will further help to evenly distribute the pyroelectric charge. Finally, to dissipate the pyroelectric charge, a trace of conductive grease was applied to the finished IOPC to electrically connect the two facets via the gold electrodes. An unused pair of electrodes from an adjacent waveguide was used for this purpose to avoid possibly shorting out the active electrodes.

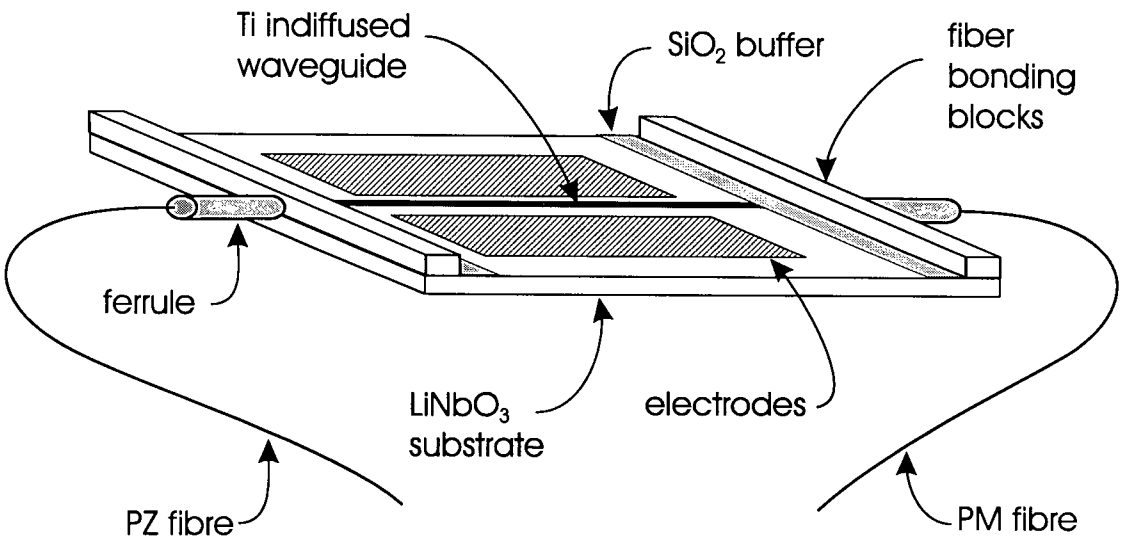

Figure 4.1: Illustration of the X-cut IOPC with attached fibers.

4.2.1 Mask Designs

Two generations of masks were made in the course of this work. The first generation was based on the three-strip coplanar electrode structure for Y-cut substrates while the second generation was based on the two-strip coplanar electrode structure for X-cut substrates (see Chapter 3). Both mask sets were made by Adtek Photomask, Montreal, QC, using electron beam writing with a 0.1 μm address size on 0.12 by 6 by 6 inch soda lime glass. The finished mask plates were cut into four quadrants, giving four unique mask patterns.

The first mask plate contained two waveguide masks and two electrode masks: a positive and negative of each, to give flexibility in the photolithographic process. The waveguide masks define the Ti prediffusion width which ranged from 6 to 7.9 μm in 0.1 μm steps. The spread of preduffusion widths was included to vary the modal birefringence so that a device with the correct bias point would be obtained [13].

The waveguides were placed on a 100 μm pitch. There were 15 repetitions of the prediffsion width variation across the mask. The electrode masks had five different central electrode widths: 10, 15, 20, 25 and 30 μm. Each combination of prediffusion width and electrode width was repeated three times across the mask.

The second mask plate was generated with four unique 3 by 3 inch quadrants for making X-cut IOPCs. The waveguide mask was similar to the first generation but covering 6.1 μm to 7.9 μm Ti prediffusion widths. The image polarity was dark field. The electrode mask was also generated as a dark field pattern with the two-strip coplanar electrode configuration. There were five different electrode gap widths: 10 μm to 30 μm in 5 μm steps. The other two quadrants of the mask plate were used for an off-axis propagation experiment that is the focus of Chapter 6. This portion of the mask consisted of waveguides and electrodes that were intentionally misaligned to the propagation axis in a range from $-1°$ to $+1°$ in $0.1°$ steps.

The mask drawing files were generated by writing C++ and Maple^{TM} code to automate the layout process and to facilitate design revisions. The Maple^{TM} code was particularly useful for the off-axis propagation experiment section of the mask which contained over 280,000 rectangles to create the shallow angles on a 0.1 μm rectangular grid. The C++ code generated rectangle patterns in the DXF format which is readable by Autocad from Autodesk Inc., San Rafael, CA, and is an acceptable format for transmission to Adtek Photomask.

4.2.2 IOPC Fabrication Steps

The lithium niobate fabrication was performed at UBC's Center for Advanced Technology in Microelectronics (CATM). The steps are given below for the X-cut fabrication. The substrates used in this work were 3 inch wafers of congruent lithium niobate from Crystal Technology, Palo Alto, CA. The wafers were cut into quadrants prior to processing. The processing steps were as follows:

1. Ti Deposition

   (a) The quadrant was cleaned under a fume hood in warm trichloroethelyne, warm acetone, and finally warm isopropanol for 5 minutes each with the last two minutes under ultrasonic agitation.

   (b) Ti was evaporated to a thickness of 800 Å using a model Auto-Tech II thermal evaporator from CHA Industries, Fremont, CA.

2. Photoresist Patterning for Waveguides

   (a) Positive photoresist, S1813 from Shipley Company Inc., San Jose, CA, was spun onto the quadrant at 4700 rpm for 40 s to obtain a thickness of approximately 1.3 μm.

   (b) The photoresist was then pre-baked at 95°C for 25 minutes.

   (c) The photoresist was then exposed through the waveguide mask for 52 s using a wavelength of 320 nm and a power density of 25 mW/cm^2.

   (d) The photoresist was then developed in Shipley MF-319 developer and slowly agitated for 60 to 80 s.

(e) The quadrant was then rinsed in de-ionized water for 90 s and subsequently dried using compressed nitrogen.

(f) The photoresist was then post-baked at 120°C for 30 minutes for hardening.

3. Ti Etching

(a) The Ti layer was then patterned by reactive ion etching using a PK-12 RIE, PECVD, Plasma system from Plasma Therm Inc., Kresson, NJ. The sample stage was first pre-heated to between 50 and 55°C by running an Ar plasma at 150 W to provide a more consistent temperature during the etching process. After heating the stage, the sample was loaded into the chamber and the chamber was evacuated. The Ti was then etched in CF_4 and Ar with the following parameters: CF_4 - 20 sccm/min, Ar - 20 sccm/min, pressure - 0.112 torr, power - 150 W, and a time of 10 minutes.

(b) The Ti layer was then inspected visually for etch completion, and etched again for another 2 minutes if necessary. An additional 2 mininute etch was used after the sample was visually clear of Ti to ensure complete removal.

(c) The photoresist was then removed using Shipley Microposit Remover 1165. This was done in two steps. A first beaker of remover was heated to between 40 and 50°C. A second beaker of remover was heated to between 50 and 60°C. The sample was placed in each beaker for 5 minutes with the last minute under ultrasonic agitation.

(d) The sample was then rinsed in heated de-ionized water (between 35 and

45°C) with ultrasonic agitation for 1 minute. The sample was subsequently dried using compressed nitrogen.

4. Ti Diffusion

   (a) The sample was then heated slowly ($\sim$ 20°C/min) to 1050°C in a Mini-Brute furnace from Thermco Products Corp. with an ANA-LOCK Series 201 controller. The furnace tube had a diameter of 2.5 inches and was flooded with O_2 at a flow rate of 1 l/min. The ramp rate was controlled by manually switching the breaker for the heating element up to 400°C, and by manually stepping the temperature set point from 400°C to 1050°C.

   (b) The diffusion temperature was maintained at 1050°C for 8 hr.

   (c) The furnace was then cooled in the reverse procedure to the heating cycle, leaving the O_2 flowing until 200°C was reached.

5. Electrode Deposition

   (a) Positive photoresist (Shipley S1813) was spun onto the quadrant at 4700 rpm for 40 s.

   (b) The photoresist was then baked at 70°C for 20 minutes.

   (c) The photoresist was then exposed through the electrode mask for 51 s.

   (d) The photoresist was then soaked for 8 minutes in chlorobenzene then blown dry with nitrogen.

   (e) The photoresist was then developed in Shipley MF-319 developer for 70 s.

(f) The quadrant was then rinsed in de-ionized water and subsequently dried using compressed nitrogen.

(g) An adhesion layer of 200 Å thick Cr was deposited using the CHA thermal evaporator. The starting vacuum was better than 2E-6 torr.

(h) Without breaking vacuum, a layer of Au was subsequently deposited to a thickness of 2300 Å to provide low resistance electrodes.

(i) The sample was then soaked in acetone until all the metal had lifted off.

(j) The sample was then rinsed in isopropanol and blown dry with nitrogen.

6. Optical Buffer Layer Deposition

(a) The sample was loaded into a Sputtering System model 3140, from Perkin-Elmer, Norwalk, CT.

(b) A shadow mask consisting of a scrap piece of $LiNbO_3$ was placed over the electrodes to prevent covering them with the buffer layer.

(c) The sample was then cleaned for 3 minutes in sputter-etch mode at 100 W in an Ar pressure of 1.8E-2 torr.

(d) Then, 3000 Å of SiO_2 was deposited in bias-sputter mode at 150 W. The time was 150 minutes and the Ar partial pressure was 1.5E-2 torr while the O_2 partial pressure was 0.3E-2 torr.

7. Laminating Fiber Bonding Blocks

(a) Two strips of $LiNbO_3$ were cut using a high-speed diamond saw, model 1006 from Micro Automation, Inc., to approximately 2 mm wide, and

sufficiently long to cover all the waveguides on the sample. The crystallographic orientation of these strips was controlled to be the same as the sample substrate.

(b) The strips were then attached to the sample with Epotek 353ND from Epoxy Technology, Billerica, MA. Excess glue was squeezed out using a small bar clamp.

(c) The epoxy was then cured in an oven for 2-3 hours at 95°C.

8. Cut and Polish

(a) The sample was cut into a rectangular block from the quadrant using the diamond saw.

(b) Each end of the sample was then polished using an Ecomet 4 polisher from Buehler, Lake Bluff, IL. The starting grit was 5 μm and the final grit was 0.3 μm.

9. Facet Coating

(a) The sample was loaded into an electron beam evaporator: model VE-400 made by Veeco Instruments Inc., Woodbury, NY, with a Perma Beam Source, model 150-0030 from Thermionic Laboratory, Inc.

(b) Y_2O_3 was deposited to a thickness of 1600 Å ($\sim \lambda/4$ @ 1310 nm) from a starting pressure of less than 5E-6 torr.

The most critical part of this process was variability in the critical dimension (CD) of the Ti prediffusion strip width. The patterned strip widths were measured

across the pattern and found to be as much as 2 μm smaller than the nominal width by the time the full pattern was etched through. This is equivalent to a 25 to 33 % loss in the Ti diffusion source for the range of nominal strip widths used here. Because of this, there was not a well defined process to obtain single mode waveguides. The fabricated waveguides were always checked for single mode operation before further testing and qualifications were done. Multimode waveguides were identified by offsetting the optical launch horizontally with respect to the waveguide to try to excite the second order mode. The mode composition was inspected at the waveguide output with a microscope objective and an Omega Meter, part number WM100B from Thorlabs, Inc., Newton, NJ.

4.2.3 IOPC Fiber Pigtailing

Pigtailing the IOPC proved to be a critical step in achieving stable sensor performance. The input fiber consisted of a 3 m length of polarizing fiber, part FS-PZ-6626 from 3M^{TM}, fusion spliced onto a 4 m long SM13 PANDA fiber, a polarization maintaining fiber made by Fujikura, Ltd., Tokyo, Japan. The fusion splice was performed by Nxtphase with care taken to obtain a greater than 30 dB extinction ratio. The PANDA fiber is less prone to developing micro-cracks than the PZ fiber when polishing, meaning the polarization state at the output of the PANDA fiber is expected to be more stable over time. For this reason, the PANDA fiber rather than the PZ fiber was bonded to the lithium niobate. The output fiber was a 4 m length of PANDA fiber.

The input and output fibers were prepared by bonding 900 μm diameter quartz

ferrules onto the fiber ends with the ultraviolet (UV) cure adhesive NOA 61 from Norland Products, Inc., Cranbury, NJ. The ferrules were then polished manually to a 0.3 μm finish. A teflon jacket, part R-STT-24 from Small Parts, Inc., Miami Lakes, FL, was added to the fibers for protection prior to attaching fiber FC connectors. A section of the jacket was removed from the fibers near the IOPC package to provide strain relief from the different thermal expansion coefficients of the fiber and jacket.

The input fiber was bonded first to the substrate. The equipment setup for the input fiber bond is shown in Figure 4.2. The axes of the input fiber were first rotated to obtain a linear polarization state at 45° to the TE and TM modes. After aligning the input fiber to the desired waveguide, the input fiber was rotated slightly to obtain equal modal powers at the waveguide output to compensate for any differential mode loss. The fiber was then backed away from the facet to apply a small bead of adhesive.

Initially the Norland NOA 61 was used to bond the fibers to the lithium niobate; however, temperature cycling tests conducted on the finished IOPCs showed problems in the 30 to 60°C range which coincides with the glass transition temperature range of the NOA 61 (see Section 5.7). A UV cure adhesive was subsequently obtained with a glass transition temperature of 80°C: Optodyne UV-2000 from Daikin Industries, Ltd., Osaka, Japan. The UV-2000 also has a much lower thermal expansion coefficient of 31 ppm/°C as compared to ~200 ppm/°C for the NOA 61.

The ferrule was brought into contact with the substrate after application of the glue. A mirror was used to visualize the interface with a microscope to obtain the optimum tilt on the ferrule to minimize the bond thickness. The curing was then performed with a UV Curing Lamp System, part number CS100 from Thorlabs. The

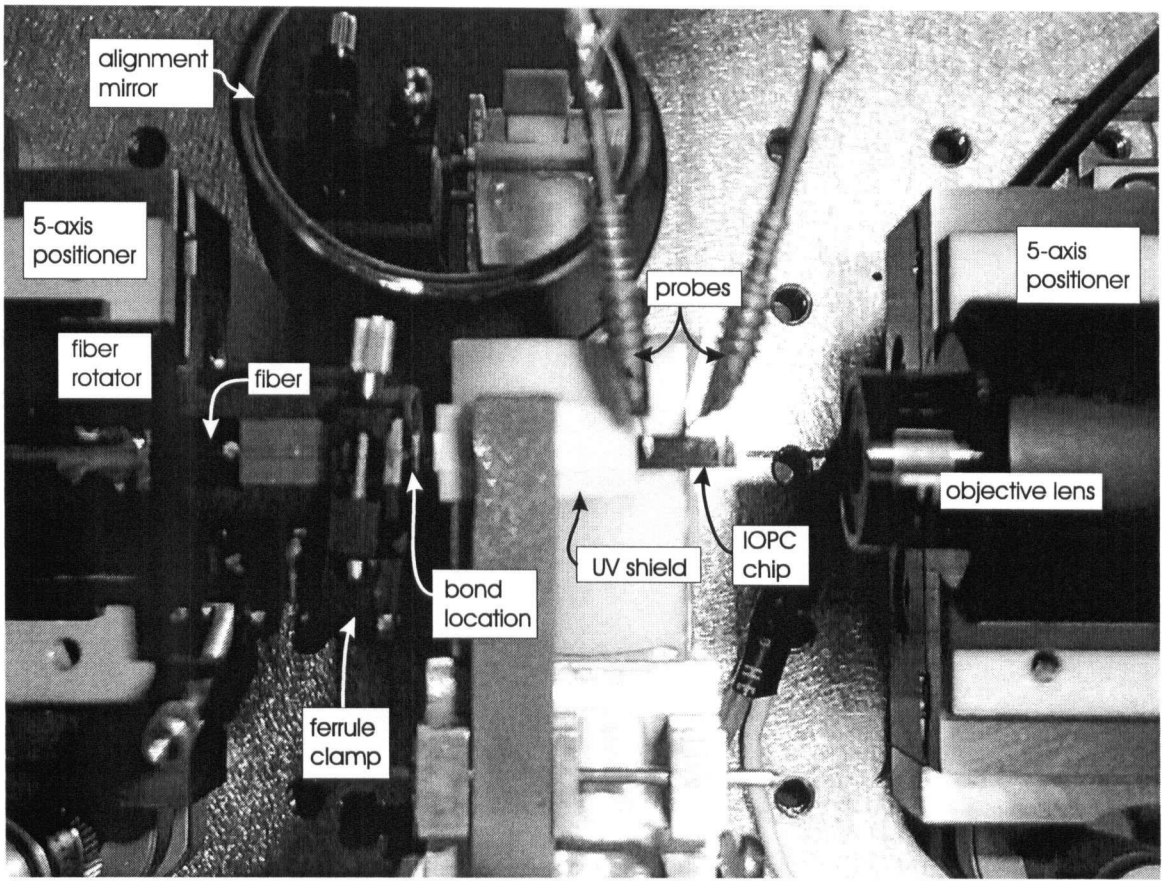

Figure 4.2: Fiber bonding station used to pigtail IOPCs. The station is set up in the photograph for bonding the input fiber.

cure time was approximately 10 minutes with a lamp distance alternating between 7 cm and 15 cm in one minute intervals so as not to overheat the parts and cause misalignment. A light shield was added to the setup to limit UV exposure of the substrate after it was found that the relative modal powers could be affected by exposure to UV radiation (see Figure 4.2).

The output fiber was bonded in a similar manner. The PANDA fiber axes were first aligned to 45° from horizontal at a second test station. The fiber was then aligned to the substrate and optimized for maximum coupling efficiency. Small rotational adjustments were then made as required to optimize the extinction ratio of the IOPC transfer function. The bonding then proceeded as for the input fiber. The best fiber-to-fiber insertion loss obtained on a pigtailed X-cut IOPC with this procedure was 4 dB, showing excellent coupling efficiency and low waveguide losses.

4.2.4 IOPC Packaging

The IOPC was found to be very sensitive to stress associated with packaging. The package is required to protect the IOPC as well as to bring electrical contacts onto the electrodes. The first package was made using 1/16 inch fiberglass, chosen for its low thermal expansion coefficient of ~15-30 ppm/°C in the plane of the fibers [54]. The lithium niobate substrate was secured into a cavity in the fiberglass using an ultra-low-stress adhesive, QMI 282 from Quantum Materials, Inc., San Diego, CA. QMI 282 is a graphite filled silicone with a modulus of elasticity below 2 MPa. The drawback to this adhesive is that it must be shipped and stored below −40°C to prevent self-curing. Despite the low-stress adhesive, the first package was unusable

due to stress problems. Simply attaching a 1/16 inch fiberglass lid to the package with four #2-56 machine screws flexed the package enough to change the optical bias point of the IOPC by approximately 50°.

The second package was made to be much more rigid than the first. Again fiberglass was used, but the thickness of the package was increased to 9.5 mm. A lithium niobate subcarrier was also used this time to increase mechanical isolation. It was cut from a 1 mm thick optical grade wafer with the crystallographic axes matched to the substrate because of anisotropic thermal expansion (15.4E-6 vs. 7.5E-6/°C in the Z and X directions respectively [55]). The QMI 282 adhesive was used at the fiberglass/subcarrier interface as well as the subcarrier/substrate interface. This new packaged IOPC showed no measurable bias change in response to manipulating the package, nor attaching fastening screws. This package is shown in Figure 4.3 with the lid removed. The contacts around the perimeter of the package are copper with evaporated gold to facilitate wire bonding. The wire bonding was done with a model 4123 wedge bonder from Kulicke & Soffa, Willow Grove, PA.

The beam splitter used in this work was provided by Nxtphase. It was aligned to the output PANDA fiber of the IOPC and oriented to give maximum extinction ratio before bonding. Exiting the beam splitter were two multimode fibers which transport the two complementary optical signals to two receivers. The two receivers were mounted in a six inch rack along with the DSP unit provided by Nxtphase. A 32-bit digital I/O board, part PCI-DOI-32HS from National Instruments, Austin, TX, was used to interface a personal computer to the DSP unit to acquire data.

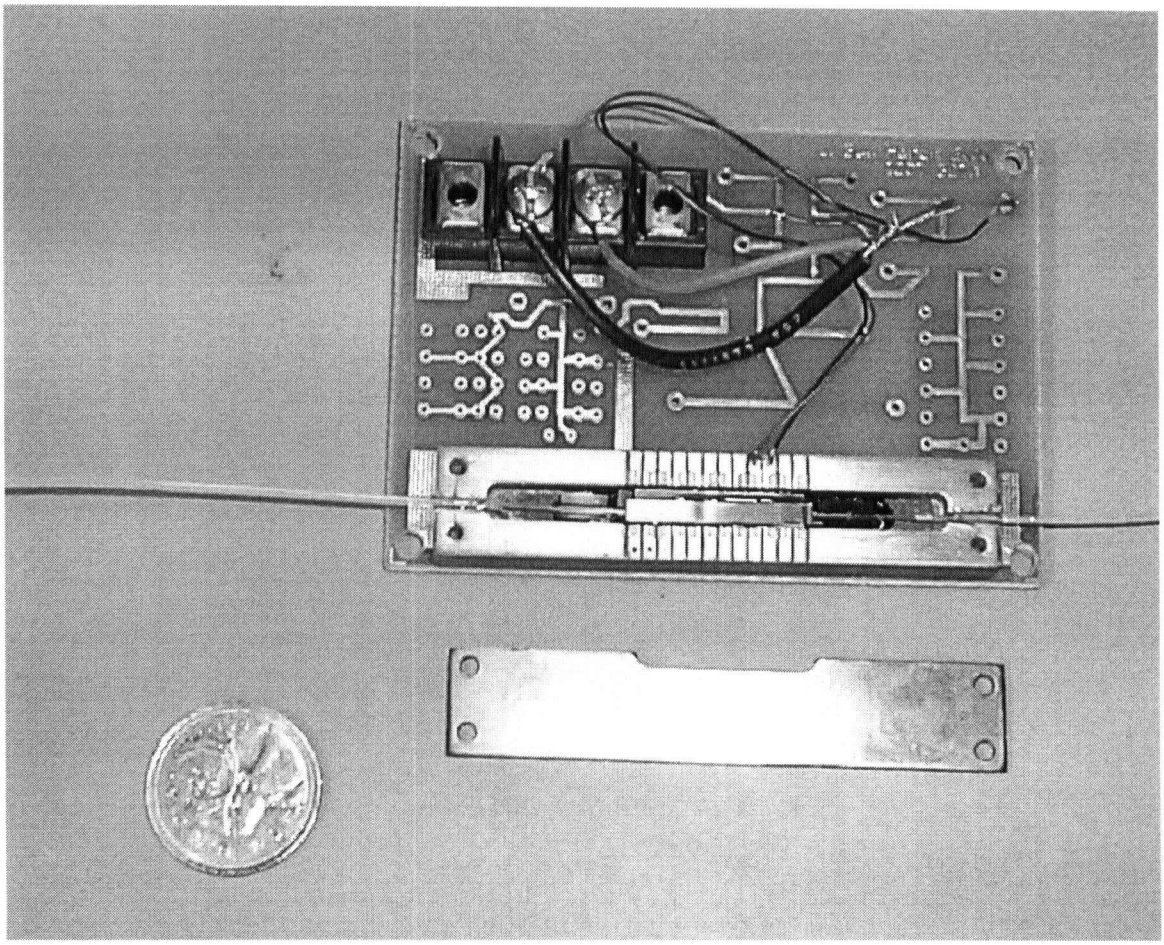

Figure 4.3: A pigtailed and packaged IOPC is shown with the cover removed. The package is sitting on an unpopulated passive integrator board.

4.3 IOCT Housing

The first generation IOCT was designed as a window type current sensor and constructed at UBC. The window diameter was 112 mm, sufficient to allow up to a 4 inch busbar to pass. The construction consisted of two main aluminum sections: a toroid to house the Rogowski coil, and a chamber at the base of the toroid to house the IOPC and integrator (see Figure 4.4). At the time of testing the first generation IOCT, the optimum IOPC design had not been developed and so an integrator was never installed. A Y-cut IOPC with parallel plate electrodes and a half-wave voltage of 507 V was installed in the IOCT housing. The output of this sensor was proportional to the derivative of the current.

The second generation IOCT was housed in a composite chamber with an integral busbar (see Figure 4.5). This housing was provided by Nxtphase and was subsequently customized at UBC to hold the integrator and IOPC. The IOPC and integrator were embedded in a thermally insulating styrofoam insert to minimize mechanical stress associated with rapid temperature change and temperature gradients. Initial high-current testing revealed a sensitivity to vibration with this housing (see Chapter 5). Subsequently the IOPC was mechanically isolated by mounting the styrofoam insert on a molded concrete ring with a mass of 3.3 kg in combination with a dense foam layer between the ring and the IOCT housing. The finished IOCT is shown in Figure 4.6 mounted on a 230 kV post insulator with two corona rings.

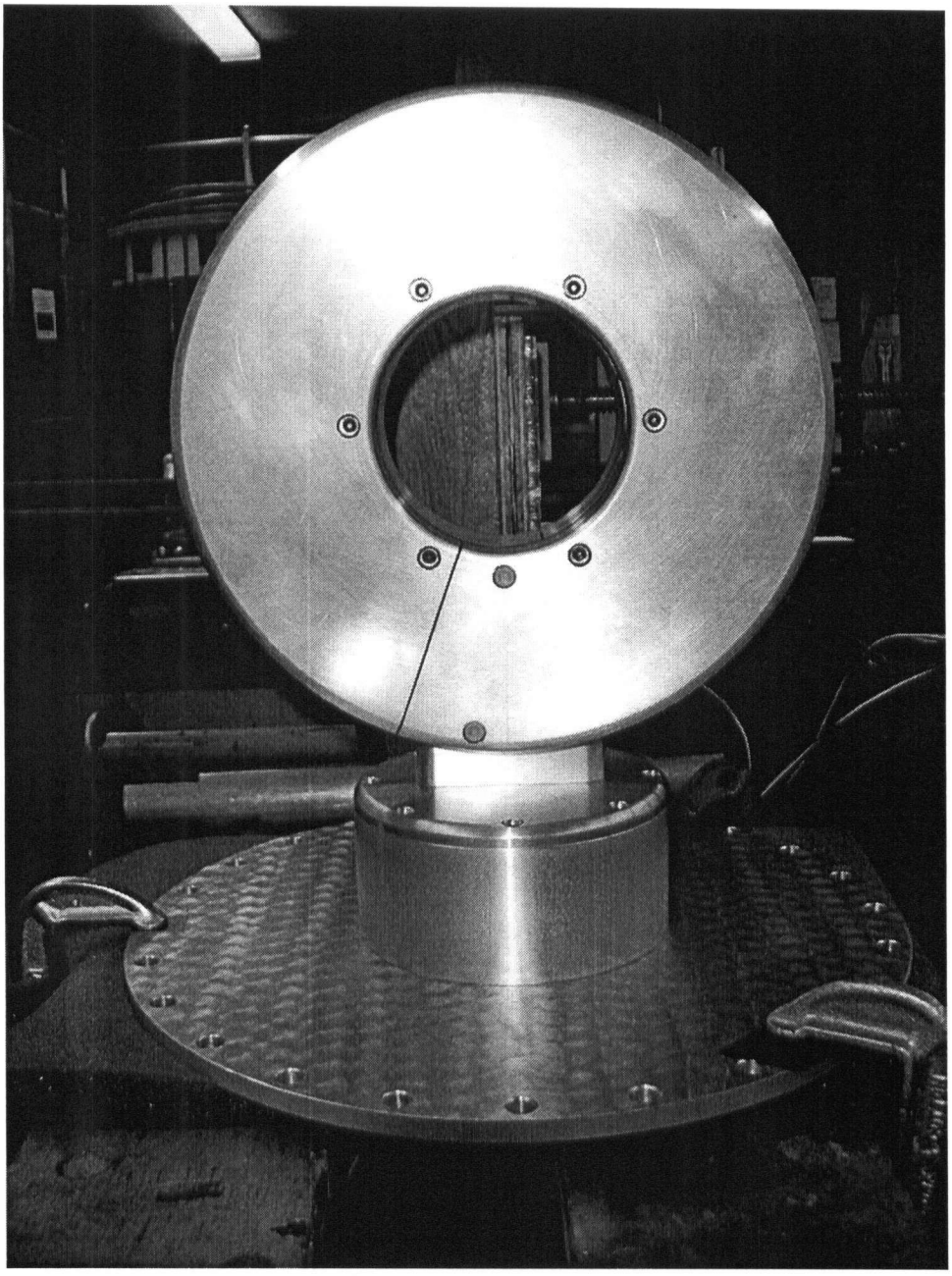

Figure 4.4: The first generation IOCT housing is seen here. The upper ring houses the Rogowski coil while the chamber at the bottom houses the IOPC.

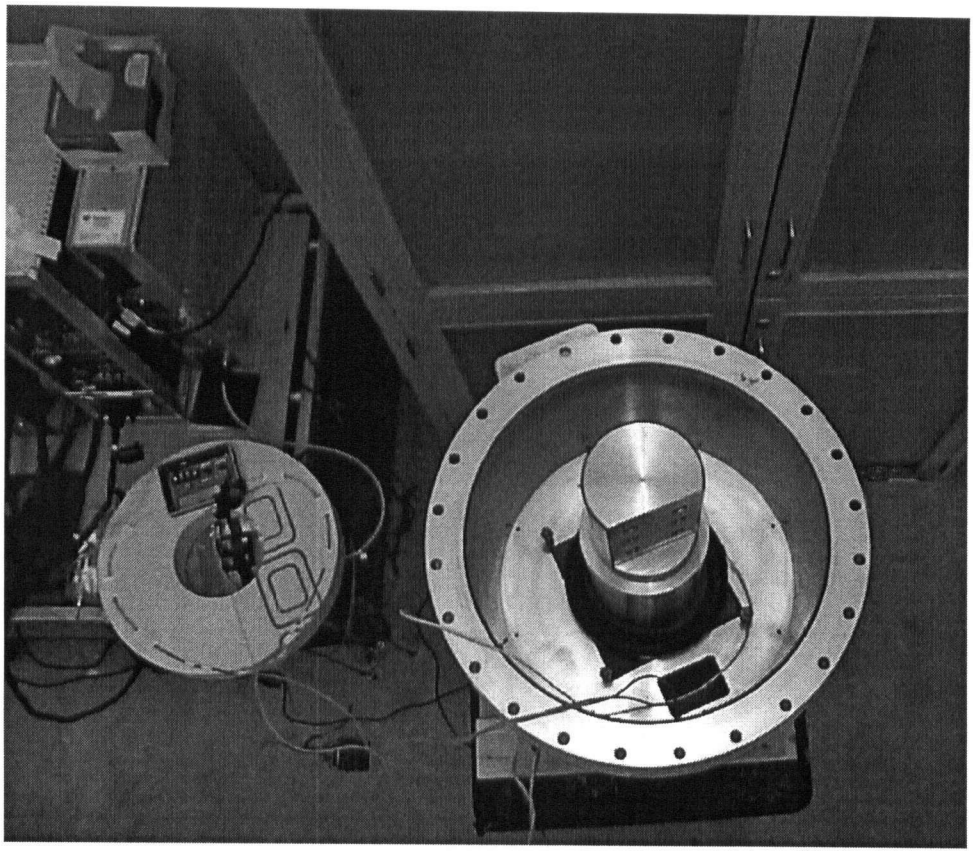

Figure 4.5: The second generation IOCT housing is seen here from above with the cover removed. The Rogowski coil is seen at the base of the busbar. The IOPC and integrator are seen at the left, embedded in a foam ring.

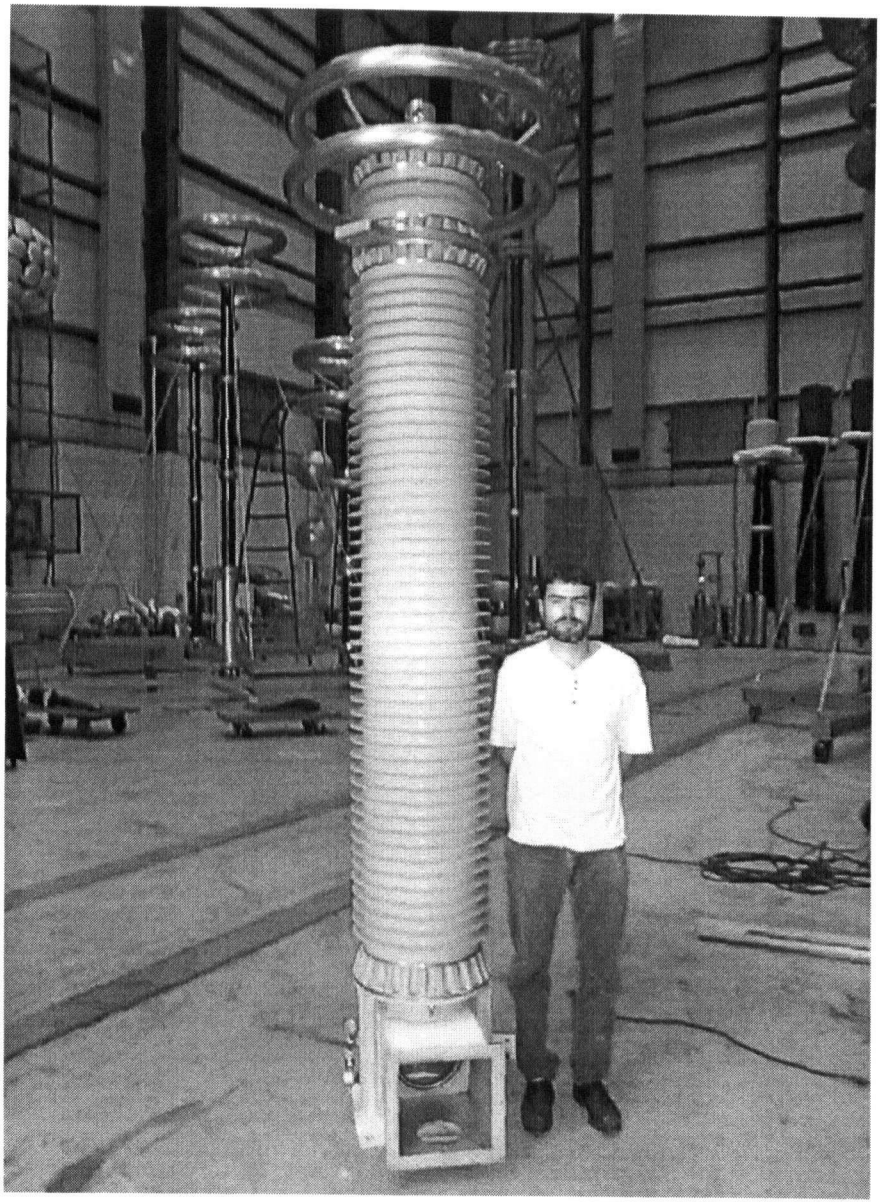

Figure 4.6: The second generation IOCT mounted on a 230 kV post insulator.

Chapter 5

Test Results

5.1 Introduction

This chapter presents the experimental results for the IOCT. The IOCT performance was measured to determine its linearity, transient response, frequency response, and temperature stability. Measurements were made using multiple setups to cover the wide dynamic range of the IOCT. The results are presented here in the context of IEC and IEEE standards for both metering and protection applications.

The first generation IOCT was tested for linearity at the High Current Laboratory at Powertech Labs Inc. (PLI), Surrey, BC. The linearity was found to be within ± 0.2 % from 200 A to 10 kA with a phase stability within ± 1.5 minutes of arc [16]. The primary limitation of this sensor was that the output was proportional to the derivative of the current. A far more rigorous test procedure was executed on the second generation IOCT, the results for which are presented below.

5.2 Test Setup

To accommodate the wide dynamic range of the IOCT, two different test configurations were required to supply current. A current source for supplying 10 A to 1.5 kA was constructed at UBC using a 100 turn coil of 12 gauge copper, two 208:60 step-down transformers (series primaries, parallel secondaries), and a variac. The coil turns were passed through the window in the IOCT's Rogowski coil to multiply the current. A reference signal was obtained from a precision low inductance, 75 W, 10 mΩ coaxial shunt resistor from T&M Research Products, Albuquerque, NM. A photograph of this current source is shown in Figure 5.1. This setup was used for low-current linearity measurements as well as thermal cycling. The IOCT, with the external housing removed for testing convenience, is shown inside the temperature chamber at UBC in Figure 5.2.

To reach higher current levels, the IOCT was tested at the High Current Laboratory at PLI. The current source available there consisted of a 600 V, 100 kVA variac used to drive three 50 kVA step-down transformers wired in parallel (see Figure 5.3). This setup could source continuous current at approximately 4 kA, and generate short duration currents of approximately 30 kA. The IOCT was connected to the transformers with one solid copper busbar, and two flexible braided copper cables as shown in Figure 5.4.

Several different current references were used to obtain an independent current measurement to which the IOCT could be compared. A Rogowski coil with an active integrator, as well as three 5000:5 A CTs (one for each step-down transformer) used with resistive shunts, were tested separately. The most reliable reference proved to

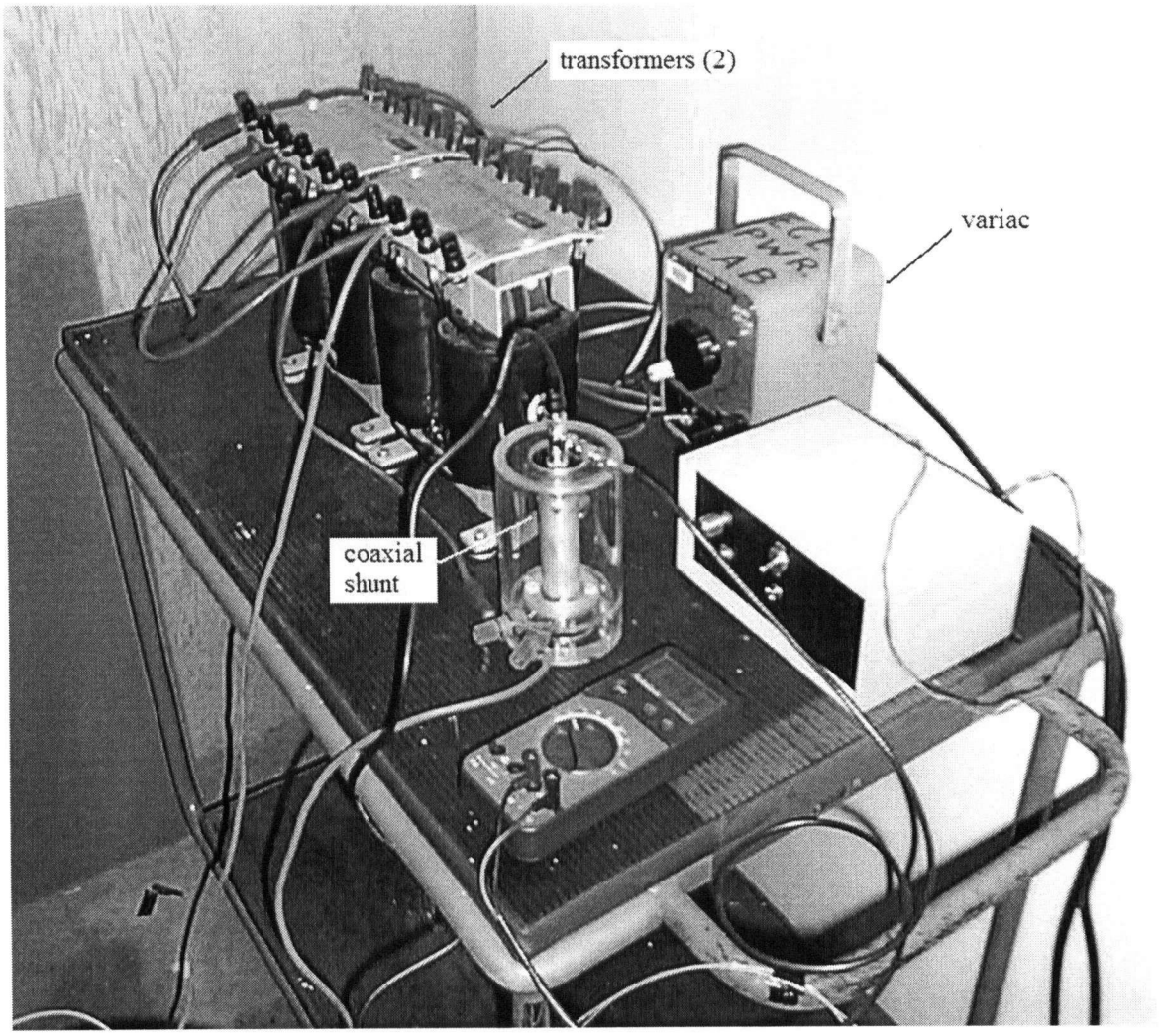

Figure 5.1: The low-current source at UBC.

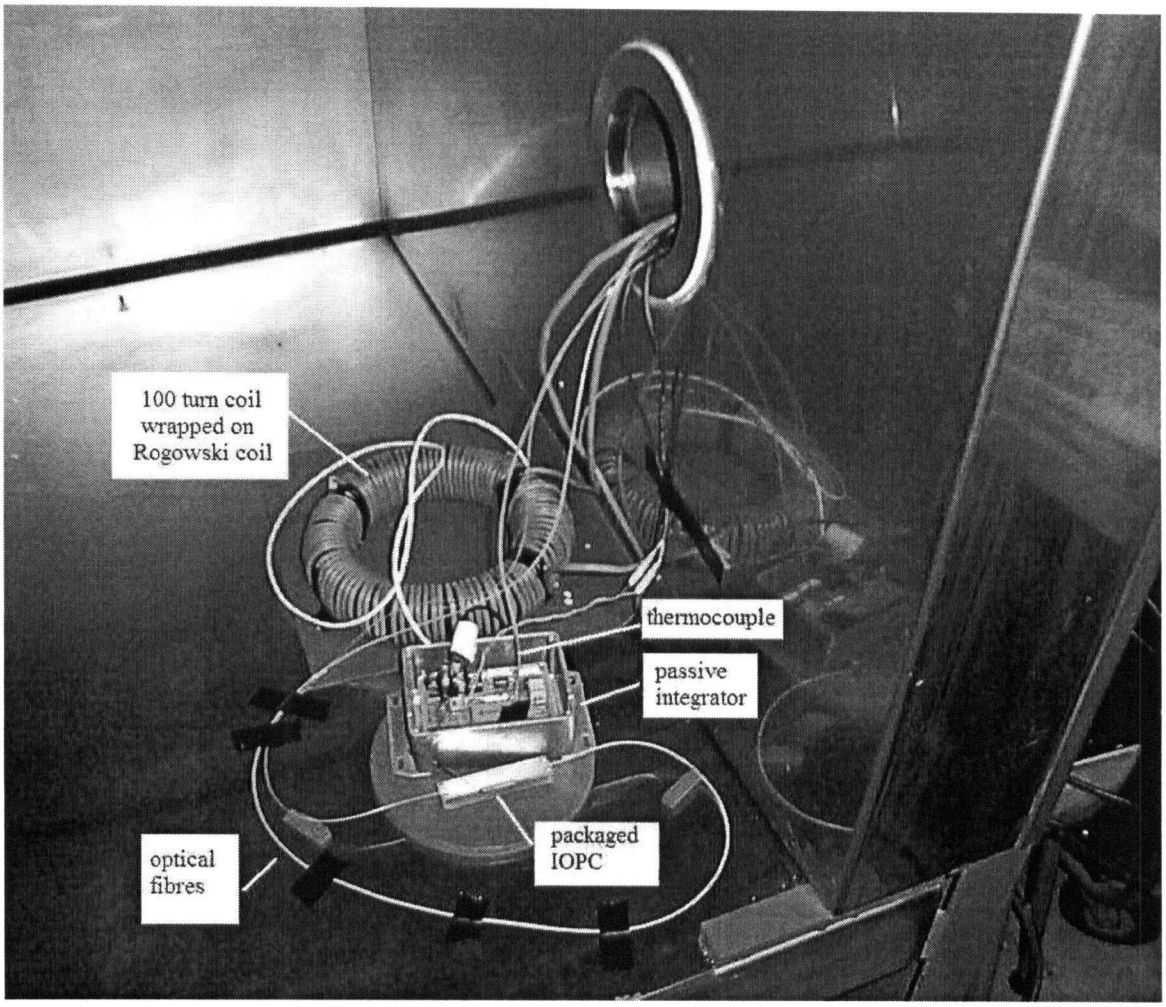

Figure 5.2: IOPC with Rogowski coil inside the temperature chamber at UBC.

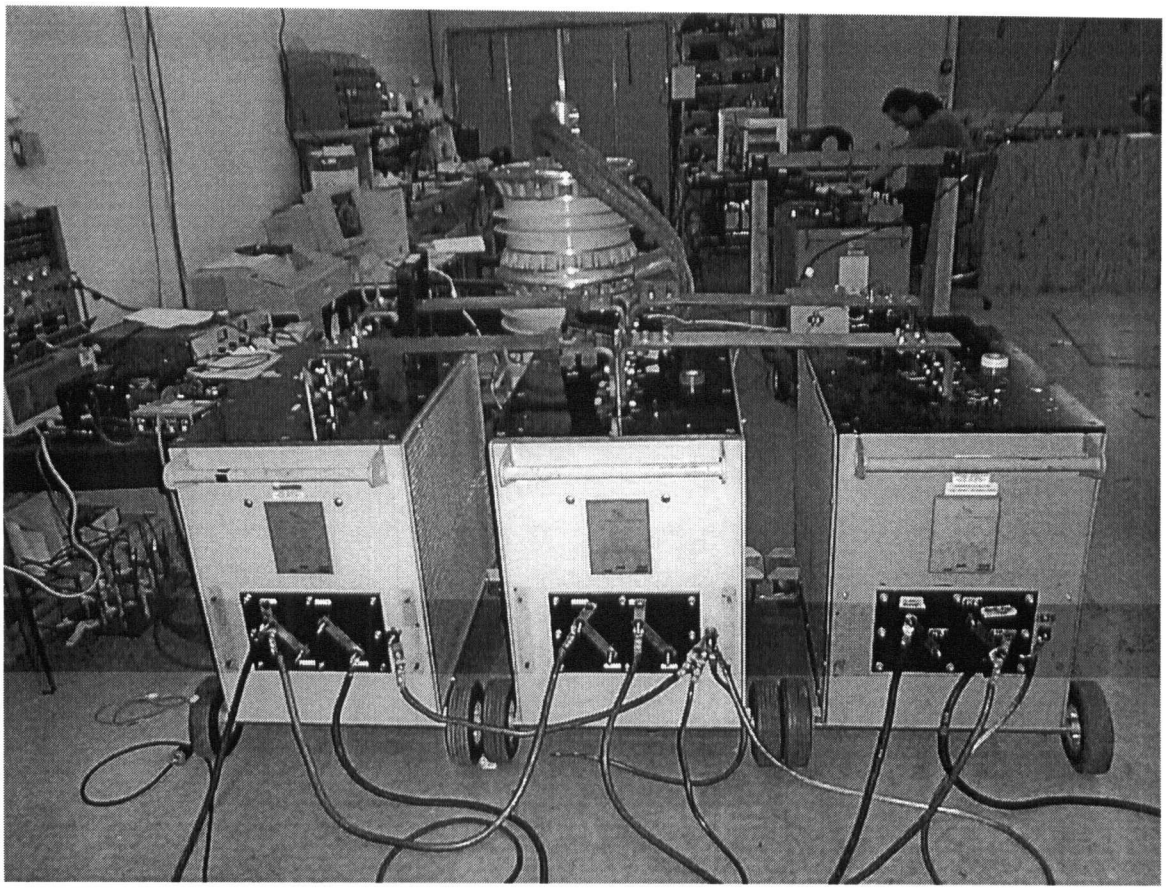

Figure 5.3: Three parallel 50 kVA step-down transformers at PLI's High Current Laboratory.

be the Rogowski coil which as expected showed no signs of saturation. On the other hand, the CTs did saturate, even at currents below rated, if the high current cables passed in close proximity to a CT core. Saturation was identified by viewing the waveform distortion on an oscilloscope.

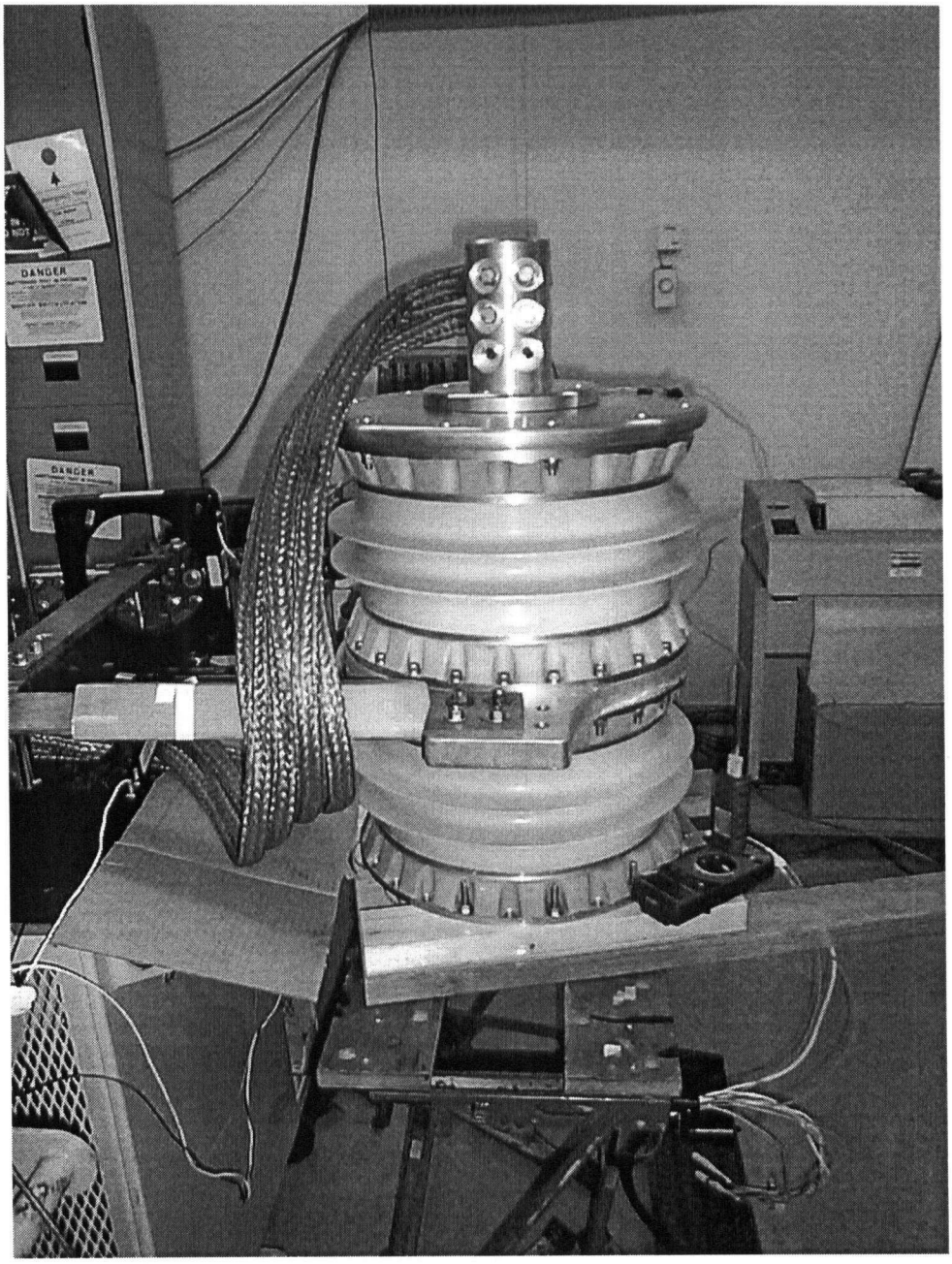

Figure 5.4: IOCT (without insulator column) at PLI's High Current Laboratory.

5.3 Linearity

The current values selected for linearity measurements were those corresponding to standard IEC [20] and IEEE [18] values for a 3 kA nominal current. Calculations of ratio and phase were performed on the digital output of the IOCT relative to the reference signal. The reference signal was sampled with a 16-bit analog-to-digital converter, provided by Nxtphase Corporation. At currents up to 10 kA, data samples spanning at least 200 power frequency cycles were collected from which the ratio and phase were calculated. At currents above 10 kA, thermal limitations of the current source required shorter tests, reaching approximately 20 power frequency cycles at 30 kA. These shorter data records were analyzed in Matlab^{TM} by trimming the data to an integral number of cycles, and using the discrete Fourier transform to obtain the ratio and phase.

The low-current setup was used from 30 A to 1.5 kA, while the high current setup was used from 1.5 kA to 20 kA. To combine the two data sets, the ratio and phase errors of the low-current data were level shifted to agree with the high current setup's error at 1.5 kA. The calibration point for zero ratio and phase error was obtained by measuring a 3 kA current at the beginning of the high current tests. All data were then corrected using the scale factor and phase displacement obtained at 3 kA.

Figures 5.5 and 5.6 show the measured ratio and phase for the IOCT along with the error limits in IEC 0.2S, IEC 0.2 [19], and the IEEE 0.3 % classes [18]. The IOCT satisfied these three accuracy classes, demonstrating excellent performance for metering applications. In fact, the IOCT is seen to significantly exceed the linearity

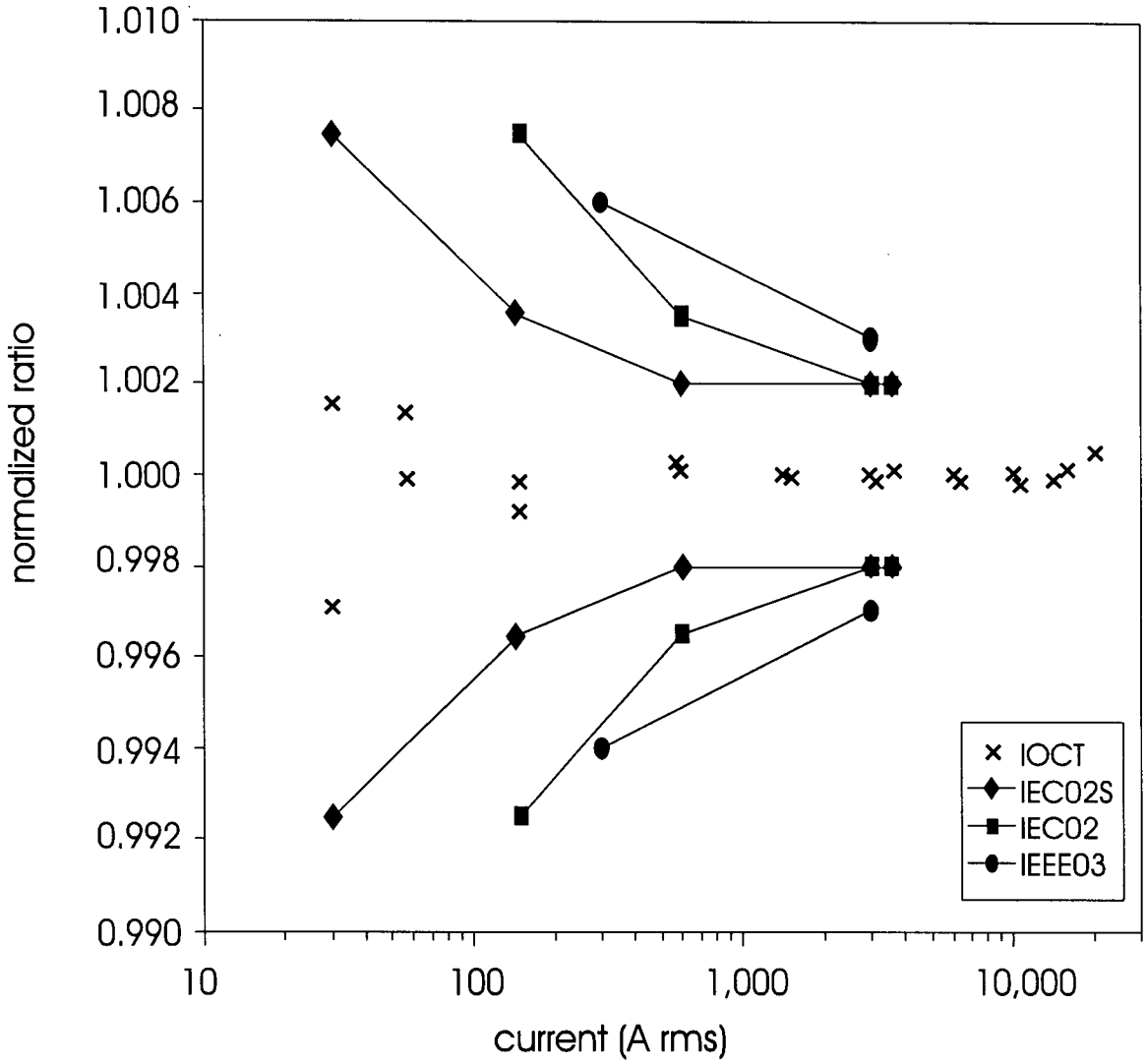

Figure 5.5: Normalized ratio vs. current for the IOCT with IEC and IEEE error classes.

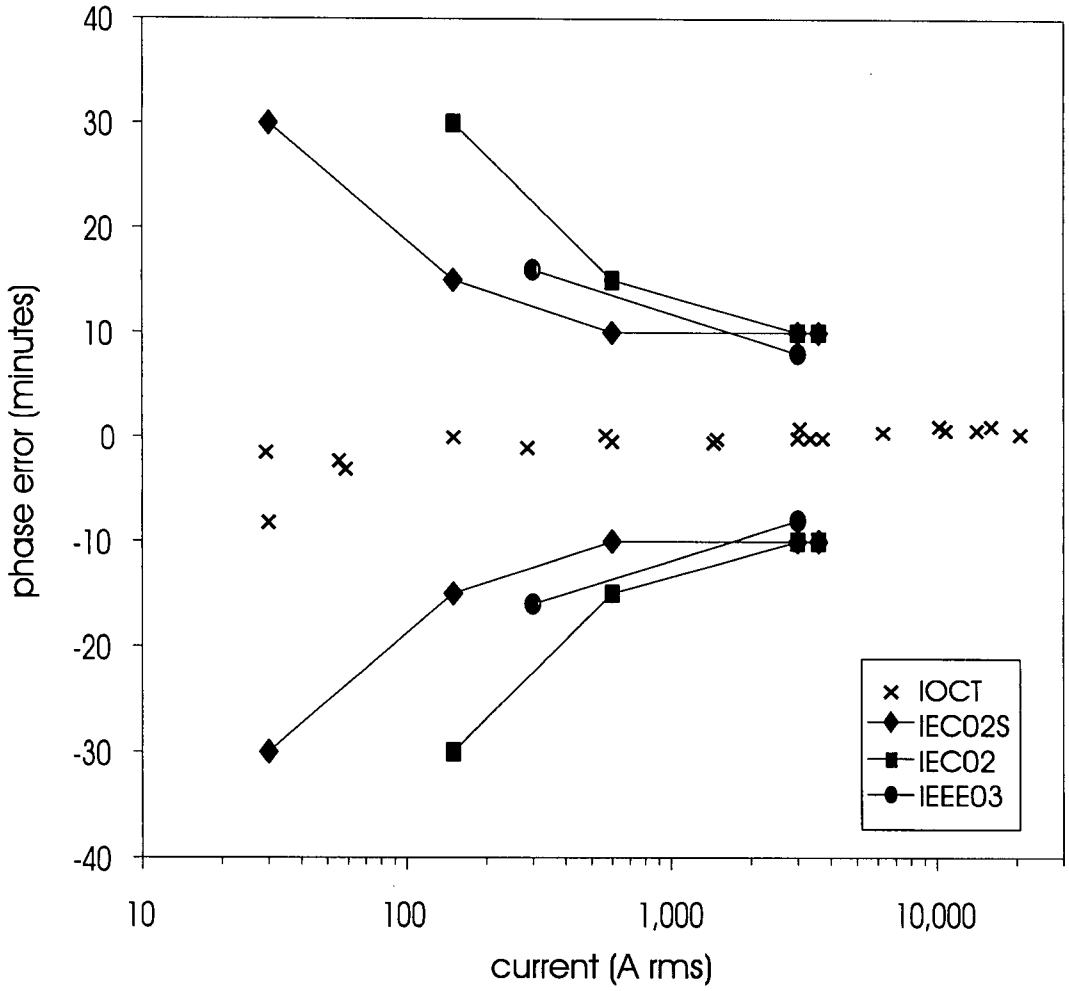

Figure 5.6: Phase error vs. current for the IOCT with IEC and IEEE error classes.

requirements past the 3.6 kA level (120 % nominal) by obtaining better than 0.2 % linearity up to 20 kA.

Although the linearity of the IOCT at 60 Hz exceeded the linearity objectives, initial tests found the IOCT to be susceptible to 120 Hz vibration. If sufficient vibration reaches the IOPC, an optical modulation results which is then falsely detected as a current signal. Table 5.1 shows the 120 Hz harmonic error current relative to the fundamental for various currents. Each data point is calculated from 87 power frequency cycles and represents the detected current over a 0.7 Hz bandwidth. For comparison, the noise floor in the vicinity of 120 Hz is approximately -91 dB over a 0.7 Hz bandwidth. The detected error current shown in Table 5.1 is well above the noise floor. Furthermore, since the vibration noise is correlated with the current, it can lead to errors if harmonics are metered.

To improve the immunity of the IOCT to vibration, a damping system was fitted to the IOCT housing (see Chapter 4). A second series of tests were performed at PLI to verify the effect of the damping system. The results show a $\sim$20 dB improvement in the 120 Hz error, bringing it close to the background noise (see Table 5.1). While these results are not conclusive that the IOCT will be immune to all vibration levels encountered in a substation (an accelerometer was not available at the time of the test), they do show that the potential exists for further noise reduction through more sophisticated damping schemes if required.

Table 5.1: Comparison of the 120 Hz error currents with and without vibration damping.

Current (A rms)	120 Hz Error Current Without Damping (dB)	120 Hz Error Current With Damping (dB)
3000	−55	−80
3600	−53	−75
6000	−54	−88

5.4 Transient Tests

Transient current measurements were performed at PLI to evaluate the ability of the IOCT to measure instantaneous current at levels up to 30 kA. In order to avoid errors associated with the finite lower cut-off frequency of the IOCT, as well as the reference, an active integrator was constructed for the reference Rogowski coil having the same lower cut-off frequency as the IOCT (0.6 Hz).

Initial tests revealed high-frequency distortion on the IOCT signal during the first few power frequency cycles after energizing and breaking the circuit. Figure 5.7 shows a typical waveform captured while energizing to a current of 30 kA. Such distortion was found to occur for currents over 6 kA, with the severity of the distortion increasing for higher currents. It was found that the cause of the distortion was mechanical in origin and could be virtually eliminated by the vibration damping system described above. Figure 5.8 shows the waveform of a 30 kA signal measured with the vibration damping in place. The high-frequency distortion observed previously no longer occurred at any of the current levels tested (150 A to 30 kA). Figure 5.9 shows the full open-close-open cycle for data in Figure 5.8.

After addressing the vibration problem, the IOCT showed excellent transient performance up to the current source limit of 30 kA. The rms error was found to be

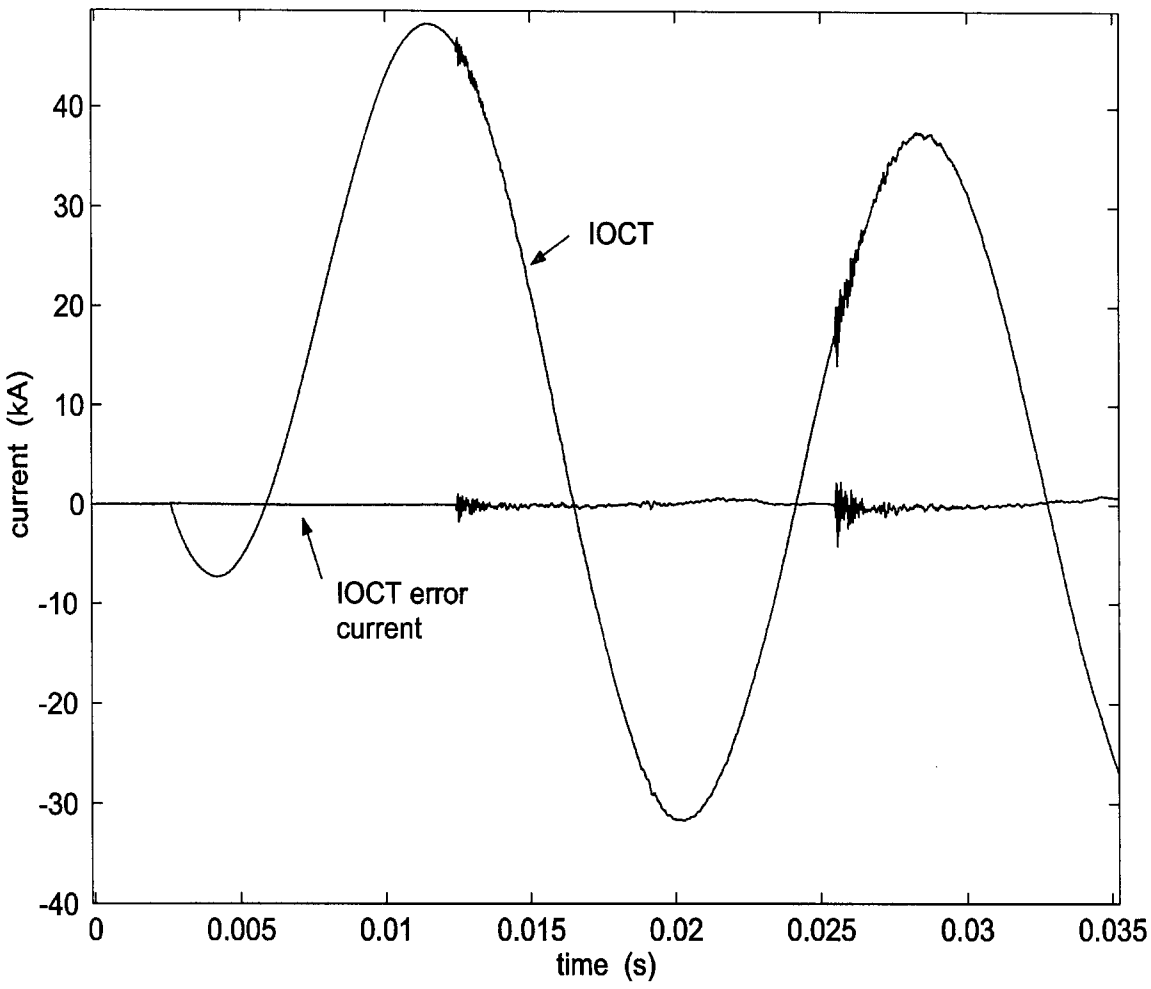

Figure 5.7: 30 kA current waveform measured with the IOCT with vibration induced noise. Error current is also plotted.

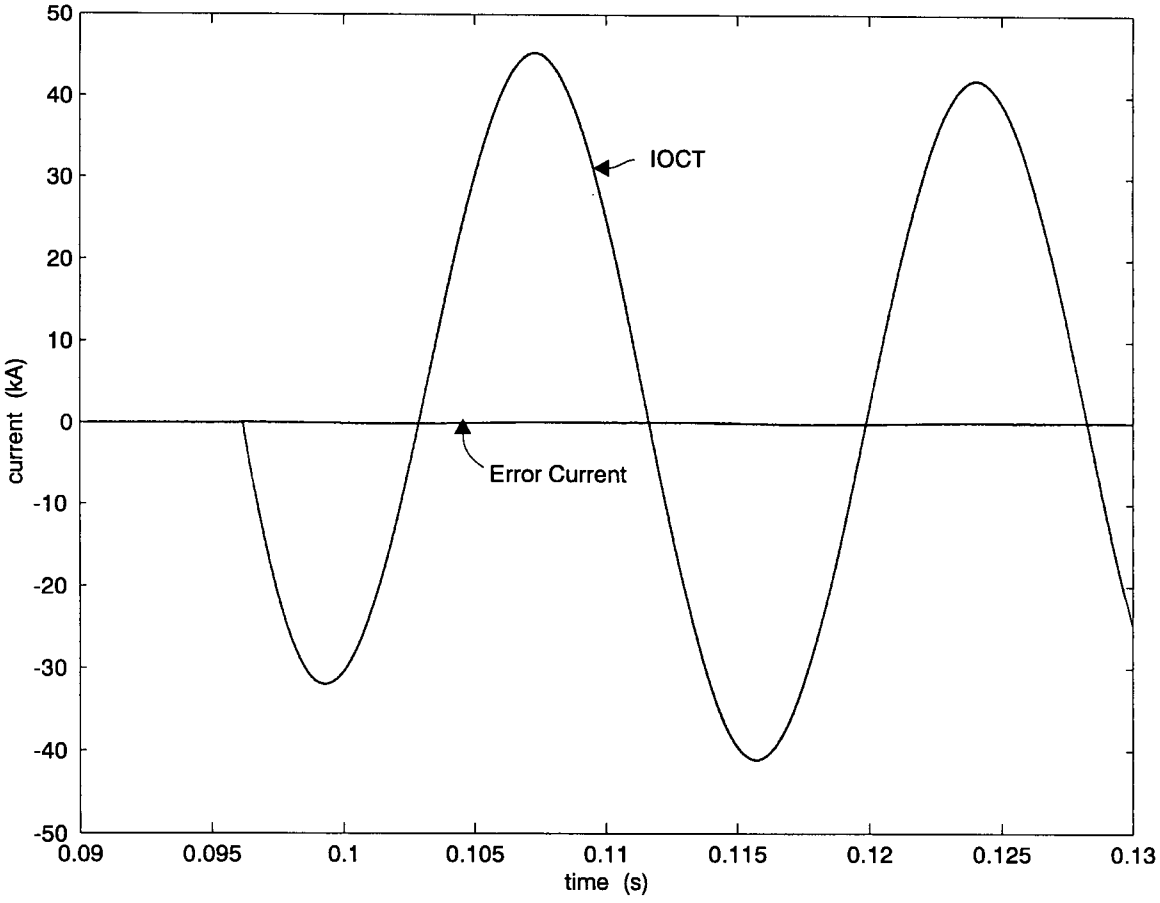

Figure 5.8: 30 kA current waveform measured with the IOCT after fitting a vibration damping system to the IOPC. The vibration induced noise is no longer visible.

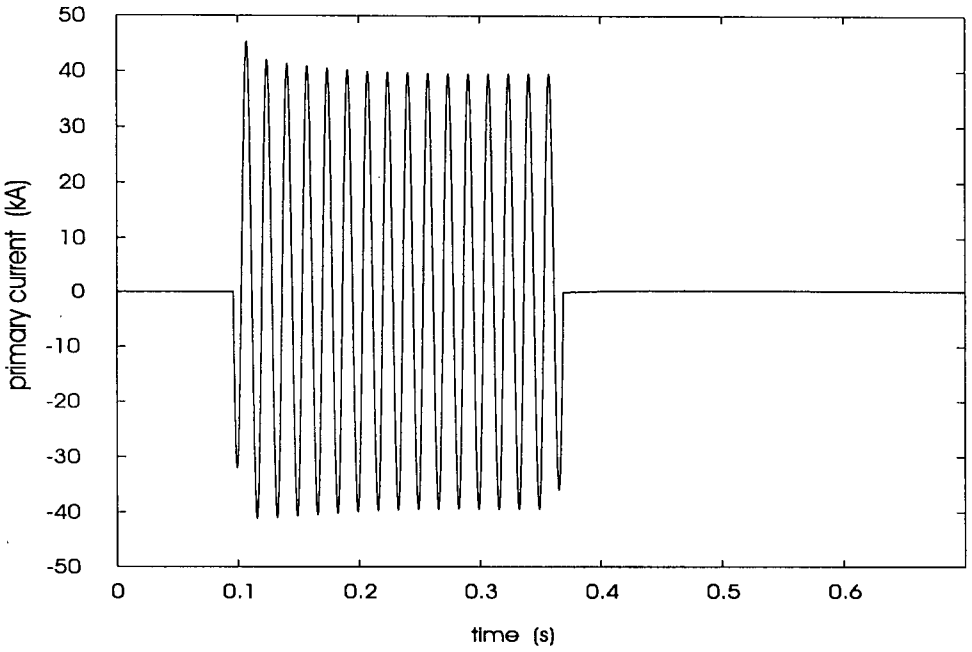

Figure 5.9: 30 kA current waveform measured with the IOCT after fitting a vibration damping system to the IOPC. The full open-close-open cycle for data in Figure 5.8 is shown.

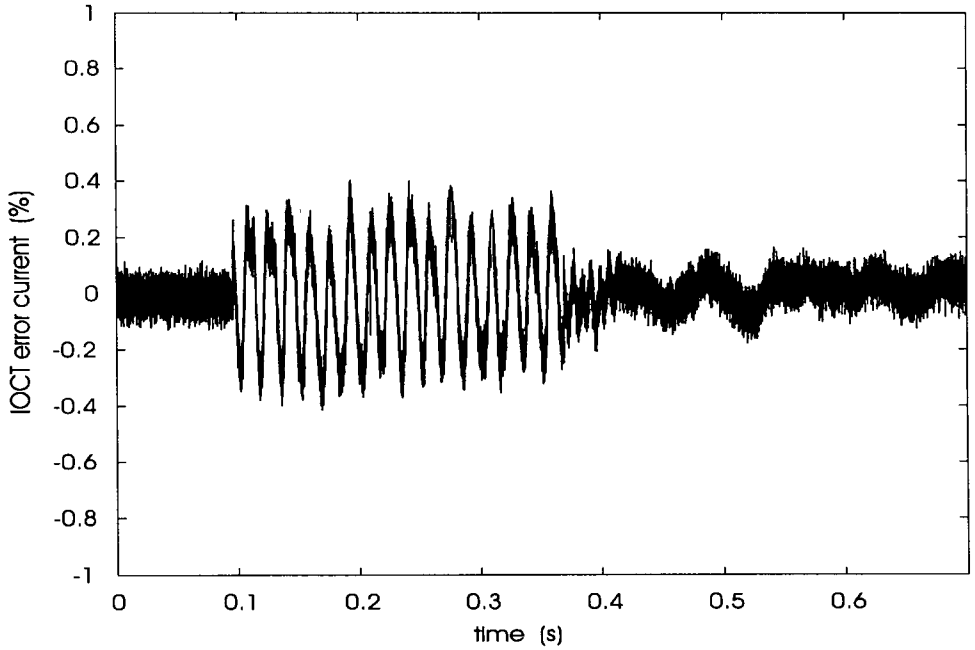

Figure 5.10: Error current in percent for the 30 kA waveform shown in Figure 5.9.

less than 0.2 % (calculated over 10 cycles) and the instantaneous error over the full open-close-open cycle was better than 0.5 % as seen in Figure 5.10. The estimated error for the IOCT is predicted to be below 1 % up to 60 kA. This estimation is based on the deviation of the measured optical transfer function, for this particular IOPC, from the ideal case of Equation 3.1. The subject of transfer function distortion is analyzed in detail in Chapter 6.

Comparison of the IOCT's instantaneous error with existing standards is of limited significance because existing standards are based on the saturation behavior of conventional current transformers (CTs). Because of the propensity of conventional CTs to core saturation, instantaneous error is conventionally measured on transients having a slowly decaying exponential current (see for example IEC 60044-1 [19]). This slowly varying component will cause measurement error due to the low-frequency cut-off of inductive type sensors. Furthermore, for the conventional CT, the slowly varying current will disproportionately increase the flux in the core and can cause saturation errors. This non-linear frequency dependent behavior means that small-signal bandwidth measurements are of little use for predicting measurement errors in the conventional CT. The IOCT in contrast is well characterized by its small-signal bandwidth due to the absence of a magnetic core. The frequency response of the IOCT is presented next.

5.5 Frequency Response

While existing standards for CTs do not cover frequency response, the draft standard IEC 60044-8 [20] does recommend specifications for both protection and metering

applications. The frequency response of the IOCT was measured at UBC using a pulsed current source and a 100 turn coil capable of providing an effective current of 3 kA. The current source consisted of a MOSFET circuit (two IRLIZ44N from International Rectifier, El Segundo, CA, in push-pull configuration) driven by a function generator and a DC power supply. This setup could be operated up to 2.5 kHz, and when combined with harmonic analysis, was effective for measuring the IOCT response up to 10 kHz. The function generator was operated in pulse mode with a 10 % duty cycle to increase harmonic content. Matlab^{TM} was used to analyze the data.

The measured magnitude response is shown in Figure 5.11. Data were collected at 5 different pulse frequencies: 15, 57.6, 300, 1000, and 2500 Hz. For each pulse frequency, the first four harmonics were calculated for the IOCT and reference signals. This produced five data series (pulse frequencies), with four data points each. Also shown in Figure 5.11 are the ratio error limits contained in [20] for three classes: power metering, quality metering, and protection. The IOCT is shown to perform within the error limits for all three classes simultaneously.

Figure 5.12 shows the measured phase error for the IOCT including the allowable error limits in [20]. A time delay of 23 μs was removed from the phase response before plotting to account for the latency of the IOCT (due in large part to the DSP unit). The corrected data are within the allowable error limits for all three classes.

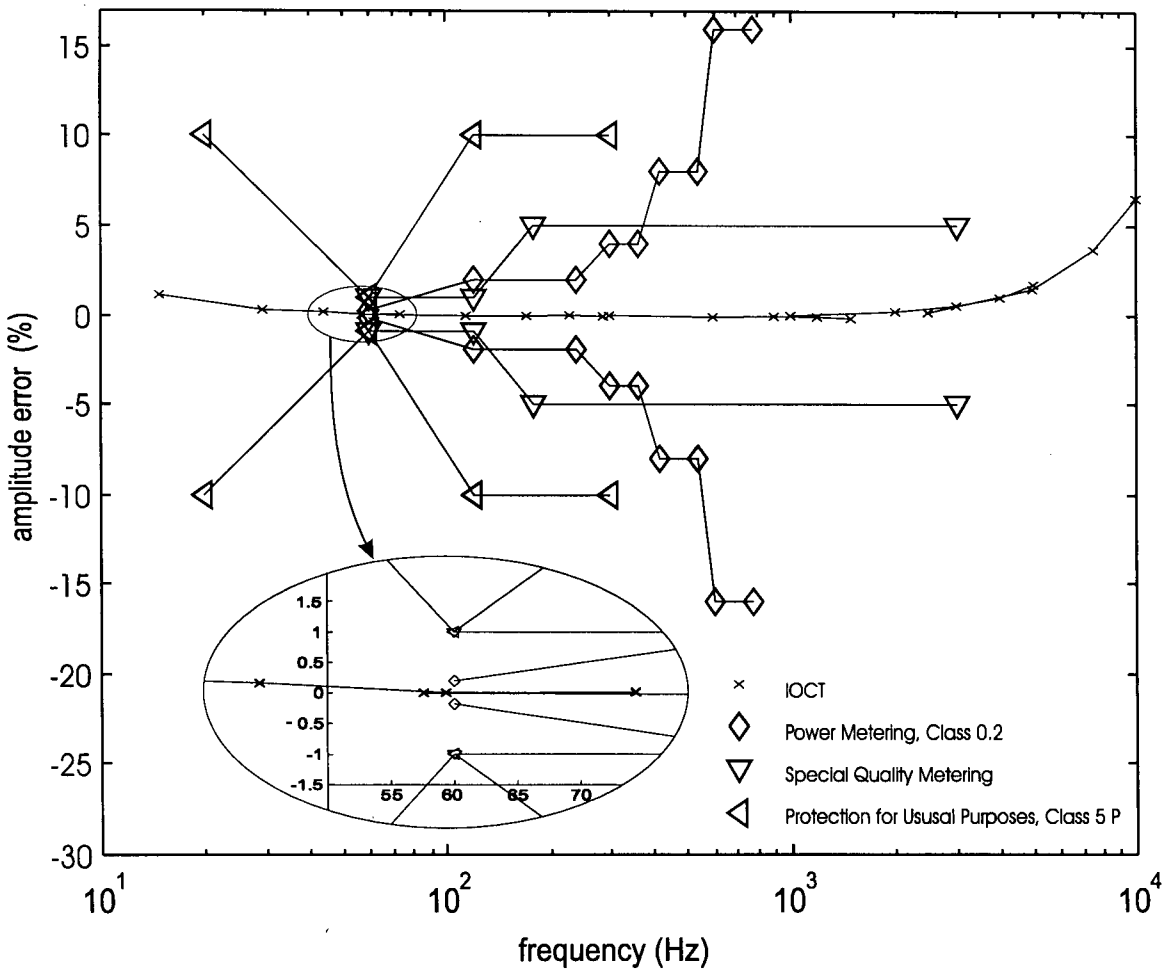

Figure 5.11: Amplitude response of the IOCT with error limits as proposed in the IEC 60044-8 draft standard.

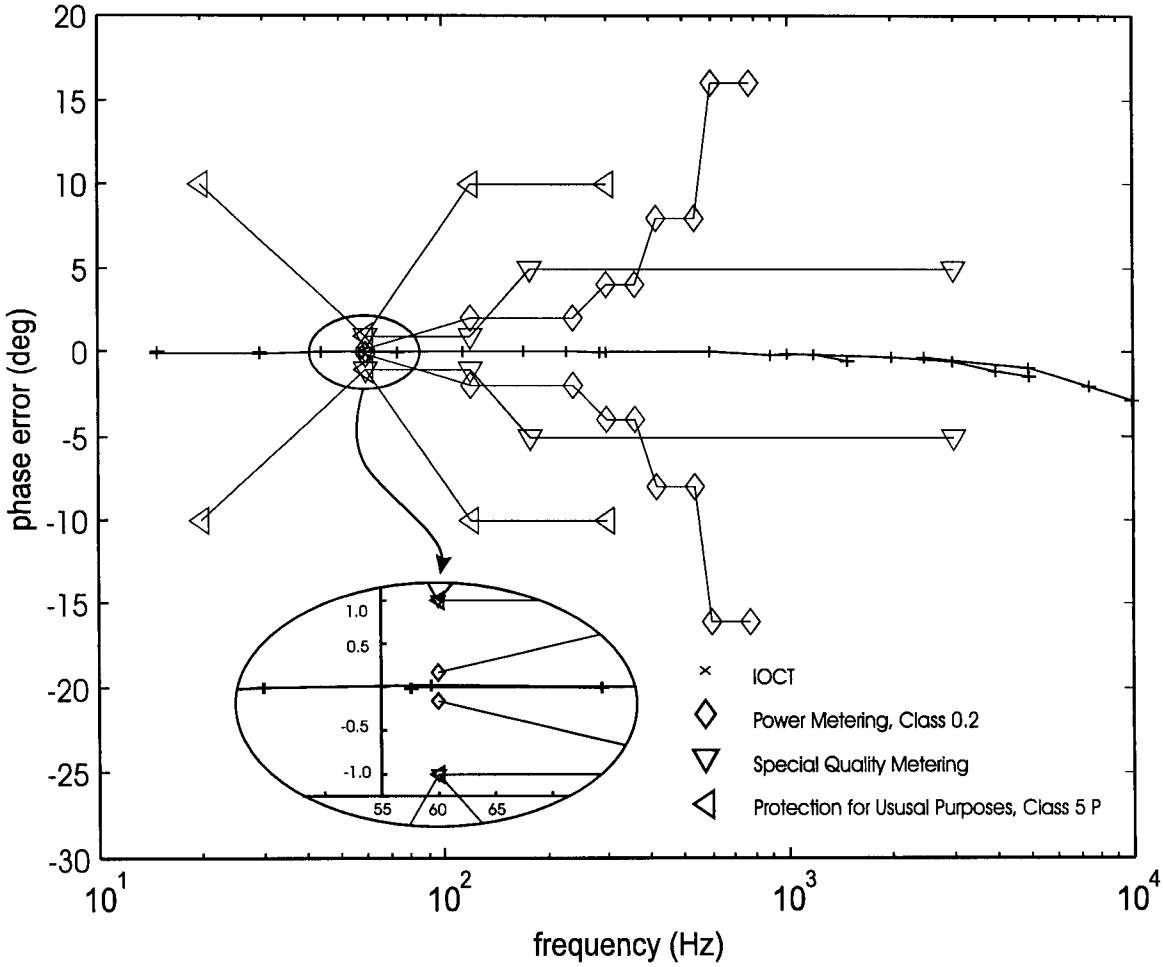

Figure 5.12: Phase response of the IOCT with error limits as proposed in the IEC 60044-8 draft standard.

5.6 Proximity Test

The IOCT was evaluated for its ability to reject currents that pass in close proximity, but not through the Rogowski coil. A nearby current could potentially be detected due to non-idealities in the Rogowski coil winding uniformity, inductive coupling to the integrator, as well as Faraday rotation in the optical path. The measurements were performed by placing a 1.5 m diameter current loop, passing 3 kA, in three different positions with respect to the IOCT. An axial magnetic field was obtained by surrounding the IOCT housing with the current loop, and two orthogonal horizontally directed magnetic fields were obtained by holding the loop approximately 200 mm from the IOCT housing.

Table 5.2 shows the currents measured for each magnetic field orientation, including the noise floor in the absence of current. Each data point represents an average of three measurements taken over 200 power frequency cycles, filtered to a 10 Hz bandwidth. The IOCT in each orientation detected less than 0.05 % of the 3 kA current. Although this was not a standard test, the results indicate that the IOCT will not suffer from cross-talk in a substation environment where the conductors are spaced considerably farther apart than the 200 mm used here.

Table 5.2: Proximity test results.

Axis	Current (10 Hz bandwidth)
axial	0.048 %
ortho 1	0.037 %
ortho 2	0.023 %
noise floor	0.02 %

5.7 Temperature Response

For metering applications, a current sensor must maintain its accuracy across its operating temperature range. The objective here was to meet 0.3 % accuracy and preferably also meet 0.2 % accuracy. Tests were first conducted on the Rogowski coil and integrator to evaluate the various contributions to the IOCT temperature response. Subsequently, the full IOCT was tested with a multi-turn primary coil to give an effective current of 3 kA. Determining the temperature response of the IOCT was a two-step process. The IOCT was temperature cycled initially to determine its magnitude response in relation to the optical bias point of the IOPC. This initial measurement was used to create a compensation curve based on optical bias that could be calculated in real-time. The IOCT was then temperature cycled again to determine the accuracy of the compensated measurements.

5.7.1 Thermal Response of Subcomponents

The Rogowski coil's temperature response was minimal, varying by 25 ppm/°C over the range from -40°C to $+60$°C. This measurement was performed with the load resistor and integrator attached in order to load the Rogowski coil. The integrator produced a larger variation at 70 ppm/°C for a total variation of 95 ppm/°C for the Rogowski coil, load resistor, and integrator combination. Although this temperature coefficient results in a total variation of ± 0.5 %, the variation is predictable and can be compensated for if the temperature is known. The IOPC's optical bias point provides the required temperature information [13].

The IOPC is the dominant source of temperature variation in the IOCT. The

challenge is in obtaining a one-to-one relationship between the optical bias point and the temperature. If such a relationship can be maintained, the bias point of the IOPC can be used as an input to a lookup table to determine the ratio correction factor for any temperature. The first problem that was encountered in temperature cycling the IOPC was a hysteresis loop in the bias as a function of temperature. This problem was correlated with rapid temperature change, particularly in the 30 to 60°C range, coinciding with the glass transition temperature of the UV adhesive initially used to bond the optical fibers to the lithium niobate substrate. The degree of hysteresis was found to decrease to acceptable levels by switching to a glue with a higher glass transition temperature and mounting the IOPC substrate in a low stress manner (see Section 4.2.3).

The second problem encountered in trying to obtain a one-to-one bias to temperature relationship was the appearance of spontaneous bias changes. Particularly at lower temperatures, rapid (less than 15 μs) jumps in the IOPC's bias point on the order of 0.02 radians occurred during temperature cycling. This situation is problematic because a jump in bias appears as a step change in the current, i.e., a sudden application of DC current, and can appear to be on the order of several kA. This poses obvious problems for relaying applications, but also can cause metering errors since the bias point is used to compensate for temperature induced ratio variations.

The bias jumping phenomenon is believed to be associated with pyroelectric discharges. Instability in the half-wave voltage and bias of a lithium niobate voltage sensor during temperature cycling has been reported [52]. The instability was attributed to the pyroelectric effect, although details on a sub-second time scale were

not given. In [52], an ITO (indium tin oxide) coating on the end-facets of the lithium niobate substrate was shown to improve temperature stability. As discussed in Section 4.2, a Y_2O_3 coating was used in this work to dissipate pyroelectric charges. An order of magnitude reduction in bias jumps was seen when using the Y_2O_3 coating although isolated jumps were still found to occur approximately once per temperature cycle. Figure 5.13 shows the measured bias and temperature over time of a Y_2O_3 coated IOPC. A single bias jump was recorded near the temperature minimum. The impact of the bias jump is seen in Figure 5.14 which shows the bias corrected ratio as a function of time for the -40 to $+60$°C cycle. The correction was done by fitting a 7^{th} order polynomial to the trace in Figure 5.15, corresponding to $\alpha = 0.93$ (α is used in linearizing the IOPC transfer function, see Equation 3.1). The corrected ratio is seen to be very stable with the exception of the bias jump event where the ratio reaches -0.5 % error.

Figure 5.15 shows the measured normalized ratio of the Y_2O_3 coated IOPC as a function of the optical bias. Five traces are shown corresponding to different values of α. The measured value for α was 0.93 although it is apparent that a slightly smaller value gives a flatter response. The effect of the bias jump from Figure 5.13 shows up in Figure 5.15 as a hysteresis loop near the negative extreme value of the bias. The loop breaks the monotonic relationship between bias and ratio, resulting in an uncorrectable error as shown in Figure 5.14.

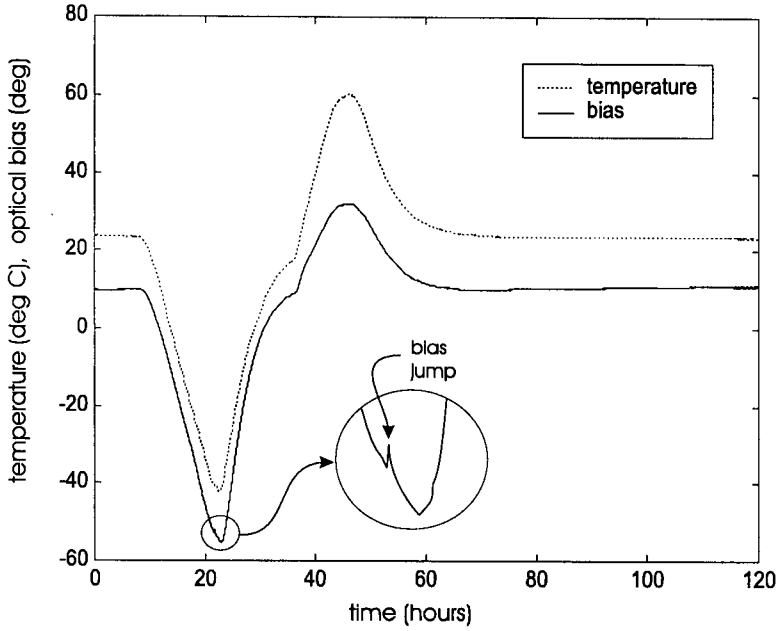

Figure 5.13: Optical bias and temperature as a function of time over a -40 to $+60°C$ cycle.

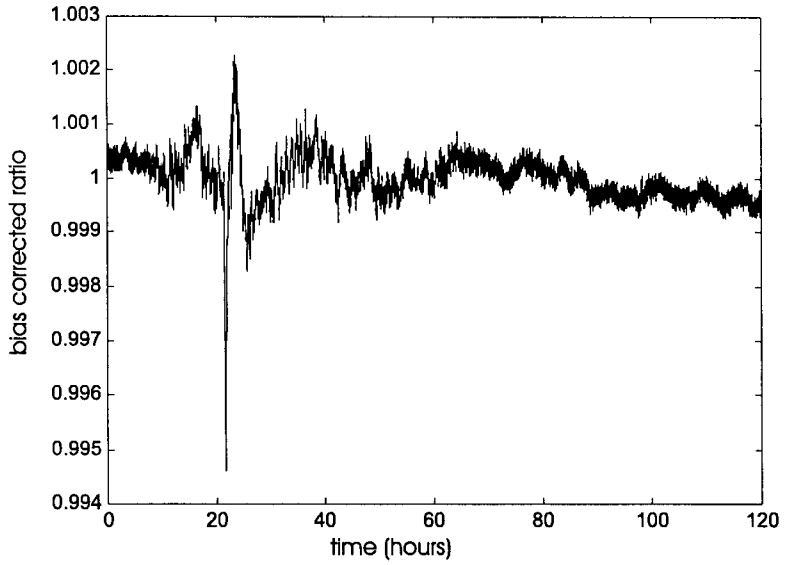

Figure 5.14: IOPC ratio as a function of time for the -40 to $+60°C$ cycle, corrected using a polynomial fit to the ratio vs. bias characteristic.

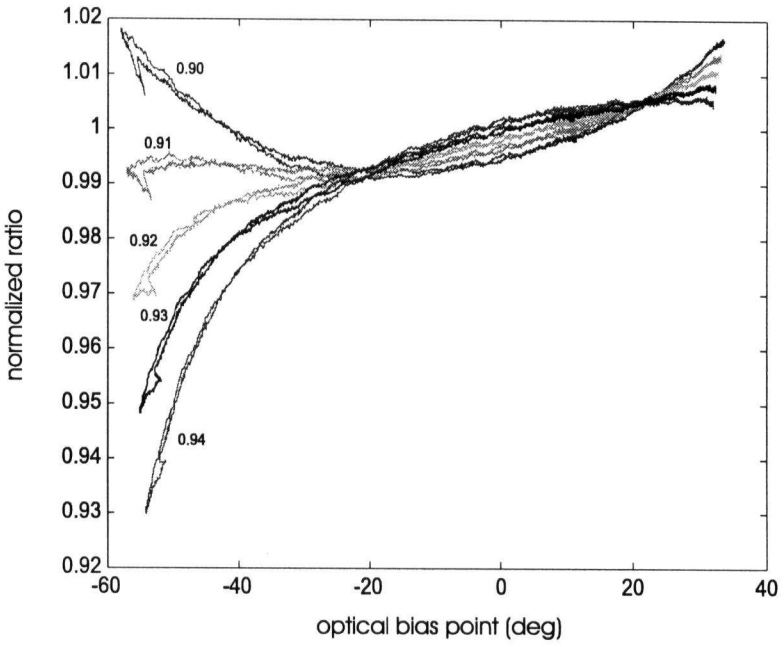

Figure 5.15: Normalized ratio for an IOPC as a function of optical bias point for the −40 to +60°C cycle. Multiple traces result from different values of α used in linearizing the IOPC transfer function.

5.7.2 Thermal Response of the IOCT

Having optimized and characterized the component parts of the IOCT, the Rogowski coil, load resistor, passive integrator, and IOPC were temperature cycled together to determine the response of the complete IOCT. Figure 5.16 shows the measured ratio as a function of temperature over a −30 to +70°C range after correction as a function of bias has been applied from an independent calibration run. A ramp rate of 10°C/hr was used. The error is primarily due to bias instability at low temperatures. The maximum ratio error was 0.29 %, and the minimum was −0.30 %. This result shows that 0.3 % metering accuracy is possible with the IOCT.

The phase accuracy of the IOCT must also be maintained over the operating temperature range. Two main factors contribute to phase variations: 1) the inte-

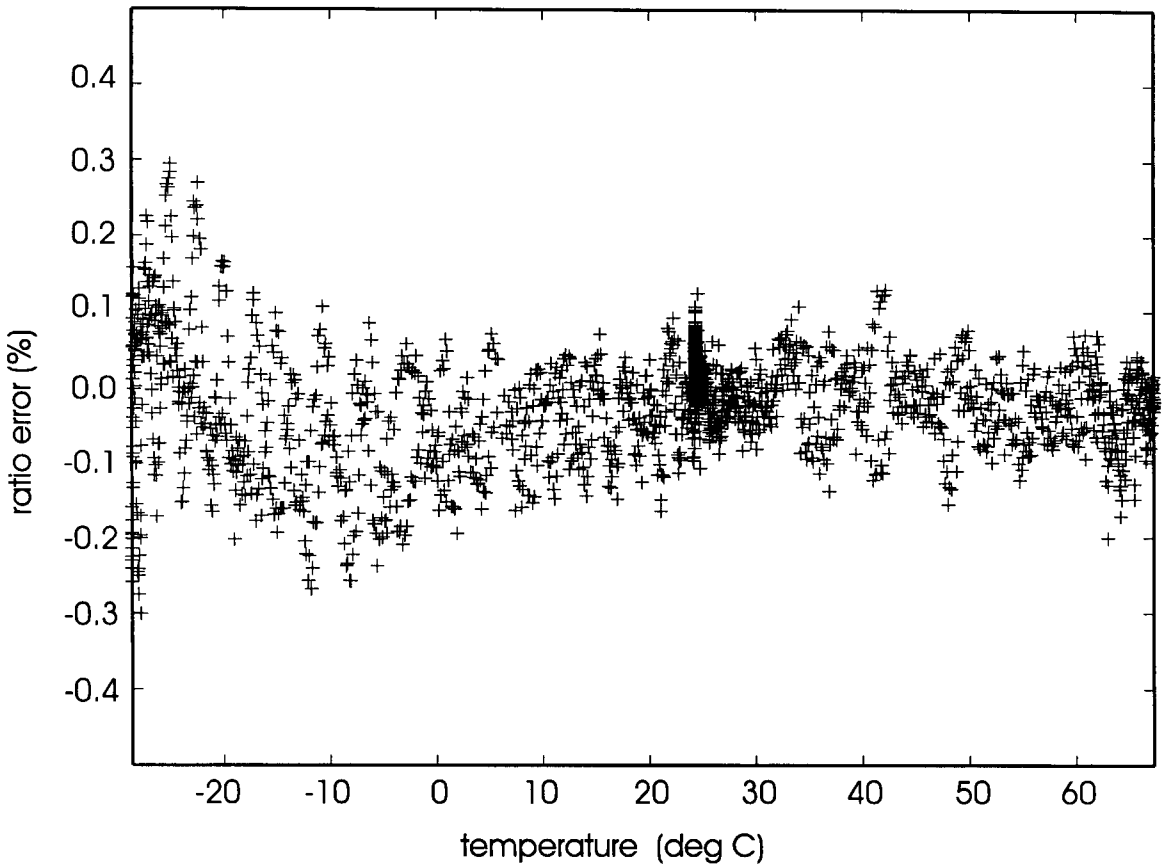

Figure 5.16: Ratio of the IOCT over the temperature range -30 to $+70$°C. Calibration data for this plot were obtained from a previous temperature cycle to test repeatability.

grator's phase varies due to variations in the resistor and capacitor values, and 2) the IOPC contributes a phase delay due to the slow time constants discussed in Section 3.3.2 which are expected to be temperature sensitive. The phase variation from the integrator was measured to be very small, approximately ± 0.7 minutes over a 100°C span. The phase response of the complete IOCT is shown in Figure 5.17. The response shows a decrease in phase at higher temperatures. (This has been characteristic of phase vs. temperature measurements of other IOPCs fabricated during the course of this work.) The variation is well below the allowable error limits of ± 8 minutes for the IEEE 0.3 % metering class and ± 10 minutes for the IEC 0.2 % class.

The total bias variation for the IOPC over the temperature range will ultimately be the limiting factor for the maximum measurable current. For the IOPC used here, the bias varied from -53 to $+40°$ from the quadrature point over the temperature range of -30 to $+70$°C, leaving an absolute maximum electro-optic modulation of $\pm 37°$. The targeted maximum over-current factor was 20, or 60 kA for a maximum measurable current. This amounts to an electro-optic modulation level of $\pm 17°$ which is still less than the maximum allowable level. The predicted ratio error at 60 kA, due to residual non-linearity in the linearized IOPC transfer function, is less than 1 % for a temperature of -30°C. Thus the IOCT is expected to maintain a composite error well below the allowable 5 % over its entire operating temperature range.

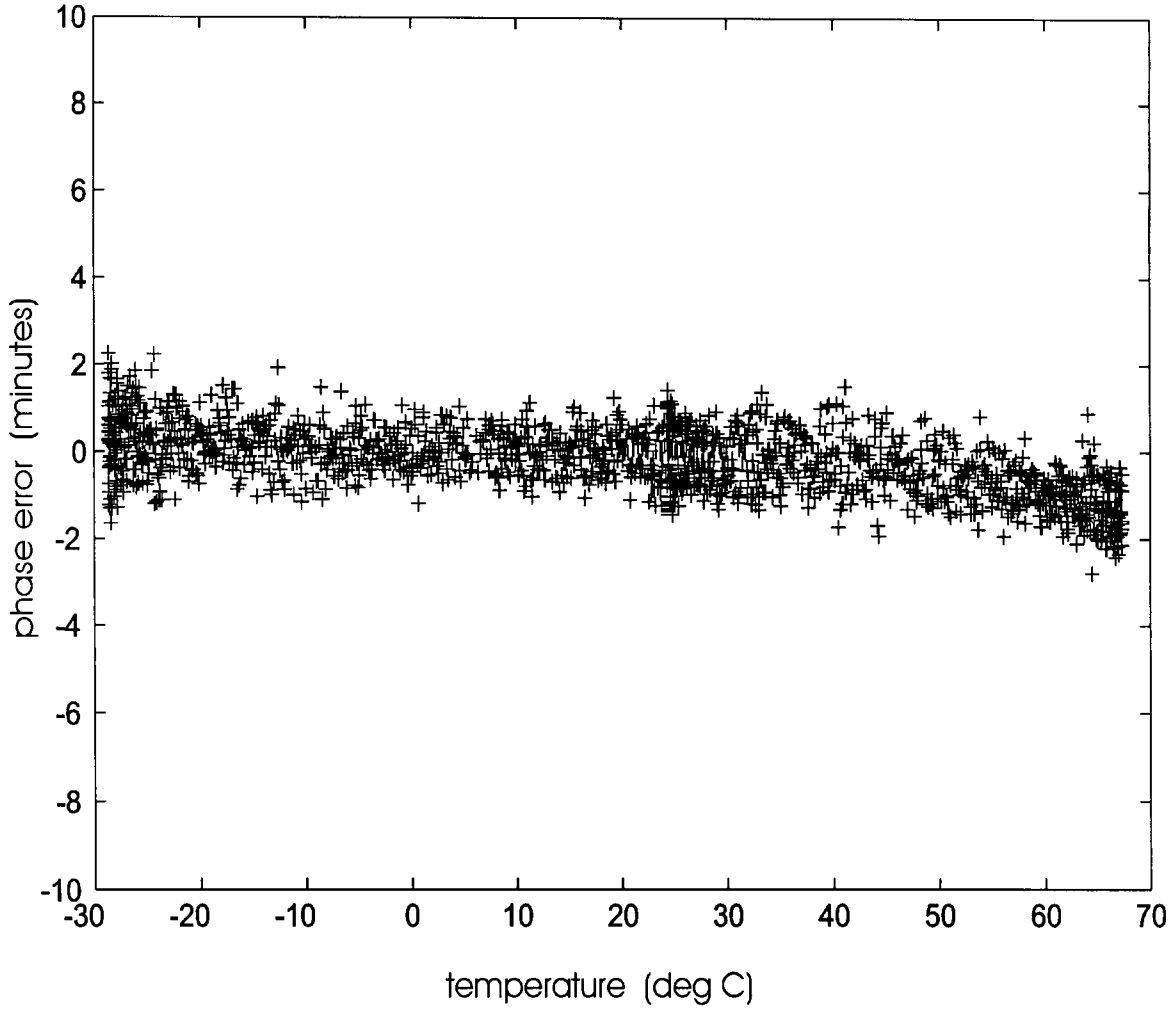

Figure 5.17: Phase error of the IOCT over the temperature range of -30 to $+70$°C range.

Chapter 6

IOPC Transfer Function: Crystallographic Issues

6.1 Introduction

In the course of this work, it was noticed that the measured transfer functions of some IOPCs showed deviations from the ideal sinusoidal transfer function [56]. For high-linearity instrumentation applications, distortion in the transfer function can lead to measurement errors. In applications where arcsine linearizing is used to enhance linearity, non-sinusoidal transfer functions will result in residual non-linearity. In this chapter, the mechanisms leading to this behavior are investigated, models are compared to measured results, and remedies are suggested.

A standard tolerance given on lithium niobate wafer axis orientation is $\pm 0.5°$ (from Crystal Technology, Palo Alto, CA). Further angular errors can be introduced during the photolithographic process if the waveguide mask is not perfectly aligned

to the crystal flat. Here, these small orientation errors will be shown to induce mode conversion in Z-propagating lithium niobate waveguides. The mode conversion in turn distorts the IOPC transfer function.

6.2 Parasitic Mode Conversion: Theory

In this section, a theory will be developed to investigate possible mode coupling mechanisms in the IOPC. More generally, the analysis is applicable to lithium niobate waveguides propagating along or near the optic axis (Z-propagating). The mechanisms that will be considered are due both to the electro-optic effect and the material anisotropy. The consideration of material anisotropy induced coupling is presented in [57] for waveguides that are misaligned in the plane of the substrate. Here the general case is considered where the waveguide can be at an arbitrary direction so long as it is near the optic axis.

The approach taken is to find the permittivity tensor, first in terms of the crystal axes, and subsequently in the waveguide coordinates which will be slightly misaligned with respect to the crystal axes. The electro-optic effect in lithium niobate induces a change in the dielectric impermeability in response to an electric field given

by [32]:

$$\Delta \begin{pmatrix} 1/n_{xx}^2 \\ 1/n_{yy}^2 \\ 1/n_{zz}^2 \\ 1/n_{yz}^2 \\ 1/n_{xz}^2 \\ 1/n_{xy}^2 \end{pmatrix} = \begin{pmatrix} 0 & -r_{22} & r_{13} \\ 0 & r_{22} & r_{13} \\ 0 & 0 & r_{33} \\ 0 & r_{51} & 0 \\ r_{51} & 0 & 0 \\ -r_{22} & 0 & 0 \end{pmatrix} \begin{pmatrix} E_x \\ E_y \\ E_z \end{pmatrix} \tag{6.1}$$

where r_{ij} are the electro-optic coefficients, and $E_{x,y,z}$ are the quasi-static electric field components. It will be assumed here that $E_y \gg E_x, E_z$ so that the device behavior is substantially "Pockels cell like." Using the relation [58]:

$$\Delta\epsilon_{ij} = -\frac{\epsilon_{ii}\epsilon_{jj}}{\epsilon_\emptyset}\Delta\left(\frac{1}{n_{ij}^2}\right), \tag{6.2}$$

the permittivity tensor in the crystal axes is:

$$\epsilon' = \epsilon + \Delta\epsilon \approx \begin{pmatrix} \epsilon_o & 0 & 0 \\ 0 & \epsilon_o & 0 \\ 0 & 0 & \epsilon_e \end{pmatrix} + \begin{pmatrix} -\frac{\epsilon_o^2}{\epsilon_\emptyset} r_{22} E_y & -\frac{\epsilon_o^2}{\epsilon_\emptyset} E_x r_{22} & \frac{\epsilon_o \epsilon_e}{\epsilon_\emptyset} E_x r_{51} \\ -\frac{\epsilon_o^2}{\epsilon_\emptyset} E_x r_{22} & \frac{\epsilon_o^2}{\epsilon_\emptyset} r_{22} E_y & \frac{\epsilon_o \epsilon_e}{\epsilon_\emptyset} E_y r_{51} \\ \frac{\epsilon_o \epsilon_e}{\epsilon_\emptyset} E_x r_{51} & \frac{\epsilon_o \epsilon_e}{\epsilon_\emptyset} E_y r_{51} & \frac{\epsilon_e^2}{\epsilon_\emptyset} r_{33} E_z \end{pmatrix} \tag{6.3}$$

where ϵ_o is the ordinary permittivity, ϵ_e is the extraordinary permittivity and $\epsilon_\emptyset$ is the free space permittivity. The permittivity tensor must be rotated into the waveguide coordinates for the coupled-mode formulation. The rotation matrices for the axial rotations are given by:

$$R_x = \begin{pmatrix} 1 & 0 & 0 \\ 0 & \cos(\theta) & -\sin(\theta) \\ 0 & \sin(\theta) & \cos(\theta) \end{pmatrix} \tag{6.4}$$

$$R_y = \begin{pmatrix} \cos(\phi) & 0 & \sin(\phi)0 \\ 0 & 1 & 0 \\ -\sin(\phi) & 0 & \cos(\phi) \end{pmatrix} \tag{6.5}$$

$$R_z = \begin{pmatrix} \cos(\psi) & -\sin(\psi) & 0 \\ \sin(\psi) & \cos(\psi) & 0 \\ 0 & 0 & 1 \end{pmatrix} \tag{6.6}$$

where the angles are defined according to Figure 6.1.

The permittivity in the rotated co-ordinate system, i.e., the waveguide coordinates, is given by:

$$\epsilon'' = R_x R_y R_z \epsilon' R_z^{-1} R_y^{-1} R_x^{-1}. \tag{6.7}$$

Evaluating Equation 6.7 and performing a Taylor series expansion to second order in ϕ, θ, ψ gives:

$$\epsilon'' = \begin{pmatrix} \epsilon_o & 0 & 0 \\ 0 & \epsilon_o & 0 \\ 0 & 0 & \epsilon_e \end{pmatrix} + \begin{pmatrix} \Delta\epsilon''_{11} & \Delta\epsilon''_{12} & \Delta\epsilon''_{13} \\ \Delta\epsilon''_{12} & \Delta\epsilon''_{22} & \Delta\epsilon''_{23} \\ \Delta\epsilon''_{13} & \Delta\epsilon''_{23} & \Delta\epsilon''_{33} \end{pmatrix} \tag{6.8}$$

where:

$$\Delta\epsilon''_{11} \approx -(\epsilon_o - \epsilon_e)\phi^2 - r_{22}E_y\epsilon_o^2/\epsilon_\emptyset \tag{6.9}$$

$$\Delta\epsilon''_{22} \approx -(\epsilon_o - \epsilon_e)\theta^2 + r_{22}E_y\epsilon_o^2/\epsilon_\emptyset \tag{6.10}$$

$$\Delta\epsilon''_{33} \approx (\epsilon_o - \epsilon_e)(\theta^2 + \phi^2) + r_{33}E_z\epsilon_e^2/\epsilon_\emptyset \tag{6.11}$$

$$\Delta\epsilon''_{12} \approx (\epsilon_o - \epsilon_e)\theta\phi - \frac{\epsilon_o^2 E_x r_{22}}{\epsilon_\emptyset} + \frac{\epsilon_o\epsilon_e E_y r_{51}\phi}{\epsilon_\emptyset} + \frac{2\epsilon_o^2 E_y r_{22}\psi}{\epsilon_\emptyset} \tag{6.12}$$

$$\Delta\epsilon''_{13} \approx (\epsilon_e - \epsilon_o)(\phi + \psi\theta) + \frac{\epsilon_o\epsilon_e E_x r_{51}}{\epsilon_\emptyset} + \frac{\epsilon_o\epsilon_e E_y r_{51}\psi}{\epsilon_\emptyset} \tag{6.13}$$

$$\Delta\epsilon''_{23} \approx (\epsilon_o - \epsilon_e)(\theta - \psi\phi) + \frac{\epsilon_o\epsilon_e E_y r_{51}}{\epsilon_\emptyset}. \tag{6.14}$$

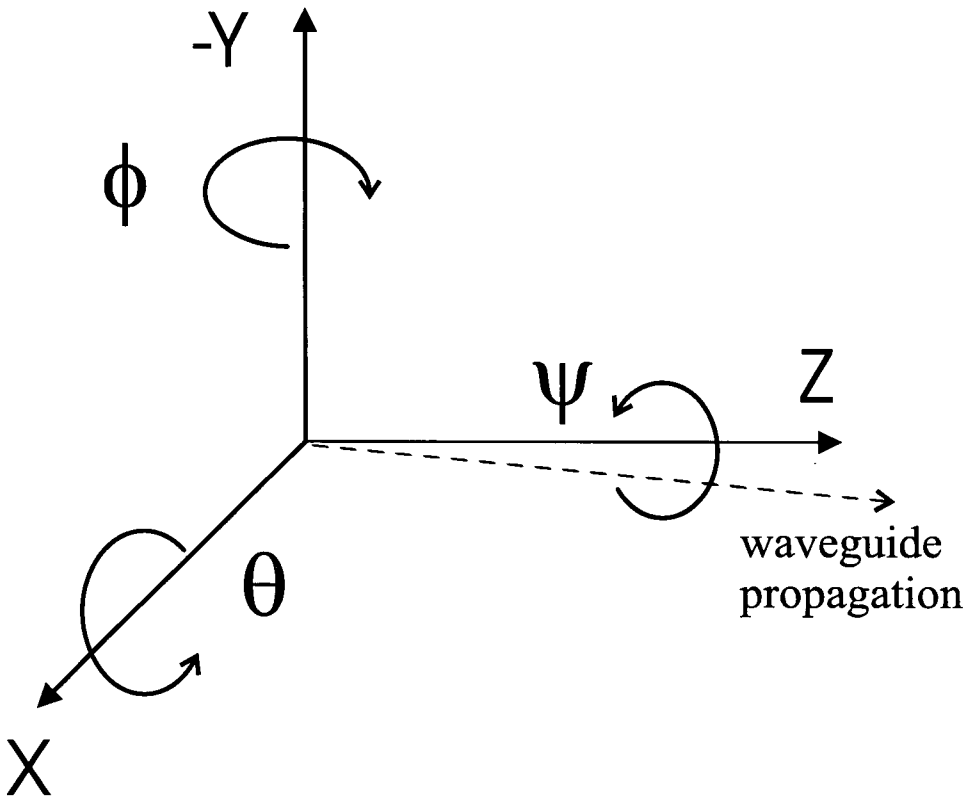

Figure 6.1: Coordinates and rotational definitions for the off-axis propagation direction. Positive angles are defined by the "Right-Hand Rule."

The coupled-mode equations will now be developed to evaluate the impact of the various coupling mechanisms considered here. The coupled-mode formulation relies on representing the behavior of a perturbed waveguide in terms of the modes of the unperturbed waveguide [58]. Since multiple coupling mechanisms between different field components are considered here, it is not possible to proceed with the scalar formulation that is often used. The modes of the perturbed waveguide will be represented by:

$$\overline{E}_a = A(z)\exp\left(-j\beta_a z\right)\overline{\varepsilon}^a(x,y) \tag{6.15}$$

$$\overline{E}_b = B(z)\exp\left(-j\beta_b z\right)\overline{\varepsilon}^b(x,y) \tag{6.16}$$

where $A(z)$ and $B(z)$ are the length dependent complex mode amplitudes, and the terms $\overline{\varepsilon}^{a,b}(x,y)$ are the normalized electric field distributions of the unperturbed modes and have the form:

$$\overline{\varepsilon}^{a,b}(x,y) = \begin{pmatrix} \varepsilon_x^{a,b}(x,y) \\ \varepsilon_y^{a,b}(x,y) \\ \varepsilon_z^{a,b}(x,y) \end{pmatrix}. \tag{6.17}$$

The objective is to solve for the amplitude functions $A(z)$ and $B(z)$. This is done by substituting the mode definitions and the permittivity tensor into the wave equation:

$$\nabla^2\overline{E} + \omega^2\mu_o[\epsilon + \Delta\epsilon^{''}]\overline{E} = 0. \tag{6.18}$$

Two differential equations that describe the behavior of the mode amplitudes are obtained from Equation 6.18 by following the procedure in Appendix A. These equations are:

$$\frac{\mathrm{d}A(z)}{\mathrm{d}z} = -\frac{j\omega^2\mu_o\epsilon_{\emptyset}}{2\beta_a}\exp\left(+j\Delta\beta z\right)\frac{\int\int \overline{\varepsilon}^{a*}(x,y)\cdot\left[\Delta\epsilon_r^{''}\right]\overline{\varepsilon}^{b}(x,y)\,\mathrm{d}x\,\mathrm{d}y}{\int\int \overline{\varepsilon}^{a*}(x,y)\cdot\overline{\varepsilon}^{a}(x,y)\,\mathrm{d}x\,\mathrm{d}y}B(z) \tag{6.19}$$

$$\frac{\mathrm{d}B(z)}{\mathrm{d}z} = -\frac{j\omega^2\mu_o\epsilon_\emptyset}{2\beta_b}\exp\left(-j\Delta\beta z\right)\frac{\int\int \overline{\varepsilon}^{b*}(x,y)\cdot\left[\Delta\epsilon_r''\right]\overline{\varepsilon}^{a}(x,y)\,\mathrm{d}x\,\mathrm{d}y}{\int\int \overline{\varepsilon}^{b*}(x,y)\cdot\overline{\varepsilon}^{b}(x,y)\,\mathrm{d}x\,\mathrm{d}y}A(z) \qquad (6.20)$$

where $\Delta\beta$ is the propagation constant mismatch given by:

$$\Delta\beta = \frac{2\pi}{\lambda_o}\left(B^m + n_o^3 r_{22}E_y + \sqrt{n_o^2 - \phi^2(n_o^2 - n_e^2)} - \sqrt{n_o^2 - \theta^2(n_o^2 - n_e^2)}\right) \qquad (6.21)$$

where B^m is the modal birefringence of the unperturbed waveguide. The propagation constant mismatch takes into account the electro-optic contribution from E_y as well as the reduction in refractive index associated with propagating off the Z-axis. When propagating off-axis, the modes can "see" some of the smaller extraordinary index. For convenience, Equations 6.19 and 6.20 can be rewritten as:

$$\frac{\mathrm{d}A(z)}{\mathrm{d}z} = B(z)K\exp\left(+j\Delta\beta z\right) \qquad (6.22)$$

$$\frac{\mathrm{d}B(z)}{\mathrm{d}z} = -A(z)K^*\exp\left(-j\Delta\beta z\right) \qquad (6.23)$$

where K is the coupling coefficient between the two modes. The fact that $\beta_a \approx \beta_b$ has been used to simplify the coupling coefficients into a single value, K, and its complex conjugate. When K is purely real or purely imaginary, the solution of Equations 6.22 and 6.23 can be found in many texts on coupled-mode theory. Since K here will turn out to be complex due to the mode overlap integrals, a general analytic solution was found by using the software package Maple V^{TM}. The solutions for the mode amplitudes are:

$$A(z) = A(0)\exp\left(\frac{jd}{2}\right)\left[\cos\left(\frac{\sigma}{2}\right) - \frac{jd}{\sigma}\sin\left(\frac{\sigma}{2}\right)\right] + B(0)2\frac{k}{\sigma}\exp\left(\frac{jd}{2}\right)\sin\left(\frac{\sigma}{2}\right) \qquad (6.24)$$

$$B(z) = -A(0)2\frac{k}{\sigma}\exp\left(\frac{jd}{2}\right)\sin\left(\frac{\sigma}{2}\right) + B(0)\exp\left(\frac{jd}{2}\right)\left[\cos\left(\frac{\sigma}{2}\right) - \frac{jd}{\sigma}\sin\left(\frac{\sigma}{2}\right)\right] \qquad (6.25)$$

where $d = z\Delta\beta$, $k = Kz$, and $\sigma = \sqrt{d^2 + 4|k^2|}$. A numerical solution is now required for the coupling coefficient K.

In order to simplify the expressions for the coupling coefficients as much as possible, an order of magnitude calculation will be done on the various contributions. The fundamental mode solutions were obtained using the full vectorial mode solver OlympIOs from C2V, Enschede, The Netherlands, for a typical lithium niobate in-diffused waveguide for a 1310 nm wavelength. The diffusion parameters used in the model were 800 Å of Ti, a 5 μm prediffusion width, and a diffusion temperature of 1050°C for 8 hours. The full vectorial field solutions are shown in Figures 6.2 and 6.3 with the relative power in each of the components. Inspection shows the dominant electric field component of the TE mode to have even symmetry in x, while the two minor components have odd symmetry in x. The dominant as well as the longitudinal electric field components of the TM mode have even symmetry in x, while the minor transverse component has odd symmetry in x. Although these symmetry conditions force odd/even components of the overlap integrals in Equations 6.19 and 6.20 to be zero, the numerical calculation will be done on all components to evaluate the numerical error in the calculations.

Table 6.1 shows the overlap integrals for each pair of field components along with the symmetry of each field in the x-direction. Overlap values for field combination with even/odd symmetry are theoretically zero as indicated. The dominant field components yield almost perfect overlap as expected. The term with $\varepsilon_y^{TE}\varepsilon_x^{TM}$ is very small, despite being non-orthogonal, because both fields are minor components. The term with $\varepsilon_z^{TE}\varepsilon_x^{TM}$ is also small despite being non-orthogonal, again, because both

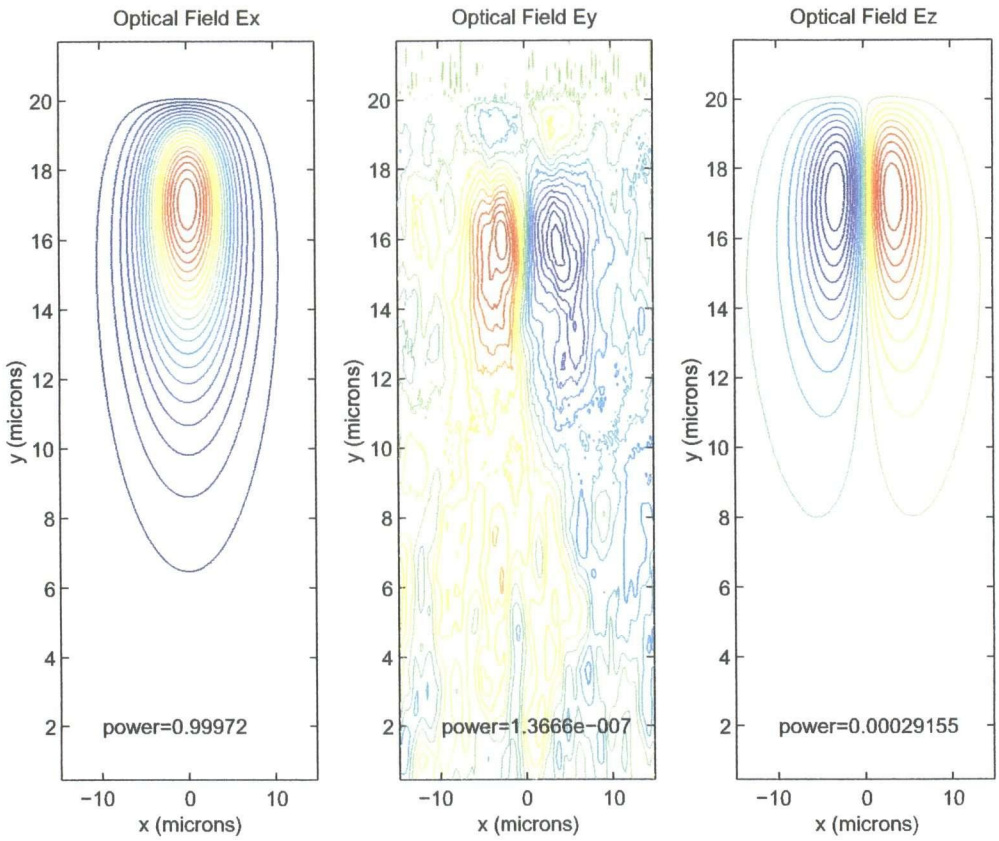

Figure 6.2: Electric field contours for the vector components of a typical TE mode. The fractional power in each component is also shown.

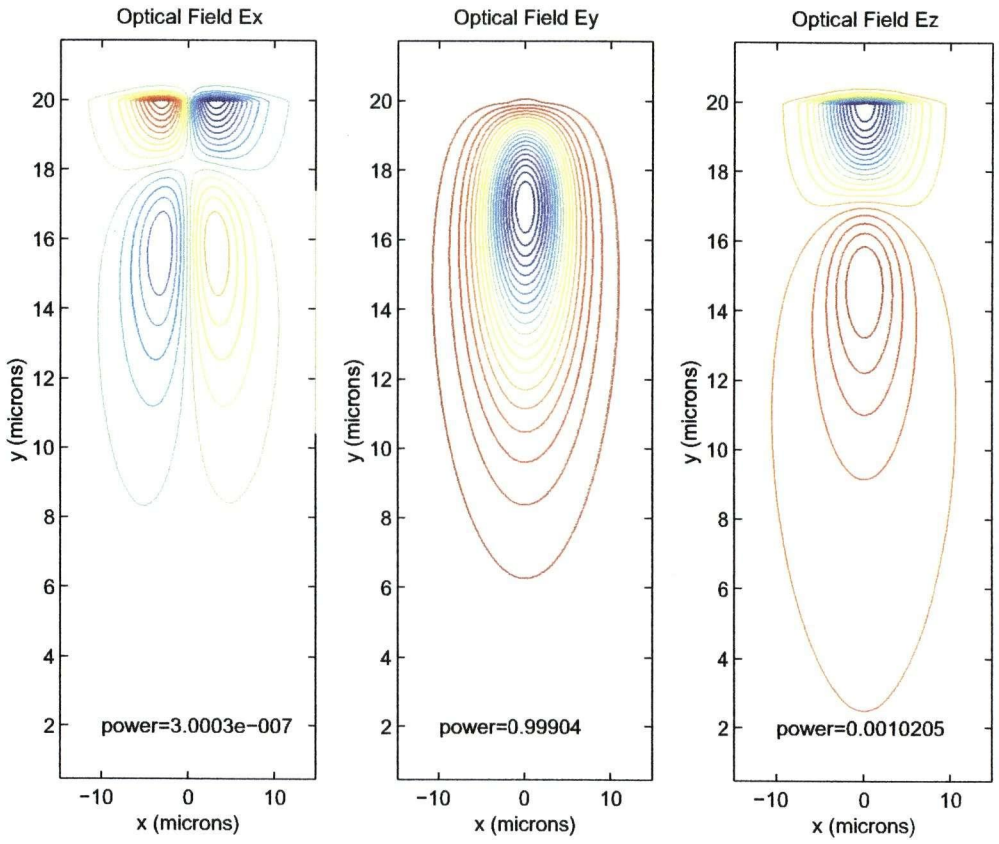

Figure 6.3: Electric field contours for the vector components of a typical TM mode. The fractional power in each component is also shown.

fields are minor although it is somewhat larger because the longitudinal components are larger than the minor transverse components. Expansion of the overlap integral in Equation 6.19, however, indicates that the $\varepsilon_z^{TE}\varepsilon_x^{TM}$ contribution is additive with the much larger $\varepsilon_x^{TE}\varepsilon_z^{TM}$ overlap. The $\varepsilon_x^{TE}\varepsilon_z^{TM}$ is significant in comparison because it includes a major field component. With this knowledge, the coupling coefficients K in Equation 6.22 can be reduced to:

$$K = \frac{-jk_o}{2n_{\text{eff}}\epsilon_\emptyset}\left[\Delta\epsilon''_{12}(\phi,\theta,\psi,E_x,E_y)\Gamma_1 + \Delta\epsilon''_{13}(\phi,\theta,\psi,E_x,E_y)\Gamma_2\right] \tag{6.26}$$

where

$$n_{\text{eff}} = \frac{\beta\lambda_o}{2\pi}, \tag{6.27}$$

$$\Gamma_1 = \frac{\int\int \varepsilon_x^{TE*}(x,y)\varepsilon_y^{TM}(x,y)\,\mathrm{d}x\,\mathrm{d}y}{\int\int \overline{\varepsilon}^{TE}(x,y)\cdot\overline{\varepsilon}^{TE*}(x,y)dxdy}, \tag{6.28}$$

and

$$\Gamma_2 = \frac{\int\int \varepsilon_x^{TE*}(x,y)\varepsilon_z^{TM}(x,y)\,\mathrm{d}x\,\mathrm{d}y}{\int\int \overline{\varepsilon}^{TE}(x,y)\cdot\overline{\varepsilon}^{TE*}(x,y)dxdy}. \tag{6.29}$$

Inspection of Table 6.1 shows that $\Gamma_1 \approx 1$ whereas the value of Γ_2 is imaginary and on the order of 1E−3.

Equations 6.24 and 6.25 can now be evaluated in terms of the off-axis angles,

Table 6.1: Calculated overlap integrals for typical fields. The X-symmetry is indicated in brackets. For values with a '*', symmetry dictates a zero value.

	$\varepsilon_x^{TM}(x,y)$ (odd)	$\varepsilon_y^{TM}(x,y)$ (even)	$\varepsilon_z^{TM}(x,y)$ (even)
$\varepsilon_x^{TE}(x,y)$ (even)	0.12E-6*	0.9986	j0.963E-3
$\varepsilon_y^{TE}(x,y)$ (odd)	0.13E-6	2.23E-6*	j0.68E-6*
$\varepsilon_z^{TE}(x,y)$ (odd)	j4.11E-6	j0.72E-6*	0.04E-6*

the applied electric fields, and the overlap integrals to see the effects on the IOPC. Measured data will be used to check their validity.

6.3 Mode Conversion Measurements vs. Theory

Various degrees of mode conversion were observed in fabricated IOPCs. Figure 6.4 shows the TM to TE mode conversion of one of the most non-ideal devices that was measured. This was measured on a Y-cut IOPC with a V_π of 598 V, fabricated with parallel plate electrodes for high-voltage sensor applications [59]. This particular IOPC was fabricated by INO, Sainte-Foy, QC, instead of at UBC. The Ti prediffusion width was 8 μm. A plate transformer and variac were used to obtain a 60 Hz, 3.2 kV_{pp} voltage source to test over several transfer function cycles. The theoretical best fit to the measured data was determined using a constant coupling coefficient, i.e., a coupling coefficient invariant with applied voltage. A good fit was obtained to Equations 6.24 and 6.25 with $d_{(E_y=0)} = 7.60$ and $|k| = 0.869$. The complex value of k cannot be determined from this measurement since Equations 6.24 and 6.25 are invariant with the angle of k when only one of the TE or TM modes is launched.

Launching equal powers into both the TE and TM modes at the same time provides information on the angle of the coupling coefficient. Figure 6.5 shows the measured TE and TM mode powers at the waveguide output as well as Equations 6.24 and 6.25 evaluated with the values of $d_{(E_y=0)} = 7.60$ and $|k| = 0.869$, determined above. The theoretical curves in Figure 6.5.a were done with $k = -j0.869$ while 6.5.b uses $k = 0.869$. The comparison clearly indicates that the value of k for this device is predominantly imaginary. The sign of the coupling coefficient is also uniquely

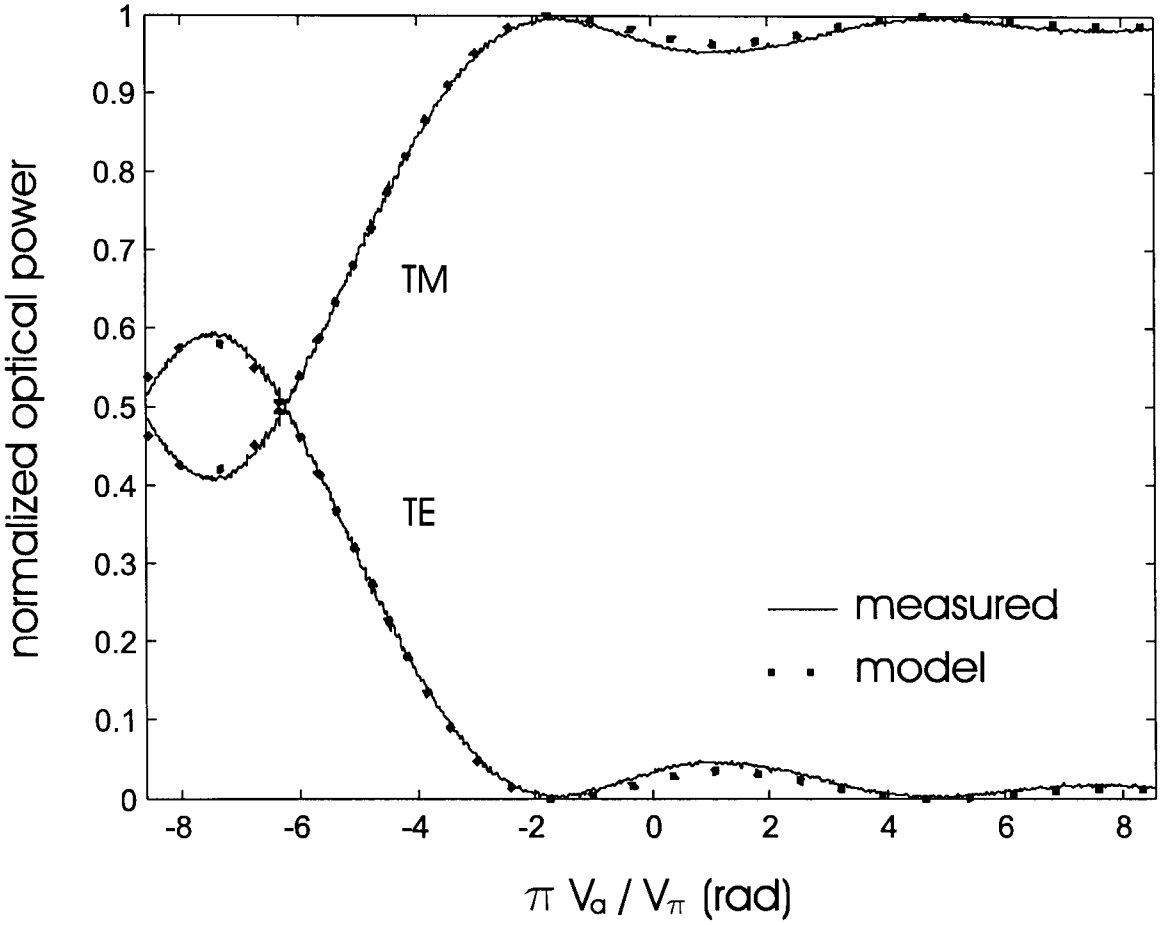

Figure 6.4: Significant mode conversion is seen in this IOPC. The TM mode was launched while both TE and TM mode powers were measured at the waveguide output. The best fit theoretical model is also shown using a constant coupling coefficient where $d_{(E_y=0)} = 7.60$ and $|k| = 0.869$.

determined since changing the sign of k interchanges the curves for the TE and TM modes.

The constant imaginary coupling coefficient determined above gives significant insights into the origin of the coupling mechanism. The imaginary coefficient results from the term with $\Delta\epsilon''_{12}$ in Equation 6.26. Furthermore, the fact that the coupling coefficient is constant requires that the dominant dielectric perturbation results from $\Delta\epsilon''_{12} \approx (\epsilon_o - \epsilon_e)\theta\phi$ in Equation 6.12. This implies that the observed mode conversion was the result of the wafer being off-axis in both θ and ϕ. Using the waveguide length of 21.4 mm, the value of $\theta\phi$ is calculated to be 1.16E-4 rad^2, or $(0.62°)^2$. This is just over the typical limit of $\pm 0.5°$ for the crystallographic orientation tolerance. Since ϕ also includes any mask angular alignment error, it is quite possible that this wafer did conform to a $\pm 0.5°$ specification. There is also an uncertainty of approximately $\pm 20\%$ in the coupling coefficient due to the assumption of a static coupling coefficient (see Section 6.6).

6.4 Birefringence Measurement

The mode conversion analysis developed here can be used to measure the modal birefringence of the waveguide. Other techniques are available but have limitations. The intrinsic bias of the IOPC is a function of the birefringence but a direct measurement of the bias can only provide a relative bias value over the range of $\pm\pi$. The cut-back technique [14] can be used to determine birefringence but the cut-back method is destructive. Wavelength scanning can provide a birefringence measurement but this approach can suffer from ambiguity due to dispersion in the modal birefringence.

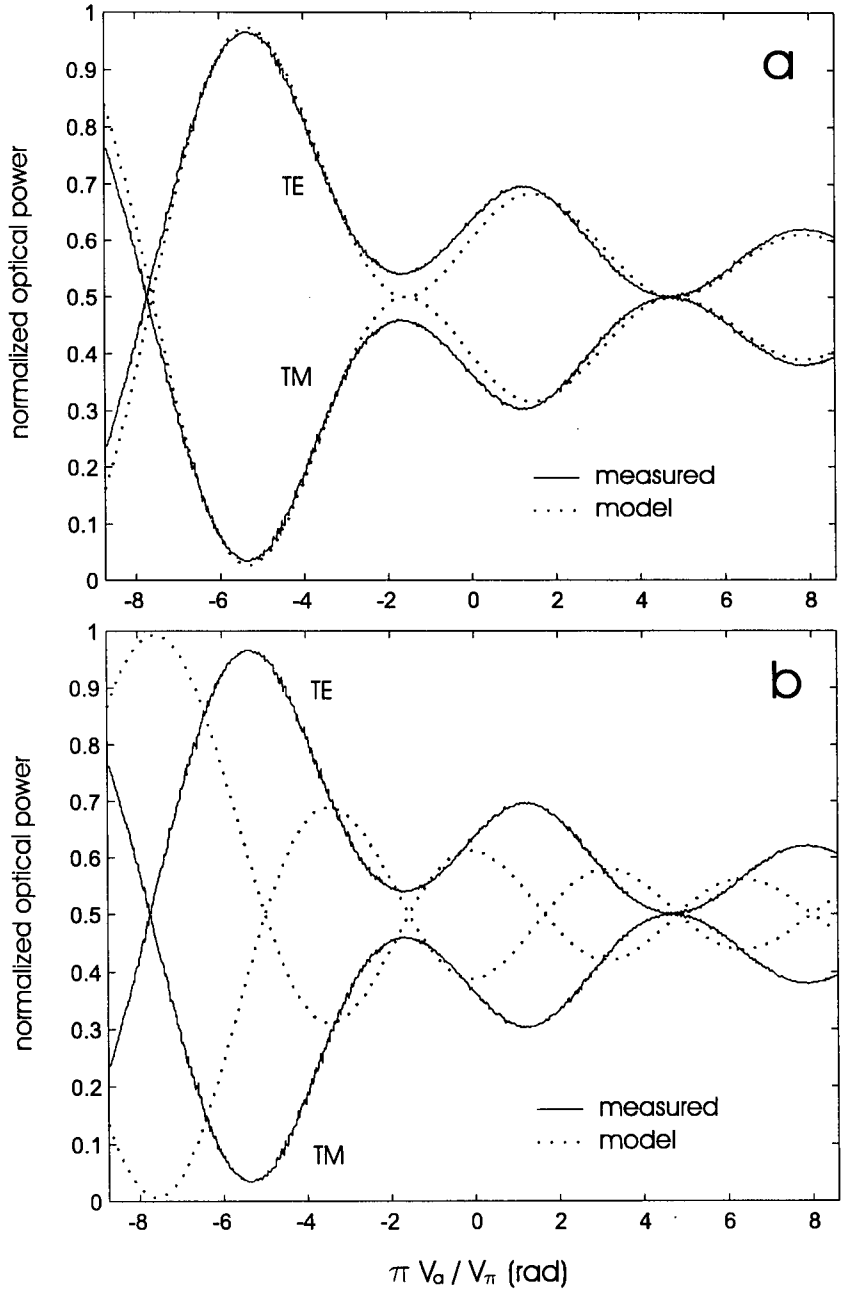

Figure 6.5: The mode conversion is measured for the same device as Figure 6.4 but with both TE and TM modes launched. (a) shows good agreement with the theoretical fit with $d_{(E_y=0)} = 7.60$ and $k = -j0.869$, while (b) shows poor agreement to the same measured data using $k = 0.869$. Clearly the coupling coefficient is predominantly imaginary.

Mode conversion measurements, on the other hand, can give a direct indication of the birefringence. For the IOPC mode conversion measurements presented in Figure 6.4, the value of d was determined by fitting Equation 6.24 to the data using $A(0) = 0$. This value of d gives the birefringence, including any off-axis contributions, from Equation 6.21 as:

$$B = \frac{d_{(E_y=0)}\lambda_o}{2\pi L} \tag{6.30}$$

where L is the electrode length. Here, $L = 21.4$ mm and $d_{(E_y=0)} = 7.60$, giving a birefringence of 7.4E−5. This measurement was verified to be correct using cut-back measurements.

In cases where a larger modulation of d is possible, a curve fit is not necessary. Equation 6.24, with $A(0) = 0$, has even symmetry about $d = 0$. This fact is illustrated in Figure 6.6. The dashed lines indicate the maximum and minimum values of k that are expected for a typical 2 cm long IOPC that has $\pm 0.5°$ crystallographic alignment tolerance. Within these limits, the mode conversion signature reaches its peak value at $d = 0$. Determining the birefringence from a measured mode conversion signature requires determining the value of d at zero voltage, that is $d_{(E_y=0)}$. d is related to the applied voltage, V_a, according to:

$$d = \frac{V_a}{V_\pi}\pi + d_{(E_y=0)}. \tag{6.31}$$

This gives:

$$d_{(E_y=0)} = -\frac{V_{peak}}{V_\pi}\pi \tag{6.32}$$

where V_{peak} is the voltage corresponding to the mode conversion peak. Measurement examples using the mode conversion peak will be given in the following section. Lastly,

it should be noted that this method for measuring birefringence requires the coupling coefficient to be non-zero. This requirement was satisfied in all of the IOPCs tested here. Nevertheless, if an IOPC were to have a vanishingly small coupling coefficient, it would be sufficient to apply a static X-directed electric field through the waveguide to increase the coupling coefficient.

6.5 Off-Axis Propagation Experiment

To further characterize mode conversion resulting from off-axis propagation, an experiment was conducted by fabricating, at UBC, waveguides that were intentionally off-axis. The experiment consisted of creating a series of waveguides on a Y-cut lithium niobate substrate at a range of angles from $\phi = -1°$ to $+1°$ off the nominal Z crystallographic axis in increments of 0.1°. The Ti prediffusion width was 6 μm; the thickness was 750 Å; the diffusion time was 8 hours at 1050°C. The sample was coated with 2700 Å of sputtered SiO_2 as an optical buffer layer over the waveguides. Subsequently, both sides of the sample were coated by evaporating 200 Å of Cr for adhesion, and finally 2300 Å of Al as electrodes. The ends of the sample were sandwiched with lithium niobate cover blocks and polished for end-fire coupling. The final sample length was 28 mm. The half-wave voltage was 197 V.

The first verification of the theory performed was measuring the change in modal birefringence as a function of the off-axis angle ϕ predicted by Equation 6.21. This was done by applying a 60 Hz voltage to the electrodes, launching equal optical powers into the TE and TM modes, interrogating the TE and TM modes at the output with an analyzer at 45°, and observing the electro-optic transfer function

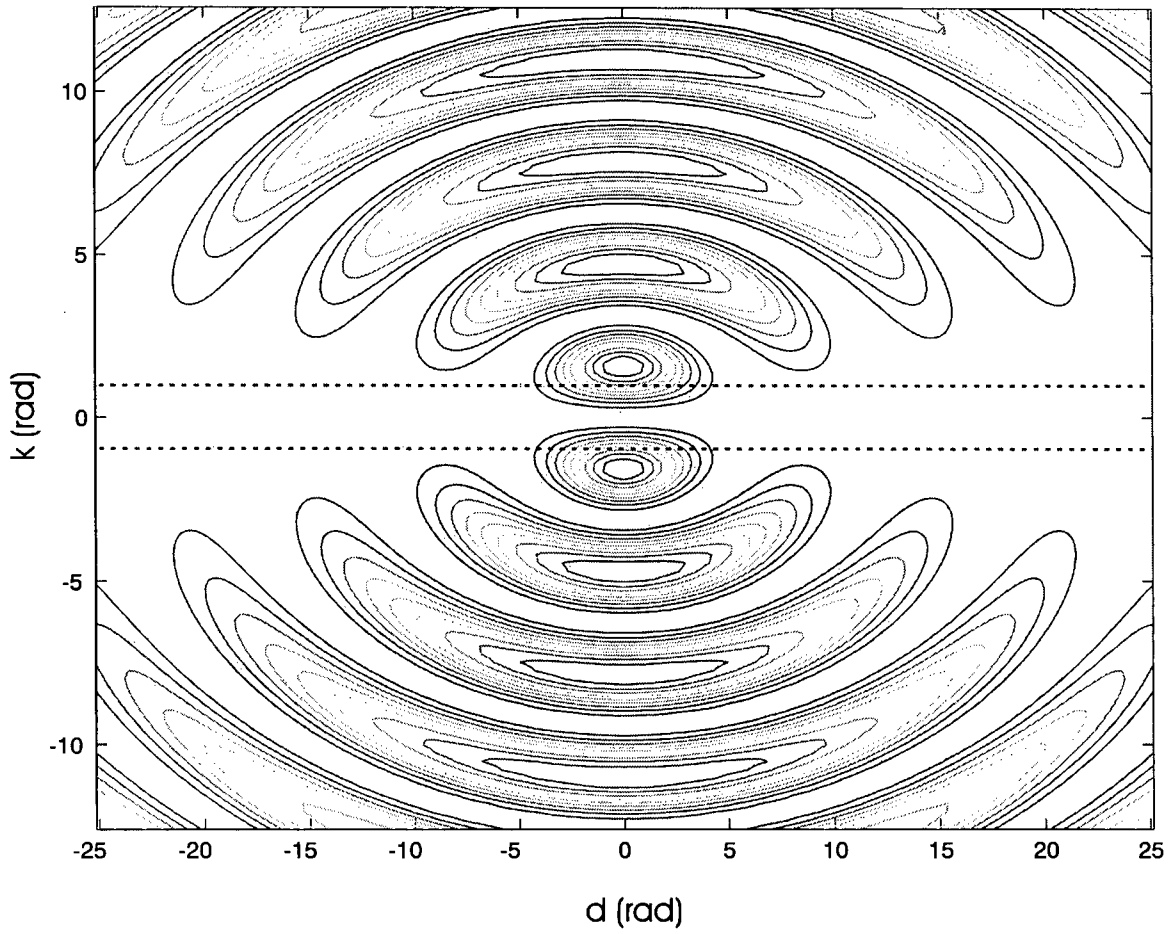

Figure 6.6: This figure shows a contour plot of Equation 6.24 with $A(0) = 0$ and $B(0) = 1$ as a function of k and d. The mode conversion pattern is symmetric about $d = 0$. This fact enables the birefringence of an IOPC to be determined by locating the $d = 0$ position in the measured mode conversion as a function of the electrode voltage. The dashed lines indicate the maximum and minimum values of k that are expected on a typical 2 cm long IOPC that has $\pm 0.5°$ crystallographic alignment tolerance.

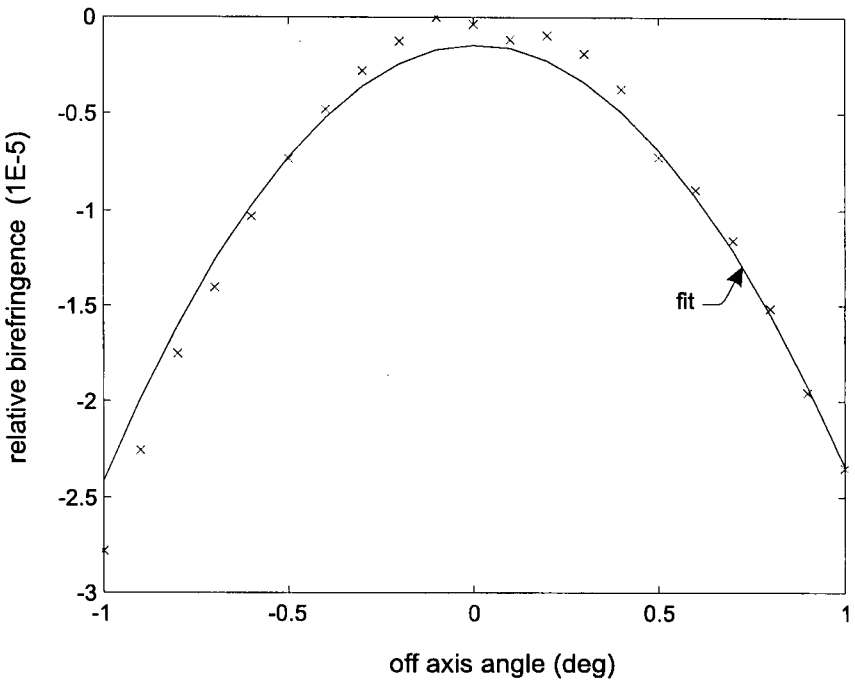

Figure 6.7: Measured relative birefringence as a function of the nominal off-axis propagation angle ϕ.

with a photodetector (New Focus model 2033) and an oscilloscope. The optical bias point was measured from which the relative birefringence was calculated according to Equation 3.2. Figure 6.7 shows the measured data as well as the best fit of Equation 6.21. An offset in the measured value of ϕ was allowed since only the relative angles were known. The results agree very well, and also indicate that in this particular case, the combined errors due to the wafer flat accuracy as well as the mask alignment to the wafer flat are nearly zero, as shown by the symmetric result.

The next measurement that was performed was measuring the change in mode conversion as a result of changing ϕ. Figure 6.8 shows the measured modal powers as a function of electrode voltage for a TM launch for both $\phi = 0°$ and $\phi = 1°$.

The mode conversion is seen to be much weaker here than it was in the device from Figure 6.4. Clearly being off-axis in the plane of the substrate (a variation in ϕ) is not the sole determinant of the coupling coefficient. The results here suggest that in this particular wafer, the value of θ is nearly zero, thereby weakening the $\phi\theta$ term in Equation 6.12. We can, nonetheless, determine the birefringence of each waveguide using the mode conversion technique. At $\phi = 0°$, the mode conversion peak occurs at -12 rad, which, using Equation 6.30, gives a birefringence of 9.1E-5. At $\phi = 1°$, the peak has moved to a smaller value of d because the TE mode begins to interact with the smaller extraordinary index. This measurement gives a birefringence of 4.7E-5. Comparison of these values with the relative birefringence plotted in Figure 6.7 shows that there is a consistency error of approximately 2E$-$5. If a more accurate measurement is desired, the result of the mode conversion measurement can be used to resolve the unknown multiple of 2π in the intrinsic bias point of the measured IOPC transfer function. This method gives a birefringence of 8.6E-5 and 6.4E-5 for $\phi = 0°$ and $\phi = 1°$, respectively. The error, based on the uncertainty in the measured intrinsic bias point, is estimated to be below 0.6E-5.

Figure 6.9 shows the mode conversion with equal TE and TM mode powers launched for the same sample with $\phi = -1°$, $0°$, and $1°$. A good fit to the model could not be obtained this time using the constant coupling coefficient assumption. This is expected if the $\phi\theta$ term in Equation 6.12 is small, or, if the variable part of the coupling coefficient moves in the direction of reduced coupling for the voltage polarity that gives zero birefringence. The response at $\phi = -1°$ is characteristic of an imaginary coupling coefficient where the beating powers only cross once near the

zero birefringence point (see Figure 6.5). At $\phi = 0°$, the mode conversion is slightly larger near the peak from Figure 6.8 at -12 rad but little can be said about the coupling coefficient since it is near zero. The mode conversion at $\phi = +1°$ shows a more complicated structure. This type of pattern can be recreated in the model if the minimum magnitude of the coupling coefficient coincides with the minimum birefringence point. The next section will explore the dependence of the coupling coefficient on the axial alignment and applied voltage.

6.6 Implications of Crystal Alignment for the IOPC

The coupling coefficient will be analyzed to get a better understanding of the magnitude of mode conversion that can result from crystal alignment errors. The coupling coefficient K provides a good metric of the degree of mode conversion. The units of K are rad/cm, and can be compared with the phase mismatch, $\Delta\beta$, also in rad/cm. If K is on the same order as $\Delta\beta$, significant mode conversion will occur; specifically, if $2K = \Delta\beta$, 50 % mode conversion can result.

Figure 6.10 shows the magnitude and phase of the calculated coupling coefficient, K, as a function of the angles ϕ and θ. The results are given for three different applied voltages: $-2V_\pi$, 0, and $+2V_\pi$. The variation in K as a function of ψ is shown in the corners of each quadrant where: $\square$ indicates $\psi = -0.5°$, $\circ$ indicates $\psi = 0°$, and $\diamond$ indicates $\psi = +0.5°$. The limits on θ and ϕ are $\pm 0.5°$, corresponding to the standard alignment tolerances. The plots show that the coupling coefficient is much stronger when both angles ϕ and θ are non-zero. This contribution comes from $\Delta\epsilon''_{12}$, meaning it results in an imaginary coupling coefficient. The effects of changing the

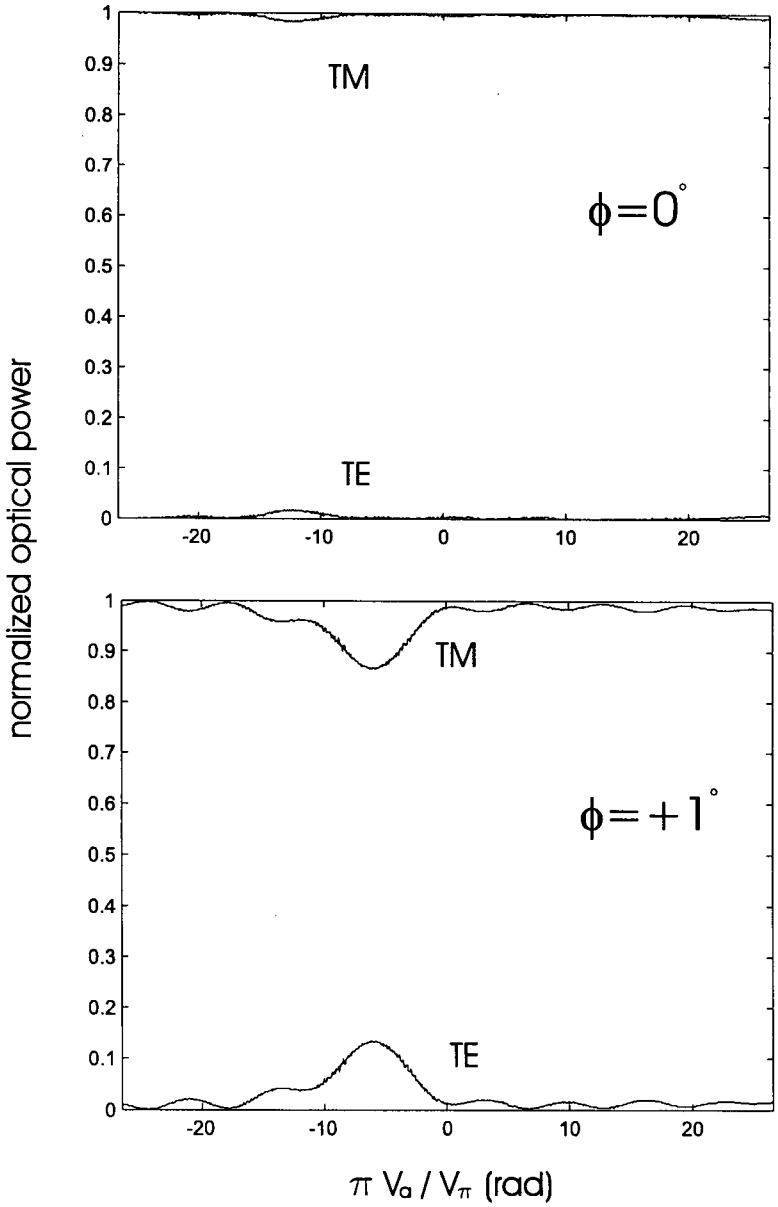

Figure 6.8: Measured mode conversion signature obtained with a TM launch on waveguides with $\phi = 0°$ and $\phi = +1°$.

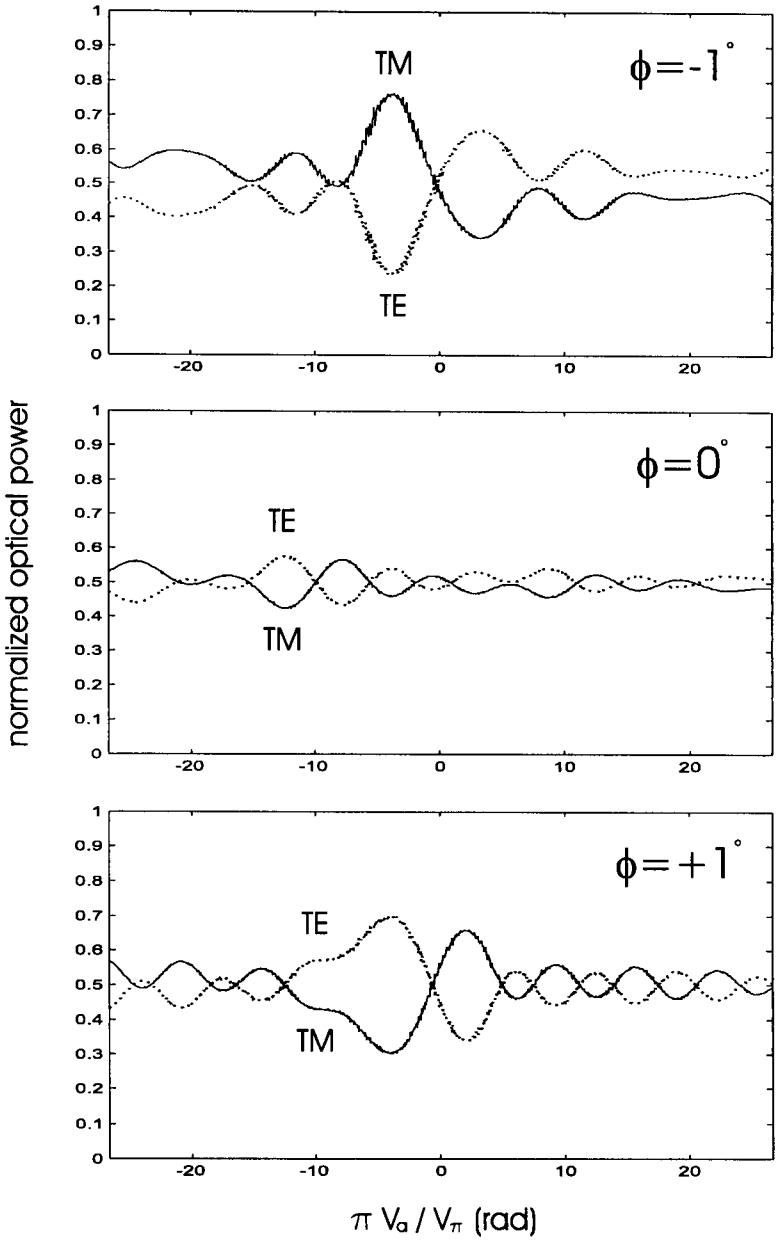

Figure 6.9: Measured mode conversion signature obtained with equal powers launched into the TE and TM modes for waveguides with $\phi = -1°$, $\phi = 0°$, and $\phi = +1°$.

applied voltage or the angle ψ are smaller, representing changes on the order of ± 20 % in the maximum coupling coefficient. In the case of $V = 0$, changing ψ has no effect. The coupling coefficient reaches 0.35 rad/cm, meaning that full power transfer would result in 2.9 cm if the modal birefringence goes to zero.

Since the correct functioning of the IOPC requires that significant mode conversion not occur, it is important to limit coupling. Firstly, it is critical that the alignment of the wafer to the mask during the photolithography process be accurate, preferable on the order of $\pm 0.1°$ to be insignificant compared to the wafer flat accuracy. This may preclude the use of mechanical alignment pins during the alignment process, necessitating a visual alignment of the mask to the wafer flat. The wafer flat used here was 20 mm long, from which $\pm 0.1°$ alignment accuracy can be obtained if the mask is kept within 35 μm along the length of the flat.

Another parameter that can be controlled to limit mode conversion is birefringence. So long as the coupling coefficient is kept smaller than the birefringence, significant mode conversion can be suppressed in the vicinity of zero volts, i.e., the passive bias point of the IOPC. The birefringence can be increased by making the modes more strongly guiding [52], or by increasing the asymmetry of the modes. The penalty for doing this is that the bias change per unit length of the waveguide increases. This makes it more difficult to fabricate IOPCs that are biased at quadrature without the need for trimming the waveguide length. It was suggested by [52] that a low birefringence waveguide at quadrature would be more manufacturable for this reason; however, the results shown here indicate that a low birefringence waveguide could be problematic in terms of mode conversion. This suggests that an optimum

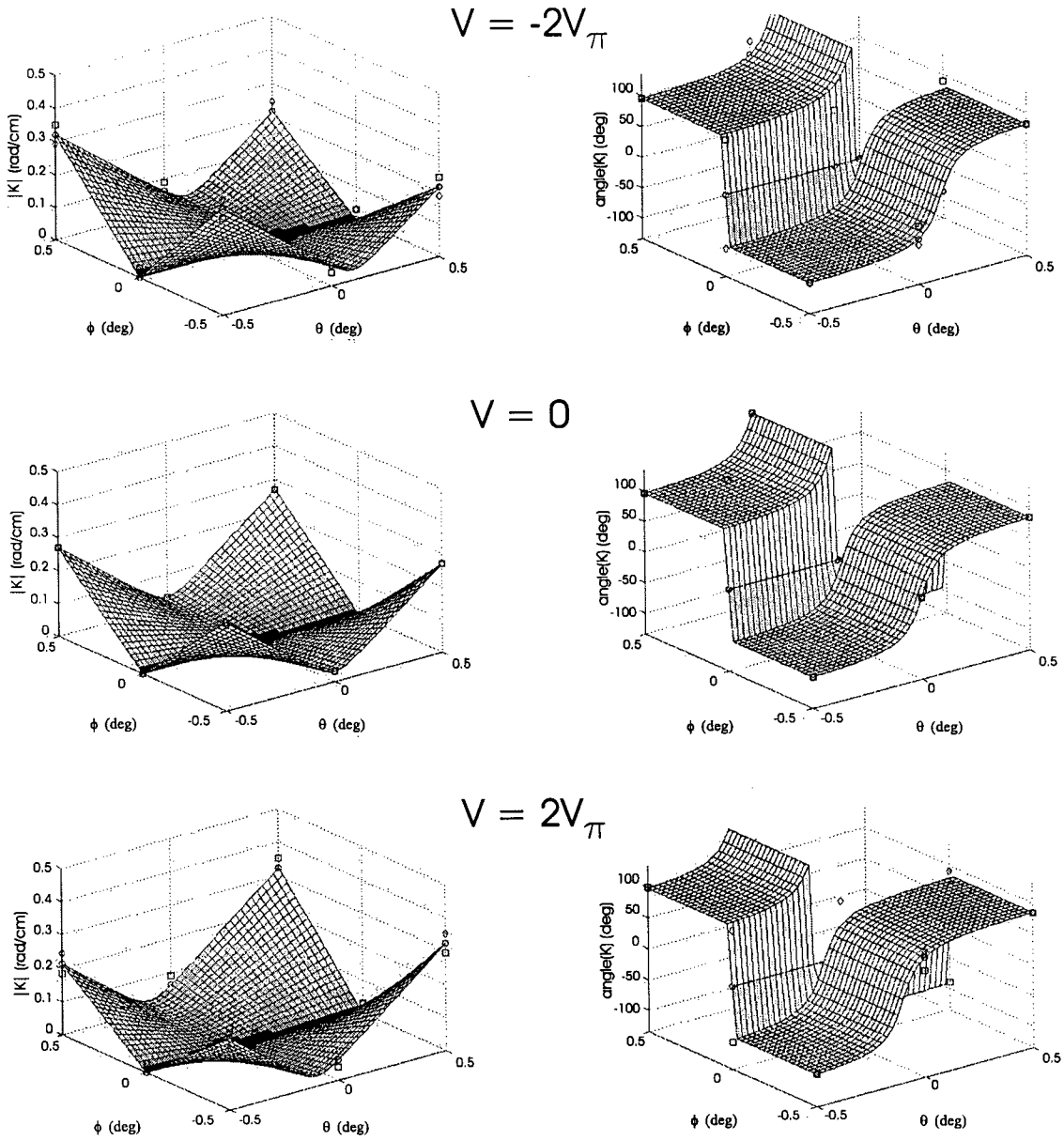

Figure 6.10: Magnitude and angle of the calculated coupling coefficient K in rad/cm as a function of the angles ϕ and θ over the range of $\pm 0.5°$. Three values of applied voltage are shown, from top to bottom: $-2V_\pi$, 0, $+2V_\pi$. The variation in K as a function of ψ is shown in the corners of each quadrant where: $\square$ indicates $\psi = -0.5°$, $\circ$ indicates $\psi = 0°$, and $\diamond$ indicates $\psi = +0.5°$.

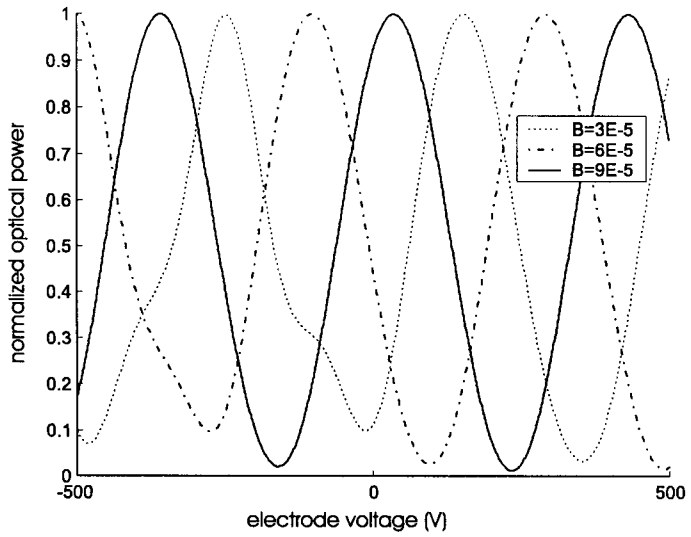

Figure 6.11: Calculated transfer functions, with $\phi = 0.5°$ and $\theta = 0.5°$, at three different values for the birefringence.

birefringence value will exist for a given manufacturing process.

Figure 6.11 shows how increasing the birefringence can improve the quality of the transfer function. Shown are calculated transfer functions for three values of birefringence (3E-5, 6E-5, and 9E-5) with $\phi = 0.5°$ and $\theta = 0.5°$. The highest birefringence case shows the desired sinusoidal transfer function in the vicinity of zero voltage. Figure 6.12 shows the mode conversion plots with a TM launch for this example. The effect of increasing the birefringence is to move the peak mode conversion location away from the zero voltage point.

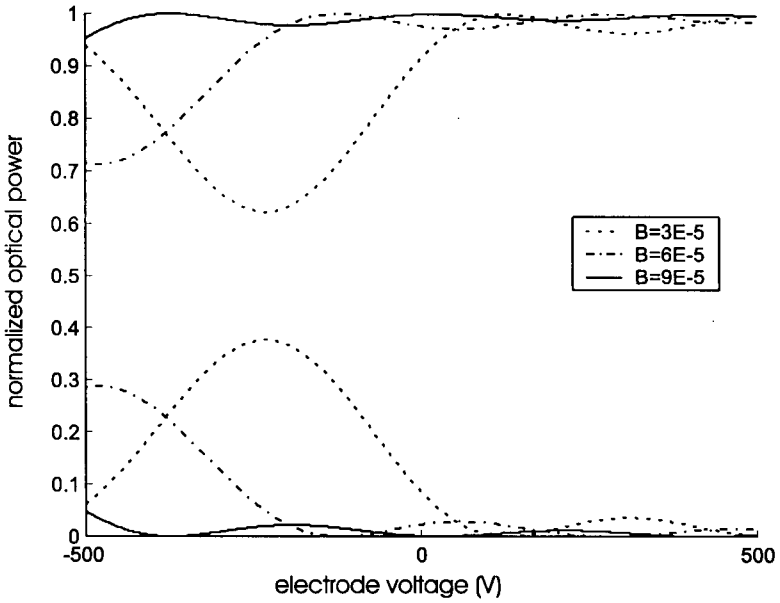

Figure 6.12: Calculated mode conversion, with $\phi = 0.5°$ and $\theta = 0.5°$, at three different values for the birefringence.

6.7 Parasitic Mode Conversion and Small-Signal Sensitivity

The last issue that will be discussed is the impact of parasitic mode conversion on the small-signal sensitivity of the transfer function (dP/dV). As indicated in Chapter 2, the dynamic range of the IOPC is extended by applying an arcsine with digital signal processing to linearize the sinusoidal transfer function. If the IOPC transfer function were perfectly sinusoidal, this linearization would produce a constant small-signal sensitivity as a function of the bias point. It has been shown above that mode conversion can distort the transfer function of the IOPC. This distortion will show up as a residual change in sensitivity with bias, despite the linearizing process.

Figure 6.13 shows the small-signal sensitivity, again with $\phi = 0.5°$ and $\theta =$

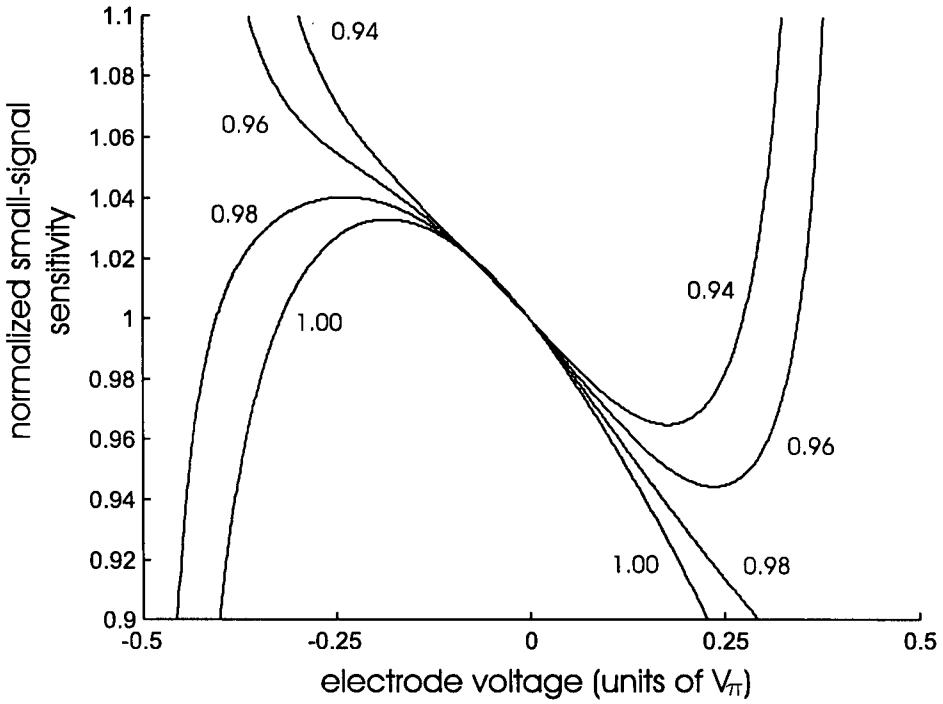

Figure 6.13: Calculated normalized small-signal transfer function sensitivity after linearizing, with $\phi = 0.5°$ and $\theta = 0.5°$, at four different values of assumed α: 0.94, 0.96, 0.98, 1.00.

0.5°, for several values of assumed α in Equation 3.1 (related to the on-off ratio). The corresponding complementary transfer functions are shown in Figure 6.14. It is apparent that the complementary transfer functions have different on-off ratios, that is, different values for α, thus representing a departure from Equation 3.1. The transfer function P_1 has an apparent value of α of 0.95, while P_2 has an apparent value of α of 1.00. It is seen in Figure 6.13 that no value of α will perfectly linearize the transfer function. This behavior was seen in the measured data shown in Figure 5.15. The preferred value of α to use in the normalization is somewhat subjective and depends on the range of bias over which a flat response is needed.

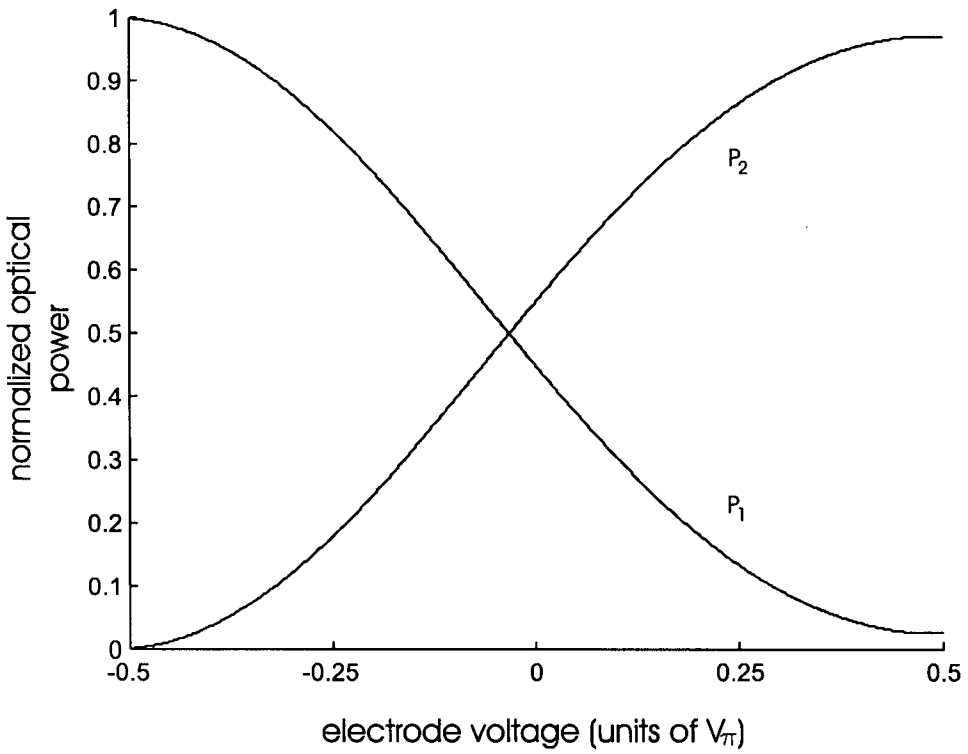

Figure 6.14: Calculated complementary transfer functions with $\phi = 0.5°$ and $\theta = 0.5°$. Non-equal extinction ratios are clearly seen.

Chapter 7

Summary, Conclusions, and Recommendations for Further Work

7.1 Summary and Conclusions

Optical instrumentation has attracted considerable interest over the years for high-voltage applications. Optical fibers, by virtue of their all dielectric construction, are highly resistant to electrical breakdown and electro-magnetic interference which makes them ideally suited for signal transmission in substation environments. Difficulties in achieving accurate and cost effective current sensors with all-optical techniques have led to the development of hybrid sensors. In this thesis, a novel hybrid current sensor was presented that has addressed the limitations of prior hybrid sensors. The results achieved here are unmatched in terms of linearity, dynamic range,

and temperature stability. The key developments that produced these results will be summarized.

The Rogowski coil was selected as a current-to-voltage transducer for this work because of its unparalleled linearity. It does not suffer from the core saturation that affects conventional current transformers, nor does it inherently dissipate power as is the case with shunt resistors. A Rogowski coil constructed on a highly dimensionally stable material, e.g., the epoxy-glass used here, also provides excellent thermal stability. The drawback of the Rogowski coil is that its terminal voltage is proportional to the derivative of the primary current. This relationship means that an integrator must be implemented, also with excellent stability.

The integrator, although simple in concept, is difficult to implement because of low-frequency noise. The integrator amplifies spectral components inversely proportional to frequency, making the location of the integrator along the signal path a key factor. It was shown that integration after the optical signal path, including digital integration, was unsuitable. In this configuration, the integrator amplifies slow bias drifts in the IOPC, creating an apparent low-frequency current noise. Residual non-linearity in the IOPC signal path also caused low-frequency signal artifacts because of rectification. For these reasons, a passive integrator was developed and constructed that could be placed in the high-voltage environment to avoid integrating low-frequency optical noise. Ultrastable resistors and capacitors were obtained and tested with stabilities better than 30 ppm/°C. To improve the gain/phase response of the passive integrator, a phase compensating circuit was incorporated into the passive integrator to minimize attenuation at the power frequency while still providing a

phase response that was flat to within 5 minutes of arc at 20 Hz and above. The results showed that passive integration can be very effective for 60 Hz instrumentation.

The optical sensor used here, the integrated-optic Pockels cell (IOPC), was designed for accurate low-voltage signal detection in a high-voltage environment. Previous work on IOPCs focused on immersion sensors with half-wave voltages on the order of 600 V. Here, the IOPC was optimized for high sensitivity so that it could detect low-voltage signals, on the order of millivolts to volts. To bring the half-wave voltage down to the 20 V range, several integrated electrode structures were designed, fabricated, and tested. A thirty-fold reduction in half-wave voltage was obtained using electrodes with gaps on the order of 20 μm and electrode lengths on the order of 20 mm.

Optical stability is typically the dominant source of error for hybrid current sensors that use analog signal transmission. The advantage, though, of using analog signal transmission is that there is no need for active circuitry in the high-voltage environment. Reliability is, therefore, increased and there is no need for supplying power in the high-voltage environment to the sensor-head. The primary difficulty encountered in developing a high-sensitivity IOPC, that was stable enough for precision instrumentation, was achieving a sufficiently flat frequency response at 60 Hz and below. We determined that SiO_2 could not be used as an optical buffer layer because of slow charge screening mechanisms that introduced phase and magnitude errors at the power frequency. Devices fabricated on X-cut lithium niobate substrates were shown to be superior to their Y-cut counterparts since X-cut devices could be used in a two-strip electrode configuration, without an optical buffer layer. We also

determined that the lithium niobate surface was highly sensitive to contamination during processing. Only lift-off and shadow-mask processes were used after the Ti indiffusion to protect the lithium niobate surface. IOPCs with phase errors as low as 2 minutes of arc were achieved with these techniques.

The effect of vibration on sensor accuracy was investigated. The noise induced by vibrating the polarization maintaining (PM) fiber at the output of the IOPC was investigated in detail. It was found that angular errors on the order of 1° between the PM fiber and the polarizing beam splitter could cause unacceptable errors in the measurement of harmonics. An efficient and effective solution based on coherence control was presented. A broadband optical source was combined with a sufficiently long PM fiber to eliminate coherent interference between the fast and slow modes at the PM fiber termination. With this approach, the alignment tolerance of the fibre axes can be greatly relaxed.

Pigtailing and packaging the IOPC were critical steps in achieving sensor accuracy. The key issue was obtaining a stable optical bias response as a function of temperature with minimal hysteresis. The optical bias point must have a one-to-one relationship with temperature so that the bias can be used to compensate for temperature variations in the sensor's magnitude accuracy. The key factor in the pigtailing procedure was using an ultra-violet cure adhesive with a glass transition temperature that was above the operating temperature range. In packaging the IOPC, it was critical that the package not stress the lithium niobate substrate as a result of temperature change or mechanical mounting. This was accomplished with a rigid fiberglass package, isolated from the substrate by a crystallographically matched lithium niobate

subcarrier, all interfaced with an ultralow stress adhesive.

High current measurements were performed to evaluate the suitability our new hybrid current sensor for metering and relaying applications. The results showed the sensor to exceed IEEE and IEC linearity standards for 0.3 and 0.2 % metering accuracy at a nominal current of 3 kA. The linearity was better than 0.3 % from 30 A to 30 kA. The same sensor was also shown to achieve better than 0.5 % instantaneous accuracy when measuring transient over-currents at 30 kA. Frequency response was also measured and shown to simultaneously satisfy all three classes in the draft IEC standard, 60044-8 for electrical current transducers, for Power Metering, Quality Metering, and Protection for Usual Purposes. The thermal stability of the sensor was shown to be capable of achieving 0.3 % accuracy from -30 to $+70$°C. These results are unmatched by other hybrid sensors.

In the course of fabricating IOPCs for this work, it was observed that some waveguides had an unexpected conversion of power between the TE and TM modes. The mode conversion was found to result in non-sinusoidal transfer functions, producing non-linearity even after linearizing using the arcsine function. Residual non-linearity was shown to be problematic due to rectification in the case where the Rogowski coil signal was integrated after transmission with the IOPC. Residual non-linearity also shows up as a ratio variation with optical bias and so increases the possibility of measurement error over bias drift.

A new theoretical model for the IOPC was developed using coupled-mode theory to explain the mode conversion in terms of small crystallographic alignment errors. The dominant mode coupling mechanism was shown to be proportional to the

product of two orthogonal angular misalignments of the waveguide axis with respect to the optic axis. Excellent agrement was obtained between the theoretical and measured results. It was concluded that small crystallographic alignment errors can have a profound effect on the ideality of the IOPC transfer function and should, therefore, be minimized. It was also shown that using waveguides with large modal birefringence provides an effective way to suppress mode conversion in the presence of the typical $\pm 0.5^{\circ}$ crystallographic alignment tolerance specified by wafer manufacturers.

Lastly, the off-axis waveguide model developed here was also used to provide a new, non-destructive method for measuring birefringence in IOPCs. This technique is non-destructive and unambiguous and, as such, provides a distinct advantage over the conventional cut-back method.

7.2 Recommendations for Future Work

Future work should target further improvements to the temperature stability of the IOPC. It was observed in the course of this work that the bias of the IOPC could jump by 0.02 radians in less than 15 μs. This effect has been attributed to pyroelectric discharge but was not confirmed. The rate of occurrence of these jumps was reduced by coating the Z-directed facets with Y_2O_3; however, the jumps were not eliminated. A more conductive coating such as indium tin oxide (ITO) could be tried as suggested in [52] to enhance bias stability. The Y_2O_3 coating used here also served as an AR coating; using a more conductive coating such as ITO might require using angled facets to defeat back-reflections.

An alternative to using conductive coatings is to chemically reduce the lithium

niobate with hydrogen. This process has been demonstrated to stabilize surface acoustic wave (SAW) filters from pyroelectric effects in [60] where the authors report that between 8 and 12 rapid ($\sim$ 10 ns) voltage bursts would be recorded on an untreated lithium niobate SAW filter when cooling from 70 to -30°C at a rate of 1°C/min. These reported bursts are consistent with the type of behavior observed when temperature cycling IOPCs over the same temperature range. After reducing the SAW filers in hydrogen at temperatures ranging from 400 to 740°C, the authors in [60] report complete suppression of pyroelectric bursts. The reduced lithium niobate suffers from increased absorption, and, as such, for optical waveguide applications, the waveguide itself may need to be masked during the reduction process. The electrode region may additionally need to be masked to avoid phase errors that could result from the increased conductivity of the reduced lithium niobate.

The dynamic range of the sensor could be further enhanced by stabilizing the total bias change as a function of temperature. Although it is desirable that the bias change with temperature to act as a thermometer for making ratio corrections, excessive bias change reduces the available modulation depth at the temperature extremes. It was observed that packaging stress could have a dramatic effect on the IOPC bias point. This suggests that stress could be used to control bias. Applying a material with either a larger or smaller thermal expansion coefficient than lithium niobate to part of the waveguide could provide a means to customize the temperature behavior of the bias.

Lastly, the bandwidth of the sensor could be enhanced by further increasing the sensitivity of the IOPC. A smaller half-wave voltage permits using a Rogowski coil

with a smaller mutual inductance, and hence a larger bandwidth. The IOPC could be made more sensitive by forming a ridge structure to enhance the overlap of the electrodes with the optical field. This can be accomplished by wet-etching ridges using a proton-exchange pretreatment [61]. The sensitivity of the IOPC could be further increased by increasing the length of the waveguide and electrodes. Lengthening the device should be done in combination with a reduction in the temperature sensitivity of the optical bias point to avoid dynamic range limitations.

Bibliography

[1] B. Hague, *Instrument Transformers*, Sir Isaac Pitman & Sons, London, 1936.

[2] Power Systems Instrumentation Emerging Technologies Working Group and Measurements Committee *et al.*, "Optical current transducers for power systems: a review," *IEEE Transactions on Power Delivery*, vol. 9, no. 4, pp. 1778–1788, 1994.

[3] L. Kojovic, "Rogowski coils suit relay protection and measurement," *IEEE Computer Applications in Power*, pp. 47–52, July 1997.

[4] T. D. Maffetone and T. M. McClelland, "345 kV substation optical current measurement system for revenue metering and protective relaying," *IEEE Transactions on Power Delivery*, vol. 6, no. 4, pp. 1430–1437, 1991.

[5] G. Zhang, S. Li, Y. Qin, and Z. Zhang, "A new electro-optic hybrid current-sensing scheme for current measurement at high voltage," *Review of Scientific Instruments*, vol. 70, no. 9, pp. 3755–3758, 1999.

[6] C. McGarrity, Y. N. Ning, J. L. Santos, and D. A. Jackson, "A fibre-optic system for three-phase current sensing using a hybrid sensing technique," *Review of Scientific Instruments*, vol. 63, no. 3, pp. 2035–2039, 1992.

[7] Y. N. Ning, T. Y. Liu, and D. A. Jackson, "Two low-cost robust electro-optic hybrid current sensors capable of operation at extremely high potential," *Review of Scientific Instruments*, vol. 63, no. 12, pp. 5771–5773, 1992.

[8] T. Wang, C. Luo, and S. Zheng, "A fiber-optic current sensor based on a differentiating sagnac interferfometer," *IEEE Transactions on Instrumentation and Measurement*, vol. 50, no. 3, pp. 705–708, 2001.

[9] Z. Gang, L. Shaohui, Z. Zhipeng, and C. Wei, "A novel electro-optic hybrid current measurement instrument for high-voltage power lines," *IEEE Transactions on Instrumentation and Measurement*, vol. 50, no. 1, pp. 59–62, 2001.

[10] R. Malewski, "High-voltage current transformers with optical signal transmission," *Optical Engineering*, vol. 20, no. 1, pp. 54–57, 1981.

[11] W. Rogowski and W. Steinhaus, "Die messung der magnetischen spannung," *Archiv fur Elektrotechnik*, vol. 1, part 4, pp. 141–150, 1912.

[12] A. P. Chattock, "On a magnetic potentiometer," *Philos. Mag.*, vol. 24, no. 5, pp. 94–96, 1887.

[13] N. A. F. Jaeger and F. Rahmatian, "Integrated electro-optic high-voltage sensors," in *EPRI Optical Sensors for T&D Applications Workshop*, Portland, OR, July 20-21, 1995.

[14] N. A. F. Jaeger and F. Rahmatian, "Integrated optics Pockels cell high-voltage sensor," *IEEE Transactions on Power Delivery*, vol. 10, no. 1, pp. 127–134, 1995.

[15] N. A. F. Jaeger and F. Rahmatian, "Bias of integrated optics Pockels cell high-voltage sensor," *SPIE*, vol. 2072, pp. 87–95, 1993.

[16] J. D. Bull, N. A. F. Jaeger, and F. Rahmatian, "Hybrid electro-optic/inductive current sensor for high-voltage power system applications," in *2000 International Conference on Applications of Photonic Technology*, Quebec City, Canada, June 12-16, 2000, vol. SPIE 4087, pp. 1222–1228.

[17] J. D. Bull, N. A. F. Jaeger, and F. Rahmatian, "A new hybrid current sensor for high-voltage applications," *IEEE Transactions on Power Delivery*, 2004, accepted for publication.

[18] IEEE, New York, NY, *IEEE Standard Requirements for Instrument Transformers, IEEE Std C57.13-1993*, 1994.

[19] IEC, Geneva, Switzerland, *IEC 60044-1, Instrument Transformers — Part 1: Current Transformers*, 1st edition, 1996.

[20] IEC, Geneva, Switzerland, *IEC 60044-8, Instrument Transformers — Part 8: Electronic Current Transformers FDIS*, 2002.

[21] J. D. Bull, N. A. F. Jaeger, and F. Rahmatian, "Optical current measuring for high voltage systems," US Patent Number 6,670,799, Dec. 30, 2003.

[22] J. D. Ramboz, "Machinable rogowski coil, design and calibration," in *IMTC/95*, Waltham, MA, 1995, pp. 329–334.

[23] K. Heumann, "Magnetic potentiometer of high precision," *IEEE Transactions on Instrumentation and Measurement*, vol. IM-15, pp. 242–250, 1966.

[24] G. J. Carlson and F. A. Fisher, "Voltage and current sensors for a 1200 kV gas insulated bus," in *7th IEEE/PES Transmission and Distribution Conference and Exposition*, Atlanta, GA, April 1-6, 1979, pp. 200–207.

[25] P. A. Thornton and V. J. Colangelo, *Fundamentals of Engineering Materials*, Prentice-Hall, Englewood Cliffs, NJ, 1985.

[26] R. C. Dorf and R. H. Bishop, *Modern Control Systems*, chapter 10, pp. 531–534, Addison-Wesley, 7th edition, 1995.

[27] E. C. Ifeachor and B. W. Jervis, *Digital Signal Processing*, chapter 7, pp. 383–388, Addison-Wesley, Wokingham, England, 1993.

[28] W. F. Ray and C. R. Hewson, "High performance Rogowski current transducers," in *Industry Applications Conference, 2000*, Nottingham, UK, October 8-12, 2000, IEEE, vol. 5, pp. 3083–3090.

[29] D. A. Ward and J. La T. Exon, "Using Rogowski coils for transient current measurement," *Engineering Science and Education Journal*, pp. 105–113, June 1993.

[30] D. C. Erickson, "The use of fibre optics for communications, measurement and control within high voltage substations," *IEEE Transactions on Power Apparatus and Systems*, vol. PAS-99, no. 3, pp. 1057–1063, 1980.

[31] R. B. Northrop, *Introduction to Instrumentation and Measurements*, chapter 5, pp. 144–145, CRC Press LLC, 1997.

[32] A. Donaldson, "Candidate materials and technologies for integrated optics: fast and efficient electro-optic modulation," *Journal of Physics D. Applied Physics*, vol. 24, no. 6, pp. 785–802, 1991.

[33] J. F. Nye, *Physical Properties of Crystals*, chapter 13, Oxford University Press, Oxford, 2nd edition, 1993.

[34] Z. Nehari, *Conformal Mapping*, Dover Publications, New York, 1952.

[35] O. G. Ramer, "Integrated optic electrooptic modulator electrode analysis," *IEEE Journal of Quantum Electronics*, vol. QE-18, no. 3, pp. 386–392, 1982.

[36] R. S. Weis and T. K. Gaylord, "Lithium niobate: Summary of physical properties and crystal structure," *Applied Physics A: Solids and Surfaces*, vol. A37, pp. 191–203, 1985.

[37] T. Tamir, Ed., *Guided-Wave Optoelectronics*, chapter 4, p. 150, Springer-Verlag, Berlin, second edition, 1990.

[38] L. Thylen and P. Granestrand, "Integrated optic electrooptic device electrode analysis: The influence of buffer layers," *Journal of Optical Communications*, vol. 7, no. 1, pp. 11–14, 1985.

[39] M. Minakata, "$LiNbO_3$ optical waveguide devices," *Electronics and Communications in Japan, Part 2*, vol. 77, no. 11, pp. 37–51, 1995.

[40] H. Nagata, J. Ichikawa, M. Kobayashi, J. Hidaka, H. Honda, K. Kiuchi, and T. Sugamata, "Possibility of dc drift reduction of Ti:$LiNbO_3$ modulators via dry O_2 annealing process," *Applied Physics Letters*, vol. 64, no. 10, pp. 1180–1182, 1994.

[41] C. H. Bulmer, W. K. Burns, and S. C. Hiser, "Pyroelectric effects in $LiNbO_3$ channel-waveguide devices," *Applied Physics Letters*, vol. 48, no. 16, pp. 1036–1038, 1986.

[42] T. Fujiwara, S. Sato, H. Mori, and Y. Fujii, "Suppression of crosstalk drift in Ti:$LiNbO_3$ waveguide switches," *Journal of Lightwave Technology*, vol. 6, no. 6, pp. 909–915, 1988.

[43] H. Nagata annd J. Ichikawa, "Progress and problems in reliability of Ti:$LiNbO_3$ optical intensity modulators," *Optical Engineering*, vol. 34, no. 11, pp. 3284–3293, 1995.

[44] M. Minakata S. Yamada, "DC drift phenomena in $LiNbO_3$ optical waveguide devices," *Japanese Journal of Applied Physics*, vol. 20, no. 4, pp. 733–737, 1981.

[45] T. Suhara, M. Fujimura, K. Kinoshita, and H. Nishihara, "Reduction of DC drift in $LiNbO_3$ waveguide electro-optic devices by phosphorus doping in SiO_2 buffer layer," *Electronics Letters*, vol. 26, no. 17, pp. 1409–1410, 1990.

[46] H. Nagata, M Shiroishi, T. Kitanobou, and K. Ogura, "DC drift reduction in $LiNbO_3$ optical modulators by decreasing the water content of vacuum evaporation deposite SiO_2 buffer layers," *Optical Engineering*, vol. 37, no. 10, pp. 2855–2858, 1998.

[47] M. Minakata, "DC-drift-free Ti-diffused $LiNbO_3$ optical modulators," in *CLEO'95*, Baltimore, MD, May 1995, pp. 62–63.

[48] G. P. Agrawal, *Fiber-Optic Communication Systems*, chapter 7, pp. 155–159, John Wiley & Sons, New York, 1992.

[49] C. Hentschel, *Fiber Optics Handbook*, Hewlett-Packard GmbH, Germany, 3nd edition, 1989.

[50] H. Kato, "Fabrication of lithium niobate integrated optic pockels cells," Tech. Rep., Kato and Associates Research Ltd. for Nxtphase Corporation, Vancouver, BC, 1998.

[51] A. A. Blistanov, V. V. Geras'kin, A. V. Stepanova, M. V. Puchkova, and N. G. Sorokin, "Changes in the pyroelectric field and electrical conduction mechanisms in $LiNbO_3$ at $T = 20 - 200°C$," *Soviet Physics Solid State*, vol. 26, no. 4, pp. 684–687, 1984.

[52] O. Ogawa, T. Sowa, and S. Ichizono, "A guided-wave optical electric field sensor with improved temperature stability," *Journal of Lightwave Technology*, vol. 17, no. 5, pp. 823–830, 1999.

[53] C. H. Ling, J. Bahaskaran, W. K. Choi, and L. K. Ah, "Study of rf-sputtered yttrium oxide films on silicon by capacitance measurements," *Journal of Applied Physics*, vol. 77, no. 12, pp. 6350–6353, 1995.

[54] U. Adler, Ed., *Automotive Handbook*, Robert Bosch GmbH, Stuttgart, 2nd edition, 1986.

[55] J. Saulnier, *Materials for Optoelectronics*, chapter 2, pp. 293–339, Kluwer Academic Publishers, 1996.

[56] J. D. Bull, N. A. F. Jaeger, H. Kato, and F. Rahmatian, "Effects of mode conversion caused by anisotropic propagation in polarimetric lithium niobate guided-wave voltage sensors," in *2000 CAP Congress*, 2000.

[57] J. Ctyroky, "Analysis of polarization effects in near-Z-axis Ti:$LiNbO_3$ devices," *Journal of Optical Communications*, vol. 14, no. 1, pp. 32–38, 1993.

[58] A. Yariv, *Optical Electronics in Modern Communications*, chapter 10, pp. 502–504, Oxford University Press, 5th edition, 1997.

[59] P. P. Chavez, J. D. Bull, N. A. F. Jaeger, and F. Rahmatian, "Effects of device geometry and orientation on the performance of lithium niobate integrated-optic pockels cell immersion-type electric field sensors," in *2000 CAP Congress*, 2000.

[60] P. F. Bordui, D. H. Jundt, E. M. Standifer, R. G. Norwood, R. L. Sawin, and J. D. Galipeau, "Chemically reduced lithium niobate single crystals: Processing, properties and improved surface acoustic wave fabrication and performance," *Journal of Applied Physics*, vol. 85, no. 7, pp. 3766–3769, 1999.

[61] S. Chang, C. Tsai, Y. Lin, J. Liu, and W. Wang, "Improved electrooptic modulator with ridge structure in x-cut $LiNbO_3$," *Journal of Lightwave Technology*, vol. 17, no. 5, pp. 843–847, 1999.

Appendix A

Coupled-Mode Formulation

The development of the coupled-mode equations, 6.19 and 6.20, is presented here.

We begin with the wave equation:

$$\nabla^2 \overline{E} + \omega^2 \mu_o [\epsilon + \Delta\epsilon''] \overline{E} = 0 \tag{A.1}$$

where $[\Delta\epsilon'']$ represents the permittivity perturbation matrix. The electric field, $\overline{E}$, can be expanded in terms of the two modes:

$$\overline{E} = \overline{E}_a + \overline{E}_b \tag{A.2}$$

where

$$\overline{E}_a = A(z) \exp(-j\beta_a z) \overline{\varepsilon}^a(x, y) \tag{A.3}$$

and

$$\overline{E}_b = B(z) \exp(-j\beta_b z) \overline{\varepsilon}^b(x, y). \tag{A.4}$$

The terms $\overline{\varepsilon}^{a,b}(x, y)$ are the electric field distributions of the unperturbed modes and

have the form:

$$\overline{\varepsilon}^{a,b}(x,y) = \begin{pmatrix} \varepsilon_x^{a,b}(x,y) \\ \varepsilon_y^{a,b}(x,y) \\ \varepsilon_z^{a,b}(x,y) \end{pmatrix}. \tag{A.5}$$

The field distributions are normalized so that:

$$\int\int \overline{\varepsilon}^{a,b*} \cdot \overline{\varepsilon}^{a,b}\, \mathrm{d}x\, \mathrm{d}y = 1. \tag{A.6}$$

Using the "slow variation" assumption [58], the expansion of the wave equation with the mode definitions leads to:

$$\begin{gathered} \overline{\varepsilon}^{a} 2j\beta_a \tfrac{\mathrm{d}A}{\mathrm{d}z} \exp(-j\beta_a z) + \overline{\varepsilon}^{b} 2j\beta_b \tfrac{\mathrm{d}B}{\mathrm{d}z} \exp(-j\beta_b z) = \\ B\omega^2\mu_o[\Delta\epsilon'']\overline{\varepsilon}^{b} \exp(-j\beta_b z) + A\omega^2\mu_o[\Delta\epsilon'']\overline{\varepsilon}^{a} \exp(-j\beta_a z). \end{gathered} \tag{A.7}$$

The first of the two coupled-mode equations is obtained by multiplying both sides of Equation A.7 by $\overline{\varepsilon}^{a*}$ and integrating over x and y. The second equation is obtained using the same procedure with $\overline{\varepsilon}^{b*}$ instead of $\overline{\varepsilon}^{a*}$. Beginning with the $\overline{\varepsilon}^{a*}$ integral, Equation A.7 can be reduced to:

$$\begin{gathered} 2j\beta_a \tfrac{\mathrm{d}A}{\mathrm{d}z} \exp(-j\beta_a z) = B\omega^2\mu_o \exp(-j\beta_b z) \int\int \overline{\varepsilon}^{a*} \cdot [\Delta\epsilon'']\overline{\varepsilon}^{b}\, \mathrm{d}x\, \mathrm{d}y + \\ A\omega^2\mu_o \exp(-j\beta_a z) \int\int \overline{\varepsilon}^{a*} \cdot [\Delta\epsilon'']\overline{\varepsilon}^{a}\, \mathrm{d}x\, \mathrm{d}y \end{gathered} \tag{A.8}$$

by using the orthogonality of the unperturbed modes. The term with A can be interpreted as a change in the propagation constant, β_a, of the unperturbed mode due to the diagonal terms in the permittivity perturbation, $[\Delta\epsilon'']$. If the diagonal terms of $[\Delta\epsilon'']$ are included in the perturbed propagation constants, β_a' and β_b', Equation A.8 becomes:

$$2j\beta_a' \frac{\mathrm{d}A}{\mathrm{d}z} \exp(-j\beta_a' z) = B\omega^2\mu_o \exp(-j\beta_b' z) \int\int \overline{\varepsilon}^{a*} \cdot [\Delta\epsilon_{od}'']\overline{\varepsilon}^{b}\, \mathrm{d}x\, \mathrm{d}y \tag{A.9}$$

where $[\Delta\epsilon''_{od}]$ is composed of the off-diagonal terms of $[\Delta\epsilon'']$. Equation A.9 is now easily rewritten as:

$$\frac{\mathrm{d}A}{\mathrm{d}z} = \frac{-j\omega^2\mu_o}{2\beta'_a}\exp\left(j\Delta\beta z\right)\int\int \overline{\varepsilon}^{a*}\cdot[\Delta\epsilon''_{od}]\overline{\varepsilon}^{b}\,\mathrm{d}x\,\mathrm{d}yB \tag{A.10}$$

where

$$\Delta\beta = \beta'_a - \beta'_b. \tag{A.11}$$

Equation A.10 is equivalent to Equation 6.19 presented in Chapter 6 since the diagonal terms of $[\Delta\epsilon'']$ in Equation 6.19 do not contribute to the overlap integral. The derivation of Equation 6.20 follows the same procedure.